Yukawa Force Spectroscopy to Search for Violations of Newton's Law of Gravity below $1\,\mu\mathrm{m}$ Distances

Von der QUEST-Leibniz-Forschungsschule der
Gottfried Wilhelm Leibniz Universität Hannover zur
Erlangung des Grades
Doktor der Naturwissenschaften
Dr. rer nat.

genehmigte Dissertation

von
Helena Schmidt

geboren am 31.10.1987

Erscheinungsjahr: 2020

Abstract

Gravity is well tested on several length scales, but some unified theories predict deviations in the region below $1\,\mathrm{mm}$. In this thesis I will present a method to search for such deviations in the sub-micrometre length scale. Below $1\,\mu\mathrm{m}$, the electrostatic and the Casimir force are stronger than the gravitational force by some magnitudes. To distinguish these forces, I have designed a new force measurement setup based on the frequency modulation AFM technique. Utilizing a quartz based parallelogram cantilever, it is feasible to measure these forces with sufficient accuracy for us to set new constraints for possible deviations of gravity. In this thesis I will present a new method of measuring such deviations of gravity, and show the initial results I have obtained using it. This will show that the measurement concept works, but that improvements are necessary before we can achieve optimum measurement uncertainty.

Keywords *Newton's Law of Gravity, Yukawa potential, Casimir effect*

Inhaltsangabe

Gravitation ist auf verschiedenen Längenskalen gut getestet, allerdings sagen einige vereinheitlichte Theorien Abweichungen bei Abständen unter 1 mm voraus. In dieser Arbeit zeige ich ein Messverfahren, um derartige Abweichungen im Submikrometerbereich zu untersuchen. Unterhalb von $1\,\mu$m dominieren die elektrostatische Kraft und die Casimir-Kraft. Um Gravitation von den anderen Kräften unterscheiden zu können, basiert das neue Kraftmesssystem auf einem frequenzmodulierten AFM. Ein Parallelogramm-Cantilever aus Quartz ermöglicht es, die Messgenauigkeit zu erhöhen. Die vorliegende Arbeit hat zum Ziel, den Aufbau des Messverfahrens sowie die ersten Messergebnisse zu dokumentieren. Darüberhinaus wird auf nötige Verbesserungen eingegangen, damit spätere Messungen genau genug sind, um die Grenzen des Gravitationsgesetzes zu verschieben.

Schlagworte *Gravitation, Yukawa Potential, Casimir Effekt*

Diese Fassung unterscheided sich durch kleine sprachliche Korrekturen von der zur Begutachtung eingereichten Fassung. AuSSerdem wurden die Grafiken 2.2, 5.27 und 6.11 dahingehend geändert, dass Lee et al. 2020 anstatt der vorläufigen Ergebnisse von 2019 eingezeichnet wurden.

Contents

Chapter 1

Introduction

Although gravity has been well tested on several length scales, some *unified theories* predict that it is possible that gravity is different somewhere below distances of 1 mm. This could happen, for example, through a set of small extra dimensions. Gravity propagates through all dimensions equally. This means the same amount of energy has different volumes to fill for different numbers of dimensions. Therefore, the strength of gravity changes with the number of dimensions. There are various methods of searching for deviations from gravitational force.

The first experiment used to measure a direct gravitational effect between two bodies was the Cavendish experiment. The experiment consisted of two large fixed spheres, and two small spheres attached to a torsion balance. The force between the small and the large spheres led to the torsion of the torsion balance. Knowing the torsion coefficient, it is possible to calculate the gravitational force. This experiment was used to determine the gravitational constant for the first time and also to measure the density of the Earth in 1797 and 1798 [1]. Fig. 1.1 shows the schematic of the experiment.
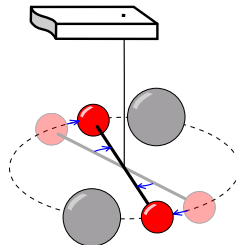
Figure 1.1: Schematic of the torsion balance of the Cavendish experiment [2].

Variations of this experiment are still the most accurate measurement tools we have determining gravitational force at distances between 1 mm and 1 m. For larger distances, astronomical observations are used. During the Moon landing missions between 1969 and 1972, several retroreflectors were placed on the Moons surface. These retroreflectors make it possible to measure the distance between the Moon and the Earth [3]. This method is called lunar laser ranging and it delivers the most precise measurement of Newton's law of gravity currently available.

In 1986 Fischbach et al. [4] reanalyzed experimental data from 1922 the Eötvös experiment. He proposed, based on the above analysis, that Newton's gravitational constant might be material-dependent. This would mean that gold would fall differently compared to hydrogen, for example. This new type of gravitational interaction was called the *fifth force* [1]. There is currently no evidence that this fifth force really exists, but its existence has also yet to be ruled out either.

1.1 Motivation: The Cosmological Constant Problem

Wikipedia has a list of unsolved problems in physics [7]. The *cosmological constant problem* is part of that list. It refers to the fact that the cosmological constant in Einstein's general relativity is several orders of magnitude smaller than estimates based on quantum field theories would indicate [8]. In 1948 [9], Dutch physicist Hendrik Casimir predicted an effect, which was named after him. In quantum field theory, a harmonic oscillator has an infinite amount of quantized energy states. State zero is the most important state for this experiment, because a harmonic oscillator has finite energy without any excitation in this state. This is called *zero-point energy*. Standing electromagnetic waves can exist between two perfectly conducting parallel plates. The distance between the two plates determines which wavelengths are able to be produced. For each wavelength, there is a corresponding zero-point energy level. Summing over all zero-point energies of wavelengths allowed by the boundary conditions results in the total amount of zero-point energy stored between the plates. This result also depends on whether a physical theory states a minimal allowed wavelength or not. Today, the Planck length ($\sim 1.6 \cdot 10^{-35}$ m) is most often used for this. This calculation leads to an energy density that would be 10^{120} times larger than the energy density of the cosmological constant. If we make a more sophisticated calculation for the vacuum energy density based on quantum field theory, then the mismatch is reduced to about 54 orders of magnitude [10] compared to the cosmological constant.

1.2 Promising theoretical approaches

In 1998, the ADD model [11] was proposed by Arkani-Hamed, Dimopoulos and Dvali (and named after the authors surnames). The ADD model, also known as the model with LED (large extra dimensions), describes how gravity can travel through more dimensions than just the three with which we are familiar. While electromagnetism can only travel in three dimensions, in the ADD model, there can be two extra dimensions through which gravity can travel, and that is just one example. This leads to a weaker gravitational force in our three dimensions and might explain why gravity is so much weaker than the electromagnetic force.

---

[1] The term *fifth force* is not only used for a new kind of gravitational force, but for every possible kind of new fundamental force. For example Krasznahorkay et al. claimed to have found a fifth force in 2015 [5][6], but this claim was neither proven wrong nor successfully replicated by another group.

In 1977, the PecceiQuinn theory [12] tried to explain why the neutron has no observable electric dipole moment even though quantum physical considerations indicate that it should have one. This theory proposed a new hypothetical particle called the axion. The axion is a dark matter candidate. Dark matter comprises 27% of all mass and energy in the universe, but has not been directly observed so far. Therefore the search for a dark matter candidate is mandatory. Dvali and Funcke [13] proposed the domestic axion hypothesis in 2016. This would also explain why the mass of a neutrino is not zero. Their model leads to predictions for gravity experiments at small distances.

Another component of the universe, dark energy, has also not been detected directly. There is a hypothesis about a particle called the *chameleon particle*, which is a dark energy candidate [14]. A chameleon particle's mass fluctuates based on local energy density, and this behavior is what gives the chameleon particle its name. Chameleon particles would cause an additional force, thus providing another reason why we should experiment on gravity at small distances.

Edholm et al. [15] proposed a model that tries to resolve the fact that gravity has singularities in Newtons and Einsteins theories. He also calculated how this model would change the behavior of Newton's law of gravity and found deviations below distances of $1\,\mu$m. In this model, the gravitational potential energy is saturated at very small distances, and at these distances a saturation of potential energy causes the force to decrease.

1.3 Experimental Concept

Most force measurements use a spring-like setup, meaning that a spring or something that acts like a spring is used. When a force acts on the spring, the compression or stretching length of the spring is proportional to the force. This constant of proportionality is called the spring constant and is usually written as k. The changes in length are easy to measure – one option is to use a laser interferometer. The smaller the spring constant, the larger the change in length is. Unfortunately this also means there exists a minimal distance between the two masses. At a certain distance, the force becomes high enough to pull the spring all the way to the source mass. This minimal distance increases with a smaller k.
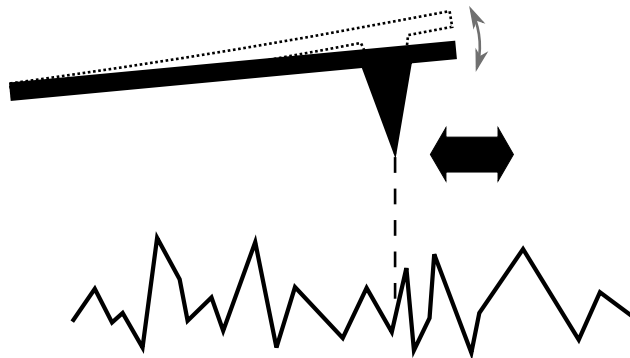
Figure 1.2: Schematic of an AFM with a cantilever.

After Binnig, Quate and Gerber [16] introduced the atomic force microscopes (AFMs), AFMs became more common in the 1990s. AFMs measure the force between a small tip, attached to a cantilever, and a surface of interest. AFMs made it possible to scan over surfaces to obtain microscopic images at an atomic scale. The cantilever is also a kind of spring with its own spring constant k. One problem with this measurement setup is that the cantilever tip jumps into contact with the surface. This is a problem, because it leads to a minimal possible distance for the force measurement and that the tip may be damaged. One solution to this problem would be to increase the stiffness of the cantilever. But a higher stiffness reduces the force resolution of the measurement. To overcome these problems, Giessibl [17] developed the frequency modulated AFM. The force is measured using a frequency measurement, rather than the length change described in the previous method. The resonance frequency of the AFM changes when a non-linear force is applied. This method allows us to use a higher k with the same precision as the previous method, which in turn allows us to measure at even smaller distances.
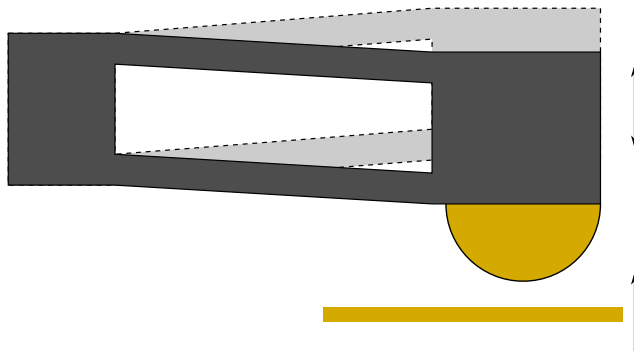
Figure 1.3: Schematic of a parallelogram flexure.

Testing gravity with an AFM requires some changes to our setup. Instead of a tip a sphere, or half-sphere is attached to the cantilever. Also, our AFM does not scan over the surface, instead we measure the force at different distances between the sphere and the plane surface. If we coat both surfaces with gold, which is highly dense, then this will create a higher gravitational effect. Also, unlike other high density metals, gold has a tendency not to form oxides, a property we can take advantage of when measuring the Casimir effect, because oxides are less conductive than bare metals. After measuring the Casimir effect, the electrostatic attraction and the Casimir effect can be subtracted from our resulting measurements, leaving only noise and a possible gravitational effect in our data.

Melcher et al. [18] demonstrated that a parallelogram flexure can replace the cantilever. This means we can achieve force measurements with a resolution of 14 fN with high Q systems[2]. Compared to a cantilever, a parallelogram flexure has no parasitic rotation during vibration. We can use radiation pressure to drive the vibration. With this method, one can reach a vibration amplitude as small as 1 nm or below.

Using the parallelogram flexure the gravitational effect distance of 0.1 nm to 100 nm comes into focus. Usually the length scale is written as λ and the

---

[2]See section 4.1.3 for a description of the quality factor Q.

effect size relative to the gravitation force is written as α. Section 3.1.1 describes the easiest modification of gravity in our length scale, known as *Yukawa Potential*.

Chapter 2

Current State of Research

For more than two centuries, Newton's law of gravity was the main theoretical model of gravity, until it was replaced by Einstein's general relativity in 1915.

2.1 Long Distance: Tests of General Relativity

More than a century has passed and Einstein's general relativity remains the best known theory of gravitation. When it was published, it explained Mercury's perihelion shift, observed by Le Verrier in 1859 [19]. This chapter describes some of the experimental tests of general relativity that were conducted in the last century.

2.1.1 Deflection of Electromagnetic Radiation

The first test of a prediction made by general relativity was to measure deflected light. The term *deflection of light* refers to a phenomenon where an electromagnetic wave that passes an object with a large mass is deflected due to the gravitational field of that object. The measurements were done by Dyson et al. [20] during the 1919 solar eclipse. They used three telescopes at two different locations to measure the deflection, but the results from only one telescope were sufficient reliable results. The next solar eclipse in 1922 provided better data and was also supporting general relativity over Newton's law of gravity [21]. The most spectacular example of deflection of light is gravitational lensing, and specifically the Einstein ring [22]. Unfortunately, we do not currently have precise, independent information about the amount of mass that produces gravitational lensing. In 1989 the Hipparcos satellite mission was launched to measure the positions of about a hundred thousand celestial bodies. Its measurements were used by Freoschle et al. [23] to estimate the deflection of light caused by the Sun. In 2013, the Gaia satellite was launched as a successor to Hipparcos. Its goal is to measure the positions of more than a billion celestial bodies with a higher precision than Hipparcos. Hees et al. [24] expects its deflection of light measurements will be helpful in constraining alternative gravitational theories.
The best way we currently have of measuring the deflection of light, or electromagnetic radiation, uses radio astronomy. It does not rely on there being a solar eclipse, so it can be used to retrieve much more data. *Very*

Long Baseline Interferometry allows precise position measurements of radio sources from across the entire celestial sphere and has been analyzed by Lambert and Le Poncin-Lafitte [25].

2.1.2 Shapiro Delay

In 1964, Shapiro [26] proposed a new test for general relativity that can be performed inside our solar system. It is based on the time dilation effect of a large mass. Electromagnetic radiation passing by a large mass like the Sun or Jupiter is slowed down. This time delay of a signal compared to a hypothetical Newtonian mass is called Shapiro delay. One of the first precise measurements of the Shapiro delay was done using the Viking spacecaft [27]. The Cassini spacecraft provided far more accurate measurements [28]. The time dilation of general relativity was also measured using atomic clocks on Earth [29], and is used to make the global positioning service (GPS) [30] more accurate.
The Shapiro delay is also important in multi messenger astronomy. Neutrinos and photons arrived on Earth almost simultaneously after the supernova 1987a occurred [31]. Some alternative theories of gravity claim that gravitational waves have a different Shapiro delay [32]. The gravitational wave event *GW170817*, an event that had an electromagnetic counterpart[1] [33], hardly constrained these theories.

2.1.3 Strong Equivalence Principle

The equivalence principle is one of the theoretical foundations of general relativity. In its Newtonian form it states that gravitating mass is identical to inertial mass. There is also the *weak equivalence principle* (WEP), that states the universality of free fall [34]:

> *Test particles with negligible self-gravity behave independently of their properties in a gravitational field.*

The *strong equivalence principle* (SEP) states [34]:

> *All test fundamental physics (including gravitational physics) is not affected, locally, by the presence of a gravitational field.*

This means, for example, that the Newtonian gravitational constant G is constant anywhere and anytime in the universe. General relativity fulfills the *strong equivalence principle*. But there are different theories of gravity that fulfill the WEP but not the SEP. One example for that is a theory called *MOG*[2] [36][37].
Fig. 2.1 describes the WEP. This depiction could also be used as an example of the SEP, if a Cavendish-like experiment is performed inside of the reference frames instead of using a laser beam.
In 2014, a neutron star pulsar with two white dwarf companions was observed [38]. The inner white dwarf has an orbital period of 1.6 days which puts it in the strong gravitational field of the neutron star. Strong is defined in this context so, that first order post Newtonian corrections are insufficient

---

[1]Only one gravitational wave with an electromagnetic counterpart has been observed so far, which means it is possible, though unlikely, that the electromagnetic counterpart was purely coincidental.
[2]Short for *modified gravity*.
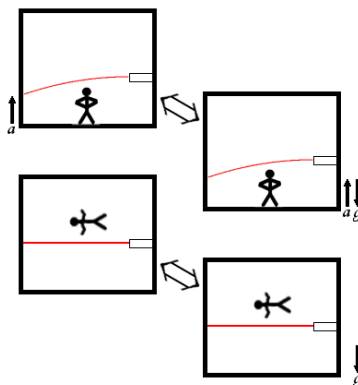
Figure 2.1: Graphical example of the equivalence principle [35]. The upper left image shows the equivalence of an accelerated reference frame to a reference frame bound by gravity as shown on the upper right image. A laser beam is used during the experiment, and in both cases the beam is curved. The lower left image depicts the equivalence of a reference frame with no gravitational field affecting it, to free falling in a gravitational field that is shown on the right. In both cases, the laser beam is straight from the point of view of any observer inside of the reference frame.

to describe the system. This neutron star system was observed since then, and in 2018, the currently best constraints on the SEP under strong gravitational conditions were published by Archbald et al. [39].
Under weak gravitational conditions, the best test for the SEP comes from data gathered by the NASA Messenger mission, during which NASA measured Mercury's orbit [40] as well as from lunar laser ranging [41].
The immutability in time of the gravitational constant G was best obtained by the ephemeris of Mars [42][19] and is now better constrained by the ephemeris of Mercury [40]. The Mercury results are only bounded by the uncertainty of the mass loss of the Sun due to solar wind.

2.1.4 Gravitational Waves

Gravitational waves were postulated by Einstein in 1918 [43], but the first time they were observed, by Hulse and Taylor in 1974 when they discovered a pulsar in a binary system, they were only able to be observed indirectly. They noted that the orbits of both objects in the system changed because of energy loss, and that this energy loss was consistent with that which would be lost due to gravitational waves. However, the first direct observation was done in 2015 after starting the two advanced LIGO detectors [44]. The first observed gravitational wave was generated by a binary black hole merger. Since then, most of the observed gravitational waves were binary black holes mergers. One binary neutron star merger was observed that lead to the observations stated in section 2.1.2.
Gravitational waves are a good test for general relativity, since we can only detect waves that are generated under strong gravitational field conditions. In 2019 the LIGO scientific collaboration published some of the tests [45] they performed on their data. All results were consistent with general
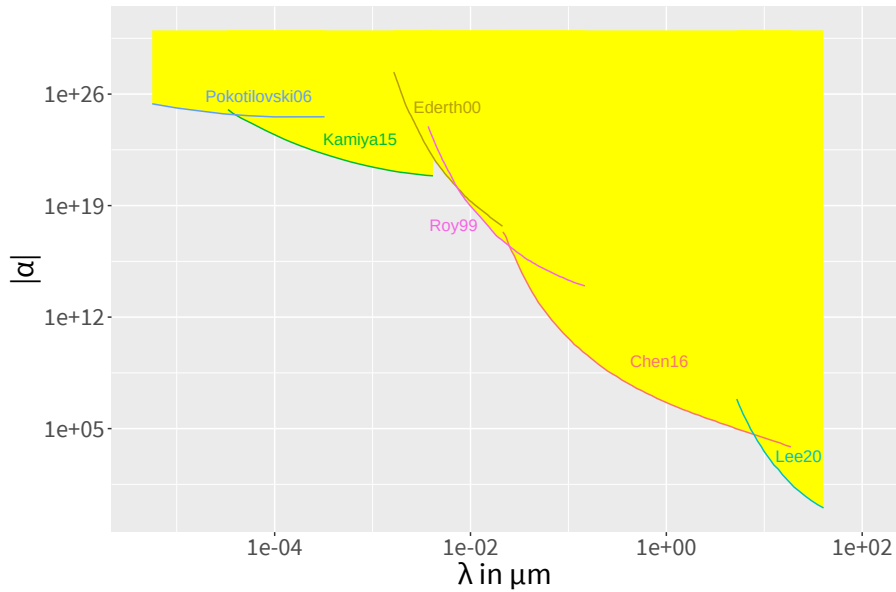
Figure 2.2: The yellow upper right corner marks the excluded parameters for α and λ in the Yukawa potential. The lines are from specific published measurements: Pokotilovski (2006) [46], Kamiya (2015) [47], Nesvishevsky (2008) [48], Ederth (2000) [49], Roy (1999) [50], Chen (2016) [51], Lee (2020) [52].

relativity and constrain possible alternatives. One result that may be important for unified theories of gravity and the standard model of particle physics is their upper bound on the mass of the hypothetical graviton:

$$m_g \leq 5.0 \cdot 10^{-23} \text{eV/c}^2 \tag{2.1}$$

2.2 Latest Short-Range Experiments

This thesis focuses on short-range deviations from gravity. Section 3.1.1 explains the Yukawa potential and its usage to parameterize deviations from gravity. It has two free parameters, α and λ, that build a parameter space. Each experiment that was done so far can be used to rule out a specific set of α and λ. In Fig. 2.2 the ruled out parameters are shown.

Other experiments are currently under way, such as the third generation of the *qBounce* experiment of the Vienna group of H. Abele [53] and the quantization of gravity experiments by the Aspelmeyer Group [54][55].

2.2.1 Antiprotonic Helium Spectroscopy

Antiprotonic helium is helium where one electron is replaced by an antiproton. The energy level of the antiproton depends on the gravitational potential. Therefore a possible Yukawa potential influences the energy levels and the energy needed for the transition of the antiproton to another energy level. In Tanaka et al. [56], the antiprotonic helium experiment by Hori et al. [57] was reanalyzed with the application to the Yukawa potential. In
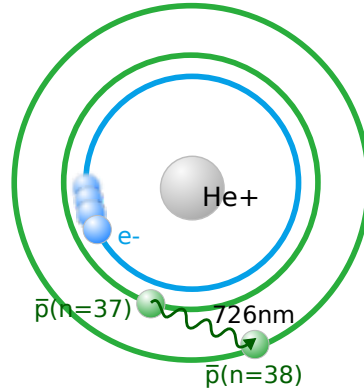
Figure 2.3: The antiprotonic helium has an antiproton instead of the second electron. The energy levels of the antiproton are measured spectroscopically.

Fig. 2.3 the measurement concept is shown. Their results would show up in Fig. 2.2 on the upper left side if it were extended below 10^{-10} m.

2.2.2 Neutron Scattering

In Fig. 2.2 the upper left excluded regions come from Pokotilovski [46] and Kamiya et al. [47] based on neutron scattering experiments. The atomic nucleus is built from the positive charged proton and the electrically neutral neutron. Therefore a neutron that hits an atom is mostly scattered by the atomic nucleus. The inner structure of a neutron consists of electrically charged quarks. This means neutrons have a charge distribution that leads to an interaction with the electrons of the electron shell. A possible new kind of interaction would be detectable due to a different scattering pattern of the neutrons. In the experiments, slow neutrons were used. That means they had an energy of about $\sim 1\text{meV}$. Slow neutrons have a wavelength that is much larger than the size of the nucleus. Therefore there is no diffraction pattern due to the nucleus. The energy of phonons in solids is about the same value of the low energy neutron. This could lead to inelastic scattering, which changes the scattering pattern. To avoid inelastic scattering gas targets, e.g. xenon gas or argon gas, were used. Kamiya et al. used the the HANARO research reactor in south Korea as neutron source [47] and xenon gas as a target. They calculated the expected scattering pattern using all known interactions the neutrons have in the experiment. And the deviations from that pattern were used to calculate limits on possible new interactions as seen in Fig. 2.2.

2.2.3 Casimir Force Measurements

The Casimir effect was first measured by Sparnaay [58] using parallel plates. In 1997 Lamoreaux [59] measured the Casimir effect to a higher precision by changing the geometry to a sphere and a plate. This geometry overcomes problems like surface profile and parallelism. This geometry was used by Roy et al. [50] using an atomic force microscope (AFM) to measure the force. A sphere was attached to a cantilever and the force between the sphere and a
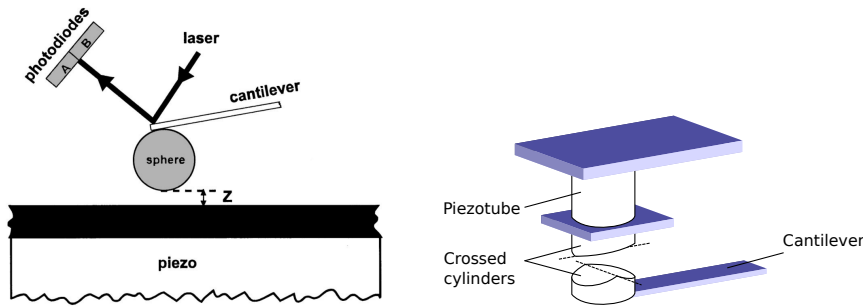
Figure 2.4: On the left is the experimental setup used by Roy et al. [50]. It used a sphere attached to a cantilever. The cantilever deflection was measured using laser beam that was reflected at the end of the cantilever. A quadrant photodiode was used to measure this deflection. On the right is the experimental setup used by Ederth et al. [49]. They used crossed cylinders for the experiment and measured the force using the cantilever deflection.

flat surface was measured using the deflection of the cantilever. For the deflection measurement, a laser beam was reflected at the end of the cantilever and was measured with a 4-quadrant photodiode. Ederth et al. [49] measured the Casimir effect between crossed cylinders. This geometry also has the advantage to avoid problems with parallelism and large-scale profile. Fig. 2.4 shows both experiments. After subtracting the Casimir Force from the measurement results, the residuals were used to calculate the limits of new gravitational forces in the nanometer range.

2.2.4 Rotating Source Mass

Measurements with rotating source masses are another possibility. The basic idea is that the source masses have regions with different densities on a disc. In case of Kapner et al. [60], holes in the discs were used, as they have the maximal possible density difference to the disc material. One disc on a torsion pendulum was used as the force sensor, the other disc was used as rotating source mass. The ratio between the number of holes at both discs has to be fractional. The frequency of the measurement signal then is not a harmonic of the rotation frequency, and the force signal is easier to detect. Between the source mass and the force measurement unit was a shielding membrane. Electrostatic and the Casimir effect were shielded by that and only the gravitational effect was measured. The disadvantage of this method is to calculate all influences on the force due to the specific geometry and a large simulation is needed. An improved version of that experiment was performed by Lee et al. [61], and its preliminary results are also shown in Fig. 2.2.

On the other hand, Chen et al. [51] used different materials within the disc, but coated a homogeneous layer of 150 nm thick gold on that disc. With this setup, they measured at a distance below a micron. The gold coating shields all electrical effects of the disc material, therefore the Casimir effect is constant during the measurement, and only gravitational effects due to the density differences have an effect on the measurement. One disadvantage of
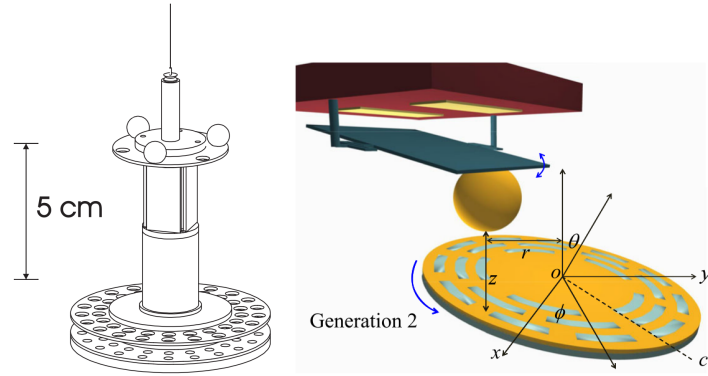
Figure 2.5: On the left: Experiment by Kapner et al. [60] using rotating source masses in the micrometer range. On the right: Experiment by Chen et al. [51] using rotating source mass and a torsional oscillator with a sphere attached to measure the force below the micrometer scale.

this method is, that the minimum possible distance between the density variations and the sphere is limited by the thickness of the gold coating, which has to be larger than $135\,\mathrm{nm}$ to attenuate the Casimir effect of the disc material by a factor of 10^6 [51][62]. The frequency of interest is different from the rotation frequency, because the density regions have a different distribution. The force measurement was performed using a torsional oscillator. Both measurements are shown in Fig. 2.5.

2.2.5   Shielded Cantilever Measurement

Geraci et al. [63] used the deflection of a cantilever to measure the gravitational force or any deviations from it. But instead of using a sphere and measuring the Casimir effect like Roy et al. they put a cuboid test mass on the cantilever, and placed a shielding membrane between the cantilever and the source mass. Similar to Chen et al. the density of the source mass was structured. The movement of the source mass had a frequency of a third of the cantilever resonance frequency. And if there were any deviations from the Yukawa potential, the amplitude of the cantilever bending would be a measurement of that deviation. See Fig. 2.6 for further details.

2.3   Epistemology for Gravitation

Plato and Aristotle used the term episteme for knowledge or understanding. Epistemology is the philosophical field for the theory of knowledge. Since Karl Popper, one main aspect is that you cannot prove a scientific theory. A scientific theory can only stand the test of time. The scientific method since him is to make only falsifiable statements. Another important concept of the scientific method is Occam's razor. It says, that if you have multiple models about the nature that are equally good to explain the specific field, you should choose the simplest model, i.e. the model with fewer parameters. For gravity this means, as we have Einstein's general relativity which supersedes Newton's law of gravity as a complete picture of gravity, we
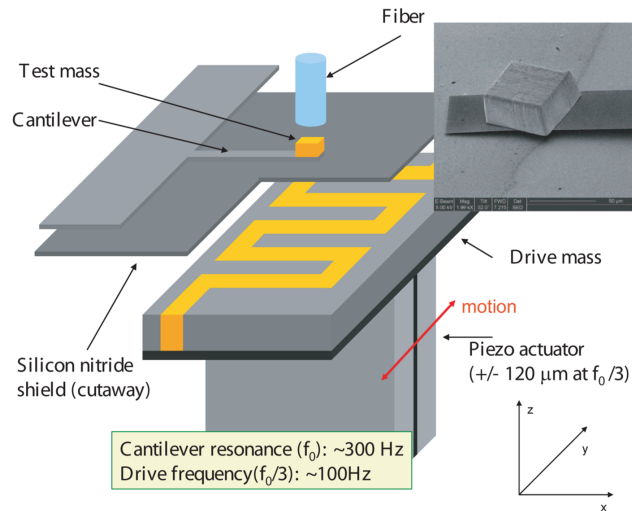
Figure 2.6: The schematic shows the experiment done by Geraci et al. [63]. With the fiber the movement of the test mass on the cantilever was measured. The driving mass was structured to induce a different frequency of density shift on the cantilever than the driving frequency. On the upper right an SEM image shows the test mass.

still can use Newton's law of gravity in all cases where general relativity is very well approximated through Newton's law of gravity. This is the case for low energy scales, and the low gravitational potential of small masses at distances between a nanometer and a micrometer. Newton's law of gravity is falsifiable, and the experiment discussed in this thesis is a test of it. The Yukawa potential is not entirely falsifiable. It is defined by two unknown parameters α and λ. What is possible is to rule out specific values of both parameters. This means, that the Yukawa potential with specific parameters is a falsifiable model. Another aspect is, why should we use the Yukawa potential to falsify specific possibilities of new non-Newtonian forces? An explanation based on the laws of physics is that the Yukawa potential comes into play when a force is mediated by massive particles. But there is no evidence that this has to be the case, and other potentials are possible. This is where Occam's razor comes into play. The Yukawa potential is the easiest potential with a length scale (λ) and a strength (α).

Chapter 3

Theoretical Background

Section 1.3 described the rough concept of the experiment described in this thesis This means, this chapter describes how deviations of gravity are described by using the Yukawa potential, and how it behaves when a plate-sphere geometry is used. We also discuss influences on the force measurement during the experiments like the Casimir effect, different types of Van der Waals interactions, the electrostatic interaction and the Patch effect as well as some other influences. Afterwards we describe how the force gets measured using the frequency modulation, and the influence of the amplitude of the vibration. In thhe end of this chapter, we describe some methods that were used for the data analysis.

3.1 Laws of Gravity

Currently Einstein's general relativity is the most successful theory of gravity. A great example is the first direct observation of gravitational waves [44] in 2015 after a century had passed since the first publication about general relativity and Einstein's prediction about gravitational waves [43]. Nevertheless Newton's law of gravity is still a great approximation in cases of low field energies. The potential $V_N(r)$ of Newton's Law of Gravity is given by:

$$V_N(r) = -G\frac{m \cdot M}{r} \tag{3.1}$$

where G is the gravitational constant, m and M are two interacting point masses and r is their distance. Section 1.2 explained a number of possible theories that could change Newton's potential at low field energies and low distances. Some of the modifications are explained in the further sections.

3.1.1 Yukawa Potential

3.1.1.1 Description of the Yukawa Potential

A possible new potential is commonly parameterized with the Yukawa potential. It has the advantage that it has a length scale as well as a strength. The Yukawa potential was introduced by Hideki Yukawa in 1935 [64] and was stated as:

$$Y(r) = -g^2\frac{e^{-\mu r}}{r} \tag{3.2}$$
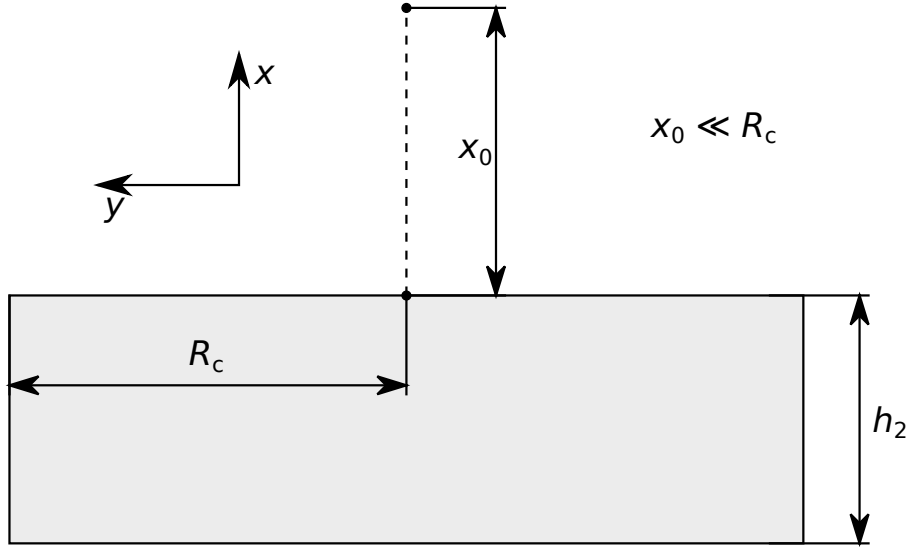
Figure 3.1: Integration over a plate for a specific point at the center.

g^2 and μ are the parameters of the Yukawa potential. g^2 is the strength of the potential and $\mu = \lambda^{-1}$ is the range of the potential.
The Yukawa part of the potential for gravity is:

$$V_Y(r) = -G\frac{m \cdot M}{r}\alpha \cdot e^{-r/\lambda} \tag{3.3}$$

This means $g^2 = G \cdot M \cdot m \cdot \alpha$, where α is the strength of the Yukawa potential in relation to Newton's law of gravity. And the complete modification of Newton's law of gravity with the Yukawa potential is given by

$$V(r) = -G\frac{m \cdot M}{r} \cdot \left(1 + \alpha \cdot e^{-r/\lambda}\right) \tag{3.4}$$

3.1.1.2 Calculation for Plate-Sphere Geometry

Eq. (3.4) is the potential for point masses. To calculate the potential for a more complex geometry, we have to go from the point masses to mass densities. First we derive the potential for the plate. For this, we integrate over the volume by assuming a cylindrical geometry of the plate with plate size defined by a radius R_c and a thickness h_2. The mass M is replaced by to ρ_2 as mass density of the cylindrical disc. r is the distance to the point, where the potential is calculated. Therefore it has the form $r = \sqrt{(x_0 + x)^2 + y^2}$, where $x_0 \geq 0$ is the minimum distance between the point and the plate. These definitions can be seen in Fig. 3.1. The potential for the plate of the Yukawa part of gravity is given by[1]:

$$V(x_0) = -\int_0^{h_2} dx \int_0^{R_c} dy \cdot y \int_0^{2\pi} d\varphi\, G\frac{\rho_2}{r}\alpha e^{-r/\lambda} \tag{3.5}$$

---

[1]m from Eq. (3.4) is omitted from this calculation, because we only calculate the field of the disc without any other mass near the disc at this point.

Define $\gamma = 2\pi\rho_2 G$.

$$V(x_0) = -\gamma \int_0^{h_2} \mathrm{d}x\,\alpha \int_0^{R_c} \mathrm{d}y \cdot \frac{y}{\sqrt{(x0+x)^2 + y^2}} \mathrm{e}^{-\frac{\sqrt{(x_0+x)^2+y^2}}{\lambda}} \tag{3.6}$$

$$= -\gamma \int_0^{h_2} \mathrm{d}x\,\alpha\lambda \left(\mathrm{e}^{-\frac{\sqrt{(x_0+x)^2+R_c^2}}{\lambda}} - \mathrm{e}^{-\frac{|x_0+x|}{\lambda}} \right) \tag{3.7}$$

$$\tag{3.8}$$

With $R_c \gg |x_0 + x|$ and $R_c \gg \lambda$, $\mathrm{e}^{-\frac{\sqrt{(x_0+x)^2+R_c^2}}{\lambda}} \to 0$

$$V(x_0) \approx +\gamma \int_0^{h_2} \mathrm{d}x\,\alpha\lambda\mathrm{e}^{\frac{-x_0-x}{\lambda}} \tag{3.9}$$

$$= -\gamma\alpha\lambda^2\mathrm{e}^{\frac{-x-x_0}{\lambda}}\Big|_0^{h_2} \tag{3.10}$$

$$= \gamma\alpha\lambda^2 \left(\mathrm{e}^{\frac{-x_0}{\lambda}} - \mathrm{e}^{\frac{-h_2-x_0}{\lambda}} \right) \tag{3.11}$$

$$V(x_0) = \alpha\gamma\lambda^2\mathrm{e}^{-\frac{x_0}{\lambda}} \left(1 - \mathrm{e}^{\frac{-h_2}{\lambda}} \right) \tag{3.12}$$

With the potential $V(x_0)$, the gravitational acceleration g can be calculated:

$$V_Y(x_0) \approx -\gamma \left(\alpha\lambda^2\mathrm{e}^{-\frac{x_0}{\lambda}} \left(1 - \mathrm{e}^{\frac{-h_2}{\lambda}} \right) \right) \tag{3.13}$$

$$g_Y(x_0) = \frac{\partial V_Y(x_0)}{\partial x_0} \tag{3.14}$$

$$\approx \gamma \left(\alpha\lambda\mathrm{e}^{-\frac{x_0}{\lambda}} \left(1 - \mathrm{e}^{-h_2/\lambda} \right) \right) \tag{3.15}$$

To obtain the total force between the two bodies, we have to integrate over the mass density of the second body, in this case a sphere. A circle with radius r has an area $A = \pi r^2$. The share of the force is identical for every point on the circle. It changes only with the distance, which is represented by x_0. At each different x_0, the equipotential circle has a different radius $r(x)$. With a distance d between the nearest point on the sphere to the plate, and a radius R for the sphere, the center of the sphere is at point $d + R$. These definitions are shown in Fig. 3.2. For any x_0 within the sphere, r^2 is defined and can be calculated using the Pythagorean theorem to $r^2 = R^2 - (R^2 - 2R(x_0 - d) + (x_0 - d)^2)$.

$$F_Y \approx \int_{d+h_1}^{d} \mathrm{d}x_0 \rho_1 \gamma A \cdot \left(\alpha\lambda\mathrm{e}^{-\frac{x_0}{\lambda}} \cdot \left(1 - \mathrm{e}^{-\frac{h_2}{\lambda}} \right) \right) \tag{3.16}$$

$$\approx \int_{d+h_1}^{d} \mathrm{d}x_0 \rho_1 \gamma\pi \left(2R(x_0 - d) - (x_0 - d)^2 \right) \cdot \left(\alpha\lambda\mathrm{e}^{-\frac{x_0}{\lambda}} \cdot \left(1 - \mathrm{e}^{-\frac{h_2}{\lambda}} \right) \right) \tag{3.17}$$

Define $\gamma_1 = \pi\rho_1\gamma\alpha$.

$$F_Y \approx \gamma_1\lambda \cdot \left(1 - \mathrm{e}^{-\frac{h_2}{\lambda}} \right) \int_{d+h_1}^{d} \mathrm{d}x_0 \left(2R(x_0 - d) - (x_0 - d)^2 \right) \cdot \mathrm{e}^{-\frac{x_0}{\lambda}} \tag{3.18}$$

21
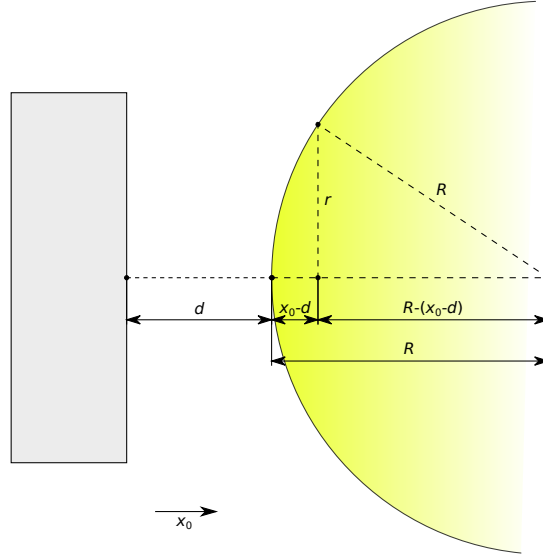
Figure 3.2: Integration of the sphere over the gravitational field of the plate.

$$= \gamma_1 \lambda^2 \left(1 - e^{-\frac{h_2}{\lambda}}\right) e^{-\frac{d+h_1}{\lambda}} \left(-h_1^2 + 2h_1(R - \lambda) + 2\lambda \left(e^{h_1/\lambda} - 1\right) \underbrace{(\lambda - R)}_{\approx -R}\right)$$
(3.19)

$$= \gamma_1 \lambda^2 \left(1 - e^{-\frac{h_2}{\lambda}}\right) \left(-2\lambda e^{\frac{h_1 - d - h_1}{\lambda}} R + \underbrace{e^{-\frac{d+h_1}{\lambda}} \underbrace{\left(-h_1^2 + 2h_1(R - \lambda) + 2\lambda R\right)}_{\approx 0}}_{\approx 0}\right)$$
(3.20)

$$= -\gamma_1 \lambda^2 \cdot \left(1 - e^{-\frac{h_2}{\lambda}}\right) 2\lambda e^{-d/\lambda} R$$
(3.21)

$$= -4\pi^2 \rho_1 \rho_2 G \alpha \lambda^3 R e^{-d/\lambda} \left(1 - e^{-\frac{h_2}{\lambda}}\right)$$
(3.22)

This result is a very good approximation for $e^{-\frac{h_1}{\lambda}} \ll 1$. For example, if $h_1 = 100\,\mu$m and $\lambda = 10\,\mu$m $\Rightarrow 4.5 \cdot 10^{-5} \ll 1$. This means, if the spherical cap (or lens) is about 10 times *higher* than the range λ of the potential we want to measure, the approximation of Eq. (3.22) can be used.[2]

In a real experiment, neither the plate nor the sphere are built from a single material. The sphere consists of a base material, an adherent layer and a coating. Therefore at least three different densities are necessary. The outer two layers have a thickness of t_c for the coating and t_a for the adherent layer. In the first stage, only the sphere has a coating:

For the coating, the force is calculated assuming the whole sphere is made of its material. For the adherent layer, the radius of the sphere changes by the thickness of the sphere. And for the base material, the same is applied, but the radius is changed by the sum of both layer thicknesses. This leads to a

---

[2]See also Bordag et al. [65].

change of ρ_1 to:

$$R \cdot \rho_1 = R\rho_c + (R - t_c)\left(\rho_a - \rho_c\right)\mathrm{e}^{-\frac{t_c}{\lambda}} + (R - t_c - t_a)\left(\rho_b - \rho_a\right)\mathrm{e}^{-\frac{t_c+t_a}{\lambda}} \quad (3.23)$$

With $R \gg t_c$ and $R \gg t_a$:

$$\rho_1 = \rho_c + (\rho_a - \rho_c)\mathrm{e}^{-\frac{t_c}{\lambda}} + (\rho_b - \rho_a)\mathrm{e}^{-\frac{t_c+t_a}{\lambda}} \quad (3.24)$$

For ρ_2, this is the same, but with possibly other materials and thickness values:

$$\rho_2 = \hat{\rho}_c + (\hat{\rho}_a - \hat{\rho}_c)\mathrm{e}^{-\frac{\hat{t}_c}{\lambda}} + (\hat{\rho}_b - \hat{\rho}_a)\mathrm{e}^{-\frac{\hat{t}_c+\hat{t}_a}{\lambda}} \quad (3.25)$$

3.1.2 Power Law

In particle physics, an unknown gravitational potential is typically described by a power law modification [66] [67]:

$$V = -G\frac{Mm}{r}\left(1 + \left(\frac{\lambda}{r}\right)^n\right) \quad (3.26)$$

with r as distance between the point masses and λ as the range of the force as well as n as the exponent of the power law. The ADD model [11][3] can be best expressed as a power law. Therefore, the approximation as Yukawa-potential is not possible for $r \ll \lambda$. But as long as the distances are at about λ or larger, the approximation as a Yukawa-potential is valid.

3.1.3 Infinite Derivative Gravity

One approach to overcome problems of general relativity (GR) is called *Infinite Derivative Gravity* [68] or short IDG. One of these problems is, that the Newtonian limit of GR leads to a singularity, IDG does not have this problem [69]. Also it is renormalizable at the quantum level [70] and it is consistent with cosmological observations without the cosmological constant of GR [71]. Edholm [72] described how this theory would change the Newtonian potential at small distances and got an oscillating potential. Perivolaropoulos analyzed experiments with that [73]. One effective oscillation potential from Perivolaropoulos is:

$$V(r) = \frac{1}{2r^2} - \frac{1}{r}\left(1 + \frac{\cos\left(\hat{m}r\right)}{3}\right) \quad (3.27)$$

where $\hat{m}$ is a natural number that describes the potential and r is the distance between point masses. See Fig. 3.3 for a comparison between a bound Newtonian potential and the oscillating potential. The oscillations of the potential are spatial, and they cancel out in most cases of Newtonian potentials. Perivolaropoulos has shown that this potential fits also well the Kapner [60] experiment using a rotating source mass in the sub-millimeter range. See also section 2.2.4 for a description of that experiment.

---

[3]See section 1.2 for a short description on the ADD model
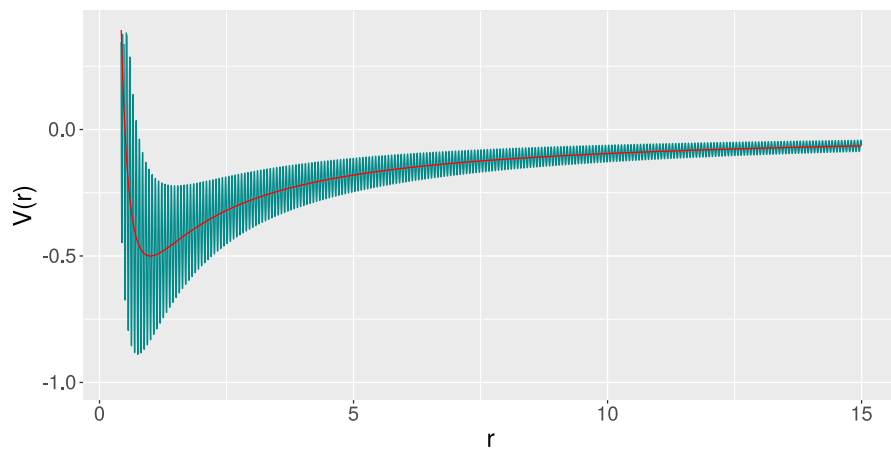
Figure 3.3: Example of the oscillating gravity potential [73] with the formula $V(r) = \frac{1}{2r} - \frac{1}{r}\left(1 + \frac{\cos(\hat{m}r)}{3}\right)$ and $\hat{m} = 100$. It is superposed with the corresponding Newtonian potential.
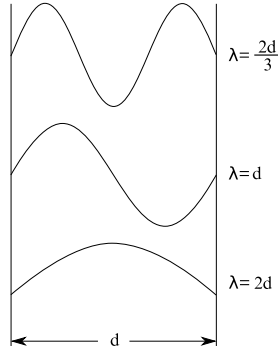
Figure 3.4: Casimir effect in 1D. Between two *points* (shown here as lines to show the stationary waves), only stationary waves are possible, because of the boundary condition that the electric field has to be zero at the metal surface.

3.2 The Casimir Effect

The Casimir effect was predicted by Hendrik Casimir in 1948 [9]. It states, that a force is acting between two conducting surfaces. This type of interaction is a quantized electromagnetic field, i.e. virtual photons.

3.2.1 The 1D-Casimir Effect

Before we calculate the Casimir Effect for the real 3D case, we start with the 1D case, because it is easier to follow. A harmonic oscillator has in quantum mechanics a zero-point energy, that goes back to the uncertainty principle. One example of a quantum harmonic oscillator is an electromagnetic wave between two perfectly conducting points[4]. There could be different energy states. The energy state *one* is the case, when one photon is in the system, the energy state *two* means there are two photons and so on.

$$E_m = \left(\frac{1}{2} + m\right)\omega\hbar \tag{3.28}$$

with $m \in \mathbb{N}$. The case with no photons in the system is the zero-point energy:

$$E_0 = \frac{1}{2}\omega\hbar \tag{3.29}$$

ω is the angular frequency of the photon. Coming back to the case of two perfectly conducting points of distance d. Then there are different types of harmonic oscillators possible. Only those types with a frequency corresponding to an stationary wave are possible. That means each stationary wave corresponds to a different harmonic oscillator. A stationary wave can have the following wavelength:

$$\lambda = \frac{2d}{n} \tag{3.30}$$

where n is the number of the harmonic. With $c = \lambda f$, the possible angular frequencies are:

$$\omega(n) = n\frac{\pi c}{d} \tag{3.31}$$

---

[4]A perfectly conducting point is the 1D repersentation of a perfectly conducting plate.

And for each angular frequency, the zero-point energy would be:

$$E_0(n) = \frac{1}{2}\omega(n)\hbar = n\frac{1}{2}\frac{\pi c\hbar}{d} \tag{3.32}$$

The total energy of the system is the sum of all zero point energies:

$$E_{\text{tot}} = \sum_{n=1}^{\infty} n\frac{\pi c\hbar}{2d} = \frac{\pi c\hbar}{2d}\sum_{n=1}^{\infty} n \tag{3.33}$$

This sum is divergent, i.e. — it sums up to ∞. Note that there is the concept of terminating the summation when the wavelength λ goes below the Planck length. This was done by Weinberg [8] in his paper on the cosmological constant problem.
There are two different ways to get a meaningful result from this divergent sum, both involve regularization.

3.2.1.1 Zeta Function Regularization

Zeta function regularization is a method to remove infinity from a quantum dynamics calculations, see Razmi et al. [74]. Riemanns ζ-function is defined by

$$\zeta(s) = \sum_{n=1}^{\infty} \frac{1}{n^s} \tag{3.34}$$

In the case of $s > 1$, the sum is convergent for every real number[5]. Riemann said that for each complex number s, this function can be continued analytically [75, 2.7.3]. The analytical continuation is done with the functional equation:

$$\zeta(s) = 2^s\pi^{s-1}\sin\left(\frac{\pi s}{2}\right)\Gamma\left(1-s\right)\zeta\left(1-s\right) \tag{3.35}$$

where $\Gamma(s)$ is the gamma function, a continuation of the factorial for all complex numbers. For $s = -1$, the sum would be:

$$\zeta(-1) = \sum_{n=1}^{\infty} \frac{1}{n^{-1}} = \sum_{n=1}^{\infty} n \tag{3.36}$$

Using this, Eq. (3.33) can be written as:

$$E_{\text{tot}} = \frac{\pi c\hbar}{2d}\zeta(-1) \tag{3.37}$$

The following value is obtained using the analytical continuation of Riemann's ζ-function for $s < 1$ from Eq. (3.35):

$$\zeta(-1) = -\frac{1}{2\pi^2}\Gamma(2)\zeta(2) \stackrel{\Gamma(2)=1!=1}{=} -\frac{1}{2\pi^2}\zeta(2) \stackrel{\zeta(2)=\frac{\pi^2}{6}}{=} -\frac{1}{12} \tag{3.38}$$

This method of finding the corresponding ζ-function to an divergent sum and using the analytical continuation of it as a finite value is called ζ-function regularization [75, 2.7.3.4]. This leads to a total energy of:

$$E_{\text{tot}} = -\frac{\pi c\hbar}{24d} \tag{3.39}$$

The negative sign means, that the corresponding force would be attractive.

---

[5]Actually, this definition is convergent $\forall s \in \mathbb{C}$ with $\Re(s) > 1$

3.2.1.2 Difference between E_d and E_∞

The other method to calculate the Casimir effect for the 1D case is the more obvious one from a physical point of view. The idea is to find the difference between the case of two points with distance d and the case where the distance goes to infinity.

The case of a distance of infinity means the sum of all zero-point energies outside the two points of distance d. In this case, there are not only positive integer numbers n allowed, but every possible positive real number. This means, the sum transforms into an integral:

$$E_{\text{outside}} = \frac{1}{2} \frac{\hbar c \pi}{d} \int\limits_0^\infty n \mathrm{d}n \tag{3.40}$$

This integral is also divergent. But we can assume, that at very small wavelengths, every metal becomes transparent to that wavelength. This wavelength is called cutoff wavelength. To represent that in both formulas, we have to introduce a cutoff function $g(n) = \mathrm{e}^{-\alpha n}$. α is a parameter representing the frequency range of the field and is a very small number, but $\alpha > 0$. Afterwards we can write the difference of both energies:

$$\Delta E = E_{\text{tot}} - E_{\text{outside}} = \frac{\pi c \hbar}{2d} \sum_{n=1}^\infty n \mathrm{e}^{-\alpha n} - \frac{\hbar c \pi}{2d} \int\limits_0^\infty n \mathrm{e}^{-\alpha n} \mathrm{d}n \tag{3.41}$$

The next step is using the Euler-MacLaurin formula. The Euler-MacLaurin formula is given by [75, 0.7.1.3]:

$$\sum_{x=0}^m f(x) = \int\limits_0^m f(x)\mathrm{d}x + \frac{f(0) + f(m)}{2} + S_m \tag{3.42}$$

with

$$S_m = \sum_{p=1}^m \left(\frac{B_{2p}}{(2p)!} \frac{\mathrm{d}^{(2p-1)} f}{\mathrm{d}x^{(2p-1)}}(x) \bigg|_{x=0} \right) + R_m \tag{3.43}$$

where B_{2p} are the Bernoulli numbers and R_m is a remainder term. First of all, the formula has been rearranged to match the structure of Eq. (3.41):

$$\sum_{x=1}^m f(x) - \int\limits_0^m f(x)\mathrm{d}x = \frac{f(0) + f(m)}{2} - f(0) - S_m \tag{3.44}$$

with $f(n) = n\mathrm{e}^{-\alpha n}$ and $f(0) = 0$. In our case $m \to \infty$.

$$\lim_{m\to\infty} f(m) = \frac{\lim_{m\to\infty} m}{\lim_{m\to\infty} \mathrm{e}^{\alpha m}} \overset{\text{L'Hôpital}}{=} \frac{1}{\lim_{m\to\infty} \alpha \mathrm{e}^{\alpha m} \to \infty} = 0 \tag{3.45}$$

The relevant Bernoulli numbers are: $B_2 = \frac{1}{6}$ and $B_4 = -\frac{1}{30}$. The first term of S_∞ is:

$$\frac{B_2}{2} \frac{\mathrm{d}n\mathrm{e}^{-\alpha n}}{\mathrm{d}n} = \frac{B_2}{2} \left(\mathrm{e}^{-\alpha n} - \alpha n \mathrm{e}^{-\alpha n} \right) \overset{n=0}{=} \frac{B_2}{2} \cdot 1 = \frac{1}{12} \tag{3.46}$$

27

And the second term of S_∞ is:

$$\frac{B_4}{4!}\frac{\mathrm{d}^3 n\mathrm{e}^{-\alpha n}}{\mathrm{d}^3 n} = \frac{B_4}{24}\left(3\alpha^2\mathrm{e}^{-\alpha n} - \alpha^3 n\mathrm{e}^{-\alpha n}\right) \stackrel{n=0}{=} \frac{B_4}{8}\alpha^2 = \frac{1}{240}\alpha^2 \qquad (3.47)$$

With a very small $\alpha > 0$, the second term is much smaller than the first term, and also every higher order term gets irrelevant. This leads to the energy difference of:

$$\Delta E = -\frac{\pi c\hbar}{24d} \qquad (3.48)$$

Which is identical to Eq. (3.39).

3.2.2   The Casimir Effect in 3D

Casimir calculated the effect in 3D. That means, we have two perfectly conducting plates at distance d. The plates are quadratic with side length $L \gg d$. First difference to the 1D case is, that electromagnetic waves can have two different polarizations. Therefore the sum needs a factor 2. On the other hand, there are not only perpendicular waves between the plates possible, but any waves in any other direction. Definition of the axes:

$$0 \;\leq\; x \leq L \qquad (3.49)$$
$$0 \;\leq\; y \leq L \qquad (3.50)$$
$$0 \;\leq\; z \leq d \qquad (3.51)$$

For each direction there are wave-numbers:

$$k_x \;=\; \frac{\pi}{L}n_x \qquad (3.52)$$
$$k_y \;=\; \frac{\pi}{L}n_y \qquad (3.53)$$
$$k_z \;=\; \frac{\pi}{d}n_z \qquad (3.54)$$

L is large compared to d, therefore k_x and k_y can be assumed to be continuous variables. The overall wave number is:

$$k = \sqrt{k_x^2 + k_y^2 + k_z^2} = \sqrt{k_x^2 + k_y^2 + \left(\frac{\pi}{d}n_z\right)^2} \qquad (3.55)$$

$$E_{\mathrm{sum}} = \frac{L^2\hbar c}{\pi^2}\sum_{n=0}^{\infty}{}' \int_0^\infty\int_0^\infty k\mathrm{d}k_x\mathrm{d}k_y \qquad (3.56)$$

The factor $\frac{L^2}{\pi^2}$ is obtained by integrating over k_x and k_y rather than integrating only over n_x or n_y. Note that in the 3D case n starts at 0. That is because there could be waves propagating only in the $k_x - k_y$ plane, and not in k_z. But in that case, there are not two different polarizations for $n = 0$, because there is no wave in k_z. That is what the $\sum'$ means. When calculating the sum a factor of $\frac{1}{2}$ has to be added to the first summand in case of $n = 0$. We also want to compare the energies outside the plates:

$$E_{\mathrm{vac}} = \frac{L^2\hbar c}{\pi^2}\iiint_0^\infty k\mathrm{d}k_x\mathrm{d}k_y\mathrm{d}n_z \qquad (3.57)$$

And the difference between both energies:

$$\Delta E = E_{\text{sum}} - E_{\text{vac}} = \frac{L^2 \hbar c}{\pi^2} \left(\sum_{n=0}^{\infty}{}' \int_0^\infty \int_0^\infty k \mathrm{d}k_x \mathrm{d}k_y - \int\!\!\!\int\!\!\!\int_0^\infty k \mathrm{d}k_x \mathrm{d}k_y \mathrm{d}n_z \right) \quad (3.58)$$

Transforming k to polar coordinates u, θ in the k_x, k_y plane gives:

$$\Delta E = \frac{L^2 \hbar c}{\pi^2} \frac{\pi}{2} \left(\sum_{n=0}^{\infty}{}' \int_0^\infty u \left(u^2 + \frac{n^2 \pi^2}{d^2} \right)^{1/2} \mathrm{d}u - \int\!\!\!\int_0^\infty u \left(u^2 + \frac{n^2 \pi^2}{d^2} \right)^{1/2} \mathrm{d}u \mathrm{d}n \right)$$
$$(3.59)$$

where $\mathrm{d}k_x \mathrm{d}k_y = u \mathrm{d}u \mathrm{d}\theta$ and n means n_z from above. The $\frac{\pi}{2}$ came from the integral over $\theta \in \left[0, \frac{\pi}{2} \right)$.
Similar to the 1D case a cutoff function $g(k)$ has to be introduced. It is assumed that metals are transparent to electromagnetic waves of very high frequencies, which is represented by the cutoff function.
The cutoff function $g(0) = 1$ for small k and for large k it is $g(\infty) = 0$.

$$\Delta E = \frac{L^2 \hbar c}{2\pi} \left(\sum_{n=0}^{\infty}{}' \int_0^\infty u \left(u^2 + \frac{n^2 \pi^2}{d^2} \right)^{1/2} g \left(\left(u^2 + \frac{n^2 \pi^2}{d^2} \right)^{1/2} \right) \mathrm{d}u \right.$$
$$\left. - \int\!\!\!\int_0^\infty u \left(u^2 + \frac{n^2 \pi^2}{d^2} \right)^{1/2} g \left(\left(u^2 + \frac{n^2 \pi^2}{d^2} \right)^{1/2} \right) \mathrm{d}u \mathrm{d}n \right) \quad (3.60)$$

The next step is to substitute the integration variable u by $v = u^2 d^2 / \pi^2$. For the new integration variable follows:

$$u = \sqrt{\frac{v \pi^2}{d^2}} = \frac{\pi}{d} \sqrt{v} \quad (3.61)$$

$$\frac{\mathrm{d}u}{\mathrm{d}v} = \frac{\pi}{d} \frac{1}{2} \frac{1}{\sqrt{v}} \quad (3.62)$$

$$\mathrm{d}u = \frac{\pi}{2d} \frac{1}{\sqrt{v}} \mathrm{d}v \quad (3.63)$$

$$u \mathrm{d}u = \frac{\pi^2}{2d^2} \mathrm{d}v \quad (3.64)$$

$$\left(u^2 + \frac{n^2 \pi^2}{d}^2 \right)^{1/2} = \frac{\pi}{d} \left(v + n^2 \right)^{1/2} \quad (3.65)$$

$$\Delta E = \frac{L^2 \hbar c}{2\pi} \frac{\pi^3}{2d^3} \left(\sum_{n=0}^{\infty}{}' \int_0^\infty \left(v + n^2 \right)^{1/2} g \left(\frac{\pi}{d} \left(v + n^2 \right)^{1/2} \right) \mathrm{d}v \right.$$
$$\left. - \int\!\!\!\int_0^\infty \left(v + n^2 \right)^{1/2} g \left(\frac{\pi}{d} \left(v + n^2 \right)^{1/2} \right) \mathrm{d}v \mathrm{d}n \right) \quad (3.66)$$

The function we want to apply the Euler-MacLaurin formula from Eq. (3.42) on, is:

$$f(n) = \int\limits_0^\infty \left(v + n^2\right)^{1/2} g\left(\frac{\pi}{d}\left(v + n^2\right)^{1/2}\right) \mathrm{d}v \tag{3.67}$$

Next step for Eq. (3.66) is:

$$\Delta E = \frac{L^2\hbar c}{2\pi}\frac{\pi^3}{2d^3}\left(\frac{1}{2}f(0) + \sum_{n=1}^\infty f(n) - \int\limits_0^\infty f(n)\mathrm{d}n\right) \tag{3.68}$$

$\lim\limits_{n\to\infty} f(n) = 0$, because $\lim\limits_{x\to\infty} g(x) = 0$, and an integral over zero is zero.
The cutoff function $g(n)$ is 1 for small n, and 0 for very large n. Therefore the derivative of $g'(n) = 0$ for small n. $f(n)$ can also be written as an integral over w, but with a lower limit of n^2:

$$f(n) = \int\limits_{n^2}^\infty w^{1/2} g\left(\frac{\pi}{d}w^{1/2}\right)\mathrm{d}w \tag{3.69}$$

The derivatives of $f(n)$ are:

$$f'(n) = -2n^2 g(\frac{\pi}{d}n) \stackrel{n=0}{=} 0 \tag{3.70}$$

$$f''(n) = -4n g(\frac{\pi}{d}n) \stackrel{n=0}{=} 0 \tag{3.71}$$

$$f'''(n) = -4g(\frac{\pi}{d}n) \stackrel{n=0}{=} -4 \tag{3.72}$$

$$f''''(n) = 0 \tag{3.73}$$

The Euler-MacLaurin formula in this case delivers:

$$\sum_{n=1}^\infty f(n) - \int\limits_0^\infty f(n)\mathrm{d}n = -\frac{1}{2}f(0) - \frac{1}{12}f'(0) + \frac{1}{720}f'''(0) + \ldots \tag{3.74}$$

Including Eq. (3.74) into Eq. (3.68), we obtain:

$$\Delta E = \frac{L^2\hbar c\pi^2}{4d^3}\left(\frac{1}{2}f(0) - \frac{1}{2}f(0) - \frac{1}{12}f'(0) + \frac{1}{720}f'''(0) + \ldots\right) \tag{3.75}$$

Putting in the numbers:

$$\Delta E = \frac{L^2\hbar c\pi^2}{4d^3}\left(-\frac{0}{12} + \frac{-4}{720}\right) = -\frac{L^2\hbar c\pi^2}{720d^3} \tag{3.76}$$

which is the same result as in Casimirs original paper.
To calculate the force, one has to differentiate by the distance d:

$$F_C = \frac{\mathrm{d}\Delta E}{\mathrm{d}d} = \frac{L^2\hbar c\pi^2}{240d^4} \tag{3.77}$$

3.2.3 Casimir Effect of the Sphere-Plate Geometry

It is not possible to use the method for the parallel plate Casimir effect to calculate the effect for the plate-sphere geometry. But with the proximity force theorem by Blocki et al. [76] there exists a method to use the result
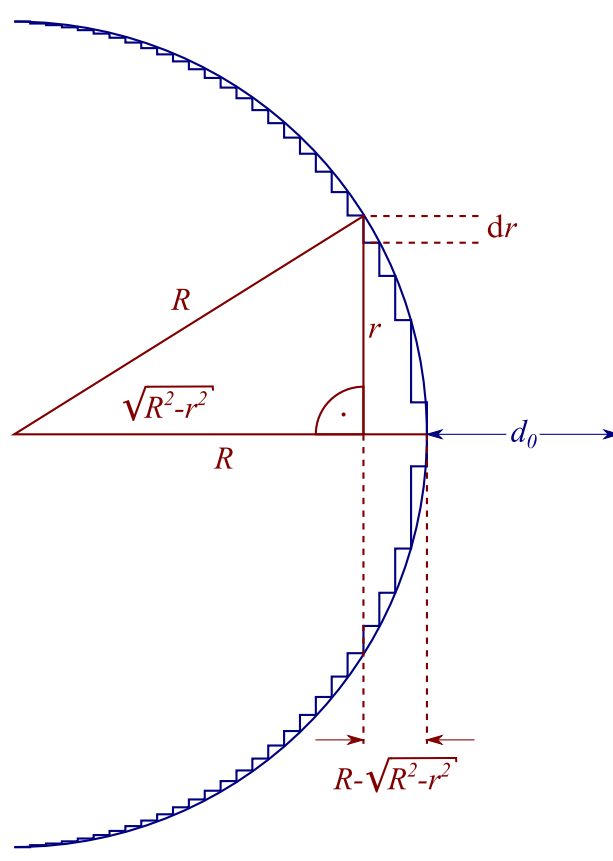
Figure 3.5: To integrate the potential over the sphere using the proximity force theorem, the force between an infinitesimal annulus parallel to the plate is summed up for each equipotential circle on the sphere. r is the inner radius of the annulus and $r + \mathrm{d}r$ is the outer radius.

from the parallel plate geometry to calculate the force of the plate-sphere geometry. The idea of the proximity force theorem is, that in cases where only a parallel surface contributes to the force, one can split up the surface of a volume to chunks of parallel surfaces with different distances. First the sphere is split into a lot of annular equipotential surfaces.

Then the area contributes with its distance to the plate to the overall potential. The area of an annulus is:

$$A = \pi(r_1^2 - r_2^2) \tag{3.78}$$

with r_1 being the outer and r_2 being the inner radius. The limits for infinitesimally thin annuli delivers the continuous case:

$$A = \int_{r_2}^{r_1} 2\pi r \mathrm{d}r \tag{3.79}$$

$$V(A) = \int_0^R 2\pi V(d(r))r\mathrm{d}r \tag{3.80}$$

For d_0 being the nearest distance of the sphere surface to the plate and R being the radius of the sphere, for the distance d we obtain:

$$d = d_0 + R - \sqrt{R^2 - r^2} \tag{3.81}$$

The term $\sqrt{R^2 - r^2}$ is the distance between the sphere center for a given annulus radius r. Now it is possible to substitute $\mathrm{d}r$ with $\mathrm{d}d$:

$$\frac{\mathrm{d}d}{\mathrm{d}r} = \frac{r}{\sqrt{R^2 - r^2}} \tag{3.82}$$

$$\mathrm{d}r = \frac{\sqrt{R^2 - r^2}}{r}\mathrm{d}d \tag{3.83}$$

$$\sqrt{R^2 - r^2} = d_0 + R - d \tag{3.84}$$

$$d(r = r_1) = d_0 \tag{3.85}$$

$$d(r = r_2) = d_0 + R \tag{3.86}$$

$$V(A) = \int_{d_0}^{d_0+R} 2\pi V(d)\,(d_0 + R - d)\,\mathrm{d}d \tag{3.87}$$

Using partial integration:

$$\int_a^b f'(x)g(x)\mathrm{d}x = f(x)g(x)\Big|_a^b - \int_a^b f(x)g'(x)\mathrm{d}x \tag{3.88}$$

With $f'(d) = V(d)$, $g(d) = d_0 + R - d$, $g'(d) = -1$ and $f(d) = \int V(d)\mathrm{d}d$:

$$V(A) = 2\pi \bigg(\underbrace{(d_0 + R - d_0)}_{=R} \left(\int V(d)\mathrm{d}d \right)(d_0)$$

$$- \underbrace{(d_0 + R - (d_0 + R))}_{=0} \left(\int V(d)\mathrm{d}d \right)(d_0 + R)$$

$$+ \int_{d_0}^{d_0+R} \int V(d)\mathrm{d}d\mathrm{d}d \bigg) \tag{3.89}$$

$$\Rightarrow V(A) = 2\pi \left(R \left(\int V(d)\mathrm{d}d \right)(d_0) + \int_{d_0}^{d_0+R} \int V(d)\mathrm{d}d\mathrm{d}d \right) \tag{3.90}$$

The corresponding force to the potential is:

$$F(A) = \frac{\mathrm{d}V}{\mathrm{d}d} = 2\pi R \underbrace{\frac{\mathrm{d}\left(\int V(d)\mathrm{d}d \right)}{\mathrm{d}d}(d_0)}_{=V(d_0)} + 2\pi \underbrace{\frac{\mathrm{d}}{\mathrm{d}d} \int_{d_0}^{d_0+R} \int V(d)\mathrm{d}d\mathrm{d}d}_{=0} \tag{3.91}$$

The second part of Eq. (3.91) is zero, because the definite integral does not depend on d anymore. As result for any force between a sphere and a plate, where the surface approximation of the PFA (proximity force approximation) is valid, is:

$$F(A, d_0) = 2\pi R V(d_0) \tag{3.92}$$

where $V(d_0)$ is the potential per unit area of the parallel plate case. In the case of the Casimir effect this results in:

$$F_C(d_0, R) = R \frac{\hbar c \pi^3}{360} \frac{1}{d_0^3} \tag{3.93}$$

3.2.4 Casimir Effect for Real Metals

Real metals are not perfectly conducting. A perfectly conducting metal would also be a perfect mirror for each wavelength. Gold is not a perfect mirror for blue light, therefore it is not perfectly conducting. The conductivity of real metals is also temperature dependent.
Lifshitz modelled the Casimir effect between dielectric materials [77]. The result for the force per unit area between two plates with dielectric functions ϵ_1 and ϵ_2 and in between a medium with ϵ_3 delivers:

$$F(d) = \frac{k_B T}{\pi c^3} \sum_{n=0}^{\infty}{}' \epsilon_3^{3/2} \xi_n^3 \int_1^{\infty} p^2 \left(\left(\left(\frac{(s_1 + p)(s_2 + p)}{(s_1 - p)(s_2 - p)} \mathrm{e}^{\frac{2p\xi_n}{c} l \sqrt{\epsilon_3}} - 1 \right)^{-1} \right. \right.$$
$$\left. \left. + \left(\frac{(s_1 + p\epsilon_1/\epsilon_3)(s_2 + p\epsilon_2/\epsilon_3)}{(s_1 - p\epsilon_1/\epsilon_3)(s_2 - p\epsilon_2/\epsilon_3)} \mathrm{e}^{\frac{2p\xi_n}{c} l \sqrt{\epsilon_3}} - 1 \right)^{-1} \right) \mathrm{d}p \right. \tag{3.94}$$

where $s_i = \sqrt{\epsilon_i/\epsilon_3 - 1 + p^2}$ and $\epsilon_j = \epsilon_j(i\xi)$. ξ is the complex frequency $i\xi = \omega$. In case of vacuum in between and both plates of the same medium the dielectric functions are $\epsilon_3 = 1$ and $\epsilon_1 = \epsilon_2 = \epsilon$. The Lifshitz-formula reduces to:

$$F(d) = \frac{k_B T}{\pi c^3} \sum_{n=0}^{\infty}{}' \xi_n^3 \int_1^{\infty} p^2 \left(\left(\frac{(s + p)^2}{(s - p)^2} \mathrm{e}^{\frac{2p\xi_n}{c} l} - 1 \right)^{-1} + \left(\frac{(s + p\epsilon)^2}{(s - p\epsilon)^2} \mathrm{e}^{\frac{2p\xi_n}{c} l} - 1 \right)^{-1} \right) \mathrm{d}p$$
$$\tag{3.95}$$

where $s = \sqrt{\epsilon - 1 + p^2}$.
$\epsilon(i\xi)$ is given by:

$$\epsilon(i\xi) = 1 + \frac{2}{\pi} \int_0^{\infty} \frac{\omega \epsilon''(\omega)}{\omega^2 + \xi^2} \mathrm{d}\omega \tag{3.96}$$

where ϵ'' is the imaginary part of dielectricity.

3.2.4.1 Real Metals without Thermal Effect

In case of $k_\mathrm{B} T d / \hbar c \ll 1$ the passage to the limit of continuous phyics can be made, thus instead of summation an integration is carried out, where $k_\mathrm{B} T$ are replaced by $\hbar \omega$, see Lifshitz for further details. When d is larger than the wavelength that characterizes the absorption spectrum of the body, the integral can be simplified: The values of p where $p\xi d/c \sim 1$ are dominant in

the integration because of the exponential factor, which leads to a $p \gg 1$. In that case $s \approx p$. The first term of Eq. (3.95) is zero and for the second term a new variable of integration can be substituted: $x = 2dp\xi/c$. This leads to:

$$F = \frac{\hbar c}{32\pi^2 d^4} \int\limits_0^\infty \int\limits_1^\infty \frac{x^3}{p^2} \left(\frac{(s+p)^2}{(s-p)^2} \mathrm{e}^x - 1 \right)^{-1} + \left(\frac{(s+p\epsilon)^2}{(s-p\epsilon)^2} \mathrm{e}^x - 1 \right)^{-1} \mathrm{d}p \mathrm{d}x$$

(3.97)

with $\epsilon = \epsilon(ixc/2pd)$. In this case, in the exponential only $x \sim 1$ are relevant to the integration, for large d the argument for ϵ is nearly zero for most of the integration time. Therefore ϵ can be replaced with the value of the function in case of $\xi = 0$:

$$F = \frac{3\hbar c}{32\pi^2 d^4} \int\limits_0^\infty \int\limits_1^\infty \frac{x^3}{p^2} \left(\frac{(s(0)+p)^2}{(s(0)-p)^2} \mathrm{e}^x - 1 \right)^{-1} + \left(\frac{(s(0)+p\epsilon(0))^2}{(s(0)-p\epsilon(0))^2} \mathrm{e}^x - 1 \right)^{-1} \mathrm{d}p \mathrm{d}x$$

(3.98)

This reduces to the integral:

$$F = \frac{3\hbar c}{16\pi^2 d^4} \int\limits_1^\infty \frac{1}{p^2} \left(\frac{(s(0)-p)^2}{(s(0)+p)^2} + \frac{(s(0)-p\epsilon(0))^2}{(s(0)+p\epsilon(0))^2} \right) \mathrm{d}p$$

(3.99)

For a metal $\epsilon(0) \to \infty$, and the result of the integral is the usual Casimir effect. But this result is an approximation, and when we want to get the next term of the expansion, we have to take other values of ϵ into account. Expanding the integral with powers of $\frac{1}{d}$ gives, using Drudes model[6] of metals:

$$F = \frac{\hbar c}{32\pi^2 d^4} \left(\frac{2\pi^4}{15} - \frac{c}{ed} \sqrt{\frac{m}{\pi N}} \int\limits_0^\infty \frac{x^4 \mathrm{e}^x}{(\mathrm{e}^x - 1)^2} \mathrm{d}x \int\limits_1^\infty \frac{p^2 + 1}{p^4} \mathrm{d}p \right)$$

(3.100)

or:

$$F = \frac{\hbar c \pi}{240 d^4} \left(1 - 7.2 \frac{c}{ed} \sqrt{\frac{m}{N}} \right)$$

(3.101)

3.2.4.2   Temperature Dependent Casimir Effect

The Lifshitz formula can also be used to calculate the temperature dependent Casimir effect. In case of metals using the Drude model, Lifshitz obtained:

$$F = \frac{k_B T}{8\pi d^3} \left(1 + 2 \left(\frac{4\pi k T d}{\hbar c} \right) \mathrm{e}^{-\frac{4\pi k T d}{\hbar c}} \right)$$

(3.102)

To calculate the force for the sphere-plate geometry, one has first to calculate the potential before using PFA:

$$V = \int F(d) = -\frac{k_B T}{16\pi d^2} \left(1 + 2 \left(\frac{4\pi k T d}{\hbar c} \right) \mathrm{e}^{-\frac{4\pi k T d}{\hbar c}} \right)$$

(3.103)

Using PFA Eq. (3.92) delivers for the first term:

$$F_{\text{sphere}} = R \frac{k_B T}{8 d^2}$$

(3.104)

---

[6]For the Drude model see later in this chapter.

3.2.4.3 Drude Model

Drude made the first kinetic theory of free electron movements in metals in the year 1900 [78] [79] after the discovery of the electron by J. J. Thomson [80]. Drudes model based on the idea, that electrons in a metal have the same behavior as molecules in an ideal gas. The Drude model was the first model that tried to explain the resistance of a metal and it was also used to explain the color of metals. The color of metals depends on their interaction with electromagnetic waves, which is the same reason that the Casimir effect exists. With the difference, that the Casimir effect assumes perfect conductivity at every frequency and the Drude model is a model, that explains imperfect conductivity. Therefore the Drude model is used to correct the Casimir effect for real world metals. The current response, also known as plasmons, to an electromagnetic field is given by:

$$\sigma(\omega) = \frac{\sigma_0}{1 + i\omega\tau} \tag{3.105}$$

where ω is the frequency of the wave and τ is the time the electron needs to accelerate.
The dielectric function ϵ is given by:

$$\epsilon = 1 + \frac{P}{\epsilon_0 E} \tag{3.106}$$

where P is the polarization density, $P = -nex$. n is the number of electrons and x is the displacement. Between the electrical field E and the polarization density P there is the following relationship:

$$P = -\frac{ne^2}{m\omega^2}E \tag{3.107}$$

Which delivers the frequency dependence of the dielectric function:

$$\epsilon(\omega) = 1 - \frac{ne^2}{\epsilon_0 m\omega} \tag{3.108}$$

The frequency where the real part of the dielectric function drops to zero and changes its sign is called plasma frequency ω_p and is usually the plasmon frequency:

$$\omega_p = \sqrt{\frac{ne^2}{\epsilon_0 m}} \tag{3.109}$$

3.2.4.4 Comparison Drude model and Plasma model

To calculate the Casimir effect for gold at finite temperature, the real part of the dielectric functions has to be used to get an accurate result at finite temperatures. Fig. 3.6 shows the measured dielectric constants of gold. Unfortunately, it is not possible to measure the dielectricity for gold at every frequency. For that case, the dielectric function is extrapolated. For example by using the Drude model.
A more accurate model of the Casimir effect at finite temperature from Eq. (3.104) has been developed by Sushkov et al. [82] and delivers for the Drude model:

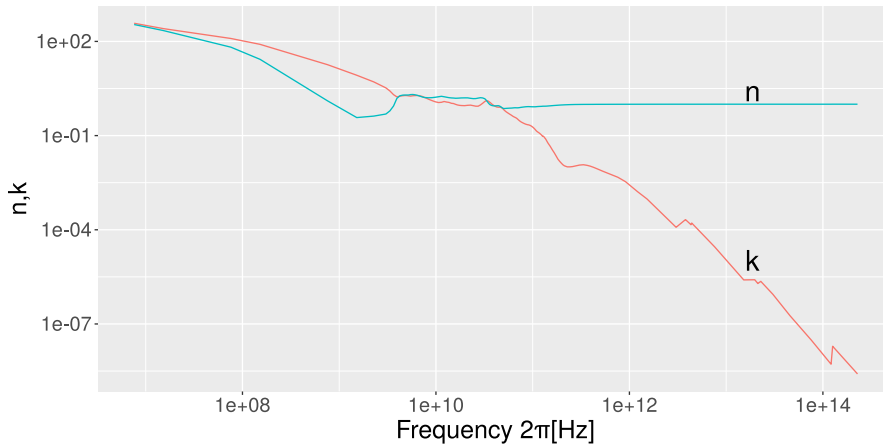$$F_C(\text{Drude}) = \frac{\zeta(3)}{8} \frac{R k_b T}{d^2} \tag{3.110}$$

Figure 3.6: The refractive index n and its imaginary part k the extinction index of gold for different angular frequencies [81].

Bezerra et al. [83] argued, that the Drude model contradicts Nernst's heat theorem, and has to be corrected. They came up with the plasma model, where the transversal electrical mode at zero frequency is not added to the calculation:

$$\epsilon(\omega) = 1 - \frac{\omega_p^2}{\omega} \tag{3.111}$$

This leads to a force that is twice as high as in the Drude model:

$$F_C(\text{Plasma}) = \frac{\zeta(3)}{4} \frac{Rk_bT}{d^2} \tag{3.112}$$

Brevik et al. [84] argued, that the conclusion from Bezerra et al. was wrong, and that the Drude model does not contradict Nernst's heat theorem. The Casimir effect was first measured in 1958 by Marcus Sparnaay in Eindhoven [58]. More precise measurements were conducted in 1997 by Steve Lamoreaux [59]. He changed the geometric setup from parallel plates to a sphere and a plate. A sphere has the advantage that its orientation is unimportant, while parallel plates need to be adjusted very precisely. The measurement of Sushkov in 2011 was in favor of the Drude model [82], while the experiment by Chang in 2012 favored the Plasma model [85].

3.3 Van der Waals Interaction

Between neutral atoms exists no Coulomb interaction. But a neutral atom or a molecule can be polarized. There are different types of polarization effects:

- Keesom interaction

- Debye force

- Londen dispersion interaction

If both molecules have a permanent electrical dipole, an electrostatic force arises. It is called *Keesom* interaction. If only one molecule has a permanent dipole and the other molecule or atom does not, the first can induce a dipole to the second. This force is called *Debye* force. The last case, where both molecules or atoms have no permanent dipole, a dipole can arise due to quantum mechanical fluctuations. This case is called *London dispersion* interaction.
All three of the above interactions follow a $\frac{1}{r^6}$ power law with different coupling strengths. They are summarized as van der Waals potentials. The potential of the van der Waals force between atoms is given by:

$$V_{\text{vdw}} = -\frac{C}{r^6} \tag{3.113}$$

where C is the constant of proportionality and r is the distance. Starting from the intermolecular forces, the force between macroscopic objects can be calculated and is done by pairwise summation of all intermolecular interactions. This was done by Hamaker [86] by assuming spherical molecules. This integration for the plate-sphere geometry was done by Czarnecki [87] and Clayfield et al. [88]. For a distance of a few nanometer, this leads to the formula [89]:

$$V_{\text{spvdw}} = -\frac{A}{6r}R \tag{3.114}$$

where A is the Hamaker constant, r is the distance between the surfaces and R is the radius of the sphere. For larger distances this would be more like:

$$V_{\text{spvdw}} = \frac{A}{6}\left(\frac{R}{r} + \frac{R}{r+2R} + \ln\frac{r}{r+2R}\right) \tag{3.115}$$

The Hamaker constant depends on the material properties. Klimchitskaya et al. [90] calculated it for gold to:

$$A_{\text{Au}} = (4.31 \pm 0.14) \times 10^{-19}\,\text{J} \tag{3.116}$$

If the distance of a pair of atoms becomes so small that the electron orbitals would penetrate Pauli's principle causes a repulsive force, which is approximated by a $\frac{1}{r^{12}}$ power law. The superposition of the attractive London potential and the repulsive force in denoted Lennard-Jones potential.

$$V(r) = \left(\frac{a}{r^{12}} - \frac{b}{r^6}\right) \tag{3.117}$$

where a and b are constants that depend on the interacting atoms or molecules. The r^{12} part describes the short range repulsive force and the r^6 part describes the stated van der Waals forces [91]. The typical Lennard-Jones-Potential is shown in Fig. 3.7.
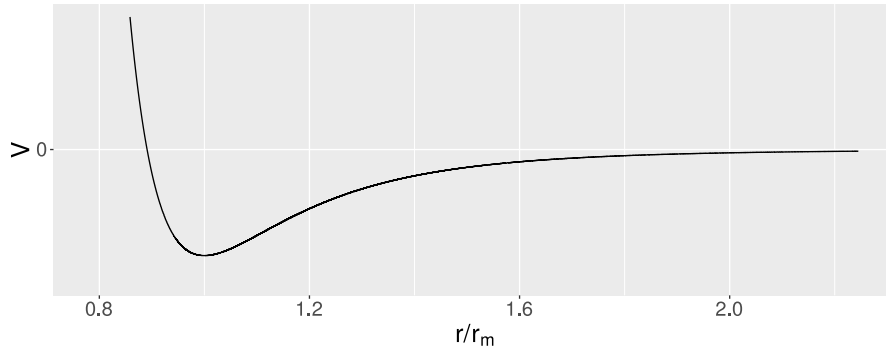
Figure 3.7: The typical form of the Lennard-Jones-Potential. The minimum of the potential, where the attractive force changes to a repulsive force r_m is often called radius of the molecule or atom. It is defined as $r_m = \left(\frac{2a}{b}\right)^{1/6}$.

3.4 Electrostatic Interaction

To calculate the electrostatic force between a sphere and a plate, we need the capacity of a capacitor built from a plate and a sphere. In Boyer et al. [92] the capacity for this is:

$$C_{sp} = 4\pi\epsilon \sinh\left(\alpha\right) \sum_{n=1}^{+\infty} 1/\sinh n\alpha \tag{3.118}$$

with $\cosh\left(\alpha\right) = 1 + d/R$, where d is the distance between the surfaces, R is the radius of the sphere and ϵ is the permittivity of the insulating interfacial layer. They calculate an approximation to:

$$C_{sp}(d) = 2\pi\epsilon R \left(\ln\left(\frac{R}{d}\right) + \ln(2) + \frac{23}{20} + \frac{\theta}{63}\right) \tag{3.119}$$

where $\theta \in [0, 1]$. The stored energy of a capacitor is:

$$W = \frac{1}{2}C \cdot V^2 \tag{3.120}$$

The force is the derivative of the stored energy with respect to the distance:

$$
\begin{aligned}
F_V(d) = \frac{\mathrm{d}W}{\mathrm{d}d} &= \pi\epsilon R V^2 \frac{\mathrm{d}}{\mathrm{d}d}\ln\left(\frac{R}{d}\right) & (3.121)\\
&= \pi\epsilon R V^2 \left(-\frac{d}{R}\cdot\frac{R}{d^2}\right) & (3.122)\\
&= \pi\epsilon R V^2 \frac{1}{d} & (3.123)
\end{aligned}
$$

With a superposition of an applied voltage and the contact potential, this is:

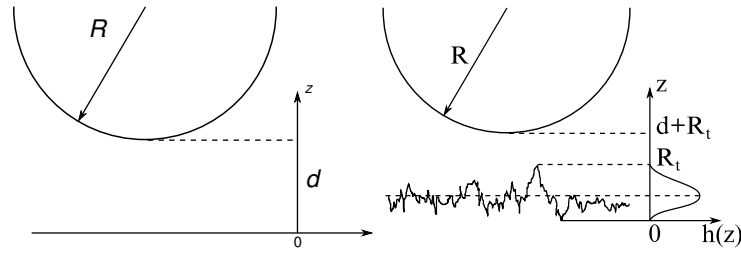$$F_V(d) = \pi\epsilon_0 R \frac{\left(V - V_m\right)^2}{d} \tag{3.124}$$

Figure 3.8: The left shows a sphere capacitor without roughness and the right shows the sphere capacitor with roughness.

3.4.1 Electrostatic force with surface roughness

For a sphere-plate capacitor with non-ideal surface topographies Boyer et al. have developed a model [92] including rough surfaces. With $h(z)$ for the height distribution (in roughness metrology often refered to as amplitude distribution) Boyer et al. state:

$$C_{\mathrm{rgh}} \approx_{d/R \ll 1} = 2\pi\epsilon R \cdot \int\limits_{0}^{R_t} h(z) \ln\left(\frac{R}{d+R_t-z}\right) \mathrm{d}z + 1.843 + \frac{\theta}{63} \qquad (3.125)$$

with $\theta \in [0,1]$. $h(z)$ is a density function of how frequent specific heights are in the surface profile, it is given by the superposition of the roughness profiles of both surfaces. It is defined that it fulfills the condition:

$$\int\limits_{0}^{R_t} h(z)\mathrm{d}z = 1 \qquad (3.126)$$

R_t is the peak-to-peak roughness. This means the roughness profile is shifted with respect to the zero line by $z = z - \min(z)$. The derivative from the capacitance in means of the distance leads to:

$$\left(\frac{\partial C_{\mathrm{rgh}}}{\partial d}\right) \overset{d/R \ll 1}{\approx} -2\pi R\epsilon \int\limits_{0}^{R_t} \frac{h(z)}{d+p-z}\mathrm{d}z \qquad (3.127)$$

And for a roughness much smaller than the distance ($d \gg R_t$):

$$\left(\frac{\partial C_{\mathrm{rgh}}}{\partial d}\right) \overset{d/R \ll 1}{\approx} -2\pi R\epsilon \frac{1}{d+R_t-R_a} \qquad (3.128)$$

where R_a is the arithmetic average of the roughness profile. This leads to a force of:

$$F_{\mathrm{rgh}}(d) \approx -\pi R V^2 \epsilon \frac{1}{d+R_t-R_a} \qquad (3.129)$$

For large distances ($d \gg R_t$) this means, that roughness changes the distance between sphere and plate only of about the mean roughness. At small distances ($R_t < d$ or $R_t \approx d$), the roughness profile has a larger effect.

Therefore the roughness profile of the sphere and the plate has to be measured and to be included in the detailed data analysis.

$$F_{\mathrm{rgh}}(d) \approx -\pi R V^2 \epsilon \int_0^{R_t} \frac{h(z)}{d+p-z}\mathrm{d}z \qquad (3.130)$$

3.4.2 The Patch Effect

The work function indicates how much energy is needed to remove an electron from the material. The work function depends mostly on the bulk material, but also on its underlying crystalline structure. Different alignments of the crystalline structure and defects change the work function, and a change of the work function leads to a different electrostatic field. The crystalline structure of gold appears to be like a patchwork, and the variation of the work function over the surface is named after that patch effect. The patch effect leads to a root mean square voltage V_{rms} which acts as an electrostatic force:

$$F_{\mathrm{rms}}(d) = \pi \epsilon R \frac{V_{\mathrm{rms}}^2}{d} \qquad (3.131)$$

ϵ is the permittivity function, V is the user controlled voltage, V_m is the offset voltage between the surfaces, V_{rms} is the voltage that comes from the patch effect [93][94].

3.5 Other Influences

3.5.1 Gas Pressure on Surfaces

Every gas particle, atoms as well as molecules, that collides with the force sensor give an impulse to the force sensor. As long as the molecules do not have preferred directions from where they hit the sensor, this does not lead to a force, but is a noise source known as Brownian noise. But there are processes where the impulse directions are no longer purely stochastic such that they cancel out, but rather have preferred directions summing up to a resultant force. One process comes into play, if for example parallel plates have different temperatures. This is used in a so called Knudsen pressure gauge, which can be used to measure the absolute pressure in vacuum. Knudsen [95] states as equation for the force between parallel plates:

$$F_{kn} = \sqrt{\frac{T_1}{T_2} - 1} \frac{pA}{2} \qquad (3.132)$$

where T_1 and T_2 are the temperatures of the plates, p is the vacuum pressure and A is the area of the plates. For the Knudsen force for a sphere with radius R before a plate with a distance d follows using the proximity force theorem:

$$F_{kn}(R) = 2\pi R \int F_{kn}\mathrm{d}d = \pi R p d \sqrt{\frac{T_1}{T_2} - 1} \qquad (3.133)$$

3.5.2 Water on Surfaces

One of the main parasitic forces in atomic force microscopy (AFM) are capillary forces due to a water film on the surfaces. To reduce this effect,

AFMs are placed in a vacuum, but not the complete water film vanishes [96] when pumping down. The force between a plate and a sphere due to a water capillary was measured by Mason et al. [97]. Based on that, Willett et al. [98] have built a model for non-equal spheres. A plate is a sphere with a radius $\lim r \to \infty$. The capillary force can only exist at a distance smaller than the cubic root of the water volume:

$$d_{\max} = \sqrt[3]{V} \tag{3.134}$$

Assuming there is a monolayer of water molecules on each surface with a thickness of $0.3\,\text{nm}$, and all the molecules form a circle of radius $r = 100\,\text{nm}$, the maximum distance $d_{\max}$ would be $27\,\text{nm}$. This means that above that distance the water on the surface does not interfere with the measurements.

3.5.3 Temperature-dependence of Young's modulus

The elastic constants of every material are temperature dependent. The temperature dependence of fused silica was measured by McSkimin [99] and Fig. 3.9 shows Young's modulus E of fused silica.
For example, the temperature dependence could lead to a frequency shift due to temperature changes. The following shows an example calculation for that. The stiffness of a cantilevered beam of a rectangular cross section is given by:

$$k = \frac{Ewt^3}{4L^3} \tag{3.135}$$

where w is the width, t is the thickness and L is the length of the cantilever. To compare different temperatures only as a function of Young's modulus, we set $\frac{wt^3}{4L^3} = 10^{-7}\,\text{m}$. The frequency for a cantilever with this k is:

$$f = 2\pi\omega = 2\pi\sqrt{k/\hat{m}} \tag{3.136}$$

where $\hat{m}$ is the effective mass, in this example is $\hat{m} = 10^{-6}\,\text{kg}$.

$$
\begin{aligned}
f(20\,^\circ\text{C}) &= 13591.86\,\text{Hz} & (3.137)\\
f(21\,^\circ\text{C}) &= 13593.13\,\text{Hz} & (3.138)\\
\Rightarrow \frac{\Delta f}{\Delta T} &= \frac{f(20\,^\circ\text{C}) - f(21\,^\circ\text{C})}{1\,\text{K}} \approx 1.3\,\text{Hz}\,\text{K}^{-1} & (3.139)
\end{aligned}
$$

3.5.4 Light pressure

When light is reflected on a mirror, the momentum of the light is transferred. The momentum of a photon is [100]:

$$|\vec{p}| = \frac{\hbar\omega}{c} \tag{3.140}$$

On a mirror, the transferred momentum is twice of that, because after the elastic collision, the photon has the same momentum as before, but in the opposite direction.
The force on a mirror coming from that momentum for N photons is:

$$F = 2\frac{\text{d}|\vec{p}|}{\text{d}t} = 2\frac{\hbar\omega}{c}\frac{\text{d}N}{\text{d}t} \tag{3.141}$$
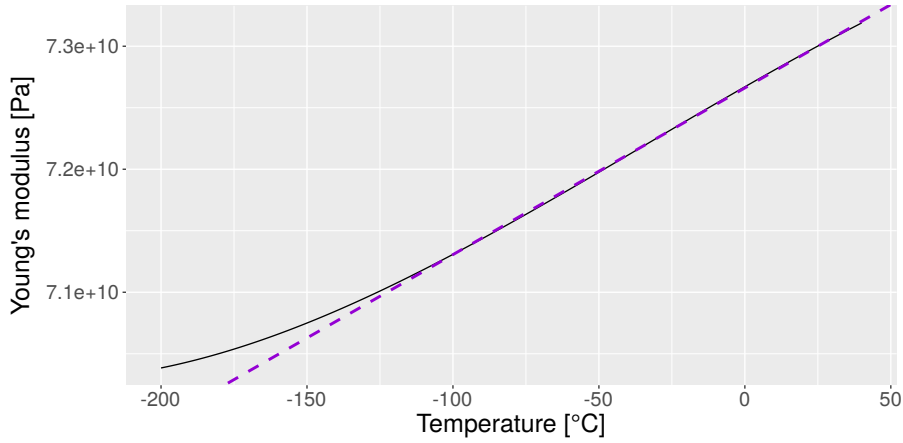
Figure 3.9: The solid line is Young's modulus of fused silica measured by Mc-Skimin [99], the dashed line is the linear fit at 20 °C with a slope of 13.5 MPa/K.

The power of a monochromatic light beam is:

$$P = \hbar\omega \frac{\mathrm{d}N}{\mathrm{d}t} \tag{3.142}$$

Combining Eq. (3.142) and Eq. (3.141), the force due to light pressure is:

$$F = 2\frac{P}{c} \tag{3.143}$$

3.5.4.1   Light Pressure in a Fabry-Pérot

Light pressure in a Fabry-Pérot cavity is more complicated, since each photon is reflected multiple times. The finesse $\mathcal{F}$ is the average number of round-trips of a photon [101] and it is given by:

$$n = \frac{\mathcal{F}}{\pi} \tag{3.144}$$

Therefore, the force in a Fabry-Pérot where the incoming light has the power P is:

$$F = 2\frac{P\mathcal{F}}{c\pi} \tag{3.145}$$

Loss in a Fabry-Pérot cavity can be described by [102]:

$$\hat{R} = R\mathrm{e}^{-\alpha L} \tag{3.146}$$

where R is the reflectivity of the mirrors, L is the length of the cavity and α is the attenuation coefficient.
The finesse as function of the reflectivity by:

$$\mathcal{F} = \frac{\pi\sqrt{R}}{1 - R} \tag{3.147}$$

Eq. (3.145) with the attenuated reflectivity results in a length dependent force:

$$F = 2\frac{P}{c} \cdot \frac{\sqrt{R}\mathrm{e}^{-\alpha L}}{(1 - R\mathrm{e}^{-\alpha L})} \tag{3.148}$$

For example, with a low finesse cavity with $R = 0.04$, $L = 25\,\mu\mathrm{m}$, $P = 1\,\mathrm{mW}$ and the attenuation coefficient according to Regener et al. [102] of $\alpha = 10.6\,\mathrm{m}^{-1}$:

$$F = 1.3897\mathrm{pN} \tag{3.149}$$

If for example one mirror oscillates with an amplitude of $1\,\mathrm{nm}$, the force changes by around $8 \cdot 10^{-21}\,\mathrm{N}$. This means that this effect does not play a role for the experiments in this thesis.
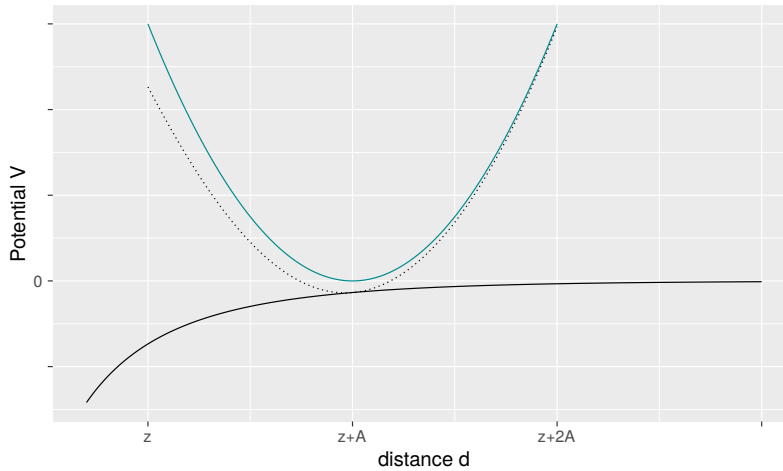
Figure 3.10: The potential of an arbitrary field (solid black line) distorts the potential of a harmonic oscillator (solid blue line) over one oscillation. The dotted line is the combined potential over one oscillation. A is the amplitude, z the nearest distance of the oscillator to the source of the distortion potential.

3.6 Force Measurement

For force measurements exist a lot of different kinds of measurement principles, such as strain gauges, piezoelectricity and electromagnetic compensation balances. The most obvious method is measuring the force using Hooke's law:

$$F(x) = kx \tag{3.150}$$

where k is the Spring constant, x is the extension of the spring and F is the force. This was also the method used at the beginning of atomic force microscopes. For AFMs exists another technique called *frequency modulation force spectroscopy*. With this method, measuring the force is converted to measuring a frequency.

A cantilever has a spring constant k_1 and an effective mass m that determine its eigenfrequency to:

$$\omega_0 = \sqrt{\frac{k_1}{m}} \tag{3.151}$$

The overall potential of the external distance depending force field in the moving direction of the oscillation and the spring potential adds up to a potential seen is Fig. 3.10. This distance dependent force field acts like a spring that is parallel to the cantilever spring as seen in Fig. 3.11. In general the spring *constant* is distance dependent and is better called *spring function*:

$$k_2(d) \tag{3.152}$$

In case of a linear force field $F(x) = k_2 x$, the spring constant is really constant. For two parallel springs, the effective spring constant is the sum of both spring constants:

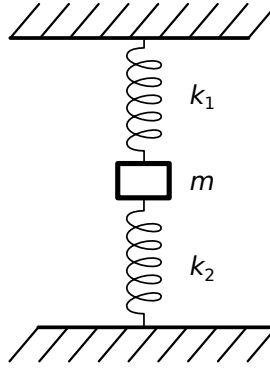$$k_{\text{eff}} = k_1 + k_2 \tag{3.153}$$

Figure 3.11: The cantilever in a force field can be seen as a mass with parallel springs. The stiffness of the cantilever itself is k_1, and the force field acts like a parallel spring with the distance dependent spring function $k_2(d)$.

This leads to a new eigenfrequency:

$$\Delta\omega + \omega_0 = \sqrt{\frac{k_1 + k_2}{m}} \tag{3.154}$$

Or written as frequency shift:

$$\frac{\Delta\omega}{\omega_0} = 1 - \sqrt{1 + \frac{k_2}{k_1}} \tag{3.155}$$

If $|k_2| \ll |k_1|$, a Taylor series can be used to simplify the square root[7]:

$$\frac{\Delta\omega}{\omega_0} = \frac{1}{2}\frac{k_2}{k_1} + h.c. \tag{3.156}$$

According to Dürig [103], the frequency shift of any kind of interaction potential can be derived using a principle of least action. He gives as interaction integral:

$$S = \int_0^T \frac{1}{2}\psi^2(t) - \frac{1}{2}\frac{\mathrm{d}\psi(t)}{\mathrm{d}t} + \frac{\omega_0}{k_1}V(\psi_0 + \psi(t))\mathrm{d}t \tag{3.157}$$

where $\psi(t)$ is the oscillatory motion, ψ_0 is an offset where the spring is relative to the interaction force source and $V()$ is the potential of the interaction force. The variation of δS has to vanish:

$$\delta S = \int_0^T \left(\omega_0^2\psi(t) + \frac{\mathrm{d}^2\psi(t)}{\mathrm{d}t^2} + \frac{\omega_0^2}{k_1}F\left(\psi_0 + \psi(t)\right)\right) \times \delta\psi(t)\mathrm{d}t \equiv 0 \tag{3.158}$$

The function $\psi(t)$ can be assumed as Fourier series:

$$\psi(t) = \sum_{n=1}^\infty a_n \cos(n\omega t) \tag{3.159}$$

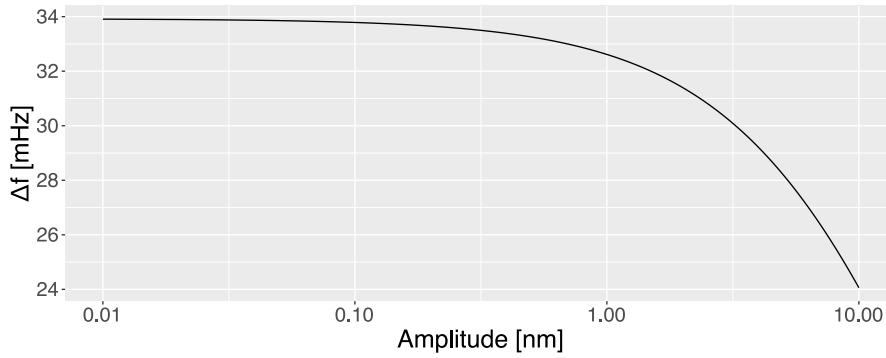[7] $\sqrt{1+x} = 1 + \frac{1}{2}x + \frac{1}{8}x^2 + h.c.$

Figure 3.12: Amplitude dependence of the frequency shift for an electrostatic potential. It was calculated for a voltage of $0.1\,\mathrm{V}$ at a distance of $50\,\mathrm{nm}$ for characteristics of the force sensor described in chapter 4.1.1.

with the corresponding variation:

$$\delta\psi(t) = \sum_{n=1}^{\infty} \delta a_n \cos(n\omega t) \tag{3.160}$$

Inserting in Eq. (3.158) gives:

$$\delta S = \frac{\pi}{\omega} \sum_{n=1}^{\infty} a_n \left(\omega_0^2 - n^2\omega\right) \delta a_n + \delta S_{\mathrm{int}} \tag{3.161}$$

with

$$\delta S_{\mathrm{int}} = \frac{\omega_r e s^2}{k_1} \sum_{n=1}^{\infty} \delta a_n \int_0^T F\left(\psi_0 + \sum_{n=1}^{\infty} a_n \cos(n\omega t)\right) \times \cos(n\omega t)\mathrm{d}t \tag{3.162}$$

restricting the fourier transform to the lowest harmonic, which means $a_n = 0 \forall n \geq 2$ gives:

$$\omega = \omega_0 \sqrt{1 + \frac{2}{\pi a_1 k_1} \int_{-1}^{1} F\left(d + a_1(1 + x)\right) \frac{x}{\sqrt{1 - x^2}}\mathrm{d}x} \tag{3.163}$$

where the substitution $\cos(\omega t) = x$ was used and d is the smallest distance between the AFM tip and the surface.
The linear case can be seen as the derivative of the distance dependent force. Putting Eq. (3.163) into Eq. (3.156) gives[8]:

$$\frac{\Delta\omega}{\omega_0} = -\frac{1}{\pi a k} \int_{-1}^{1} F(z + a(1 + u)) \frac{u}{\sqrt{1 - u^2}}\mathrm{d}u \tag{3.164}$$

It follows that a lower amplitude a is better for measuring the frequency shift at a given distance z. Fig. 3.12 shows the amplitude dependence of the

---

[8]See also [104] and [105] for the derivation.

frequency shift for an electrostatic potential at a $50\,\mathrm{nm}$ distance for conditions described in chapter 4.1.1.

In Sader et al. [105] this formula is inverted for the constant amplitude case, to get the force out of the frequency shift:

$$F(z) = 2k \int\limits_{z}^{\infty} \left(1 + \frac{a^{1/2}}{8\sqrt{\pi(t-z)}} \frac{\Delta\omega(t)}{\omega_0} \right) - \frac{a^{3/2}}{\sqrt{2(t-z)}} \frac{\mathrm{d}\Delta\omega(t)}{\omega_0 \mathrm{d}t} \mathrm{d}t \qquad (3.165)$$

This equation should be useful, as long as the forces and therefore the frequency shift diminishes with larger z.

3.7 Resonance Amplitude of a Mechanical Oscillator

The differential equation of a force mechanical oscillator is:

$$\ddot{x} + 2\gamma\dot{x} + \omega_0^2 x = \frac{F_0}{m} \cdot \cos\omega t \qquad (3.166)$$

ω is the driving frequency, F_0 is the amplitude of the driving force, m is the effective mass off the osscilator, γ is the dampening and ω_0 is the eigenfrequency of the oscillator as was seen in Eq. (3.151). The amplitude of the stationary state of the forced oscillator is [106, Eq. 11.26]:

$$A(\omega) = \frac{F_0/m}{\sqrt{\left(\omega_0^2 - \omega^2\right)^2 + \left(2\gamma\omega\right)^2}} \qquad (3.167)$$

where $A(\omega)$ is the amplitude.

The resonance frequency ω_R is:

$$\omega_\mathrm{R} = \sqrt{\omega_0^2 - 2\gamma^2} \qquad (3.168)$$

The effective mass m of a more complex oscillator is not easily accessible, so it is replaced with the stiffness k and the eigenfrequency:

$$m = \frac{k}{\omega_0} \qquad (3.169)$$

By putting equations Eq. (3.169) and Eq. (3.168) into Eq. (3.167) it leads to:

$$A(\omega_\mathrm{R}) = \frac{F_0\omega_0^2/k}{\sqrt{\underbrace{\left(\omega_0^2 - \left(\omega_0^2 - 2\gamma^2\right)\right)^2}_{4\gamma^4} + \underbrace{4\gamma^2\left(\omega_0^2 - 2\gamma^2\right)}_{4\gamma^2\omega_0^2 - 8\gamma^4}}} \qquad (3.170)$$

$$A(\omega_\mathrm{R}) = \frac{F_0\omega_0^2/k}{\sqrt{4\gamma^2\omega_0^2 - 4\gamma^4}} \qquad (3.171)$$

Based on the relation of the quality factor Q and the dampening γ from

Siebert [107], $Q = \frac{\omega_0}{2\gamma}$, follows:

$$\overset{\gamma=\frac{\omega_0}{2Q}}{\Longrightarrow} A\left(\omega_{\mathrm{R}}\right) = \frac{F_0 \omega_0^2 / k}{\sqrt{4\omega_0^2 \frac{\omega_0^2}{4Q^2} - 4\frac{\omega_0^4}{16Q^4}}} \tag{3.172}$$

$$A\left(\omega_{\mathrm{R}}\right) = \frac{F_0 \omega_0^2 / k}{\sqrt{\frac{\omega_0^4}{Q^2} - \frac{\omega_0^4}{4Q^4}}} \tag{3.173}$$

$$A\left(\omega_{\mathrm{R}}\right) = \frac{F_0 \omega_0^2 / k}{\omega_0^2 \sqrt{\frac{1}{Q^2} - \frac{1}{4Q^4}}} \tag{3.174}$$

$$A\left(\omega_{\mathrm{R}}\right) = \frac{F_0 / k}{\sqrt{\frac{1}{Q^2}\left(1 - \frac{1}{4Q^2}\right)}} \tag{3.175}$$

$$A\left(\omega_{\mathrm{R}}\right) = Q\frac{F_0 / k}{\sqrt{1 - \frac{1}{4Q^2}}} \tag{3.176}$$

With the definitions $D = \frac{1}{2Q}$ as dampening coefficient[9] and $A_{\mathrm{stat}} = \frac{F_0}{k}$ as the displacement with a static force F_0, the formula can be rewritten so that the resonance amplitude depends on the static *amplitude* A_{stat} and the dampening D:

$$A_{\mathrm{res}} = \frac{A_{stat}}{2D\sqrt{1 - D^2}} \tag{3.177}$$

After removing the driving force, or with a different kind of excitation, the oscillation decays:

$$x(t) = A\mathrm{e}^{-\gamma t} \cos\left(\omega_{\mathrm{d}} t + \varphi\right) = A\mathrm{e}^{-\omega_0 t/2Q} \cos\left(\omega_{\mathrm{d}} t + \varphi\right) \tag{3.178}$$

with $\omega_{\mathrm{d}} = \sqrt{\omega_0^2 - \gamma^2}$ [106]. This can be used to measure the quality factor.

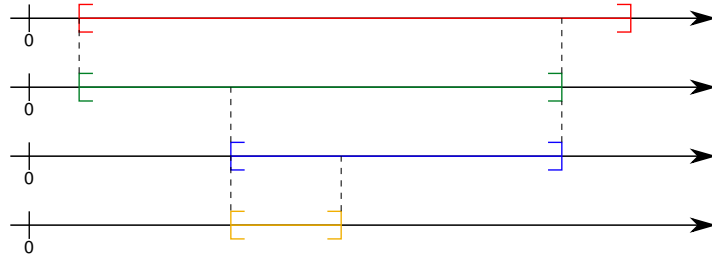[9]Note that D is a dampening per oscillation, it can also be written as $D = \frac{\gamma}{\omega_0}$.

Figure 3.13: Nested intervals [108]. Starting from the top interval, in each interaction the interval is refined until a specific lower interval length is reached.

3.8 Data Analysis

3.8.1 Nested Intervals to Calculate Yukawa Parameters for a Given Frequency

While Eq. (3.22) can easily be used to calculate α for a given force and a given λ, this is not possible if only the frequency shift from Eq. (3.164) is known. To calculate α for a given frequency shift $\Delta\omega$ and a given length scale λ a numeric method is needed. For this, a nested interval approach is used. Fig. 3.13 shows the nested intervals method graphically. Usually the nested intervals method calculates the mean between the upper boundary and the lower boundary and calculates the function value at that point and compares it to the reference value. One example where this method is used is finding the square root of a number. As the Yukawa plot is logarithmic, a nested interval method cannot use the upper and lower boundaries itself, because it would not finish the algorithm in a reasonable number of iterations. Instead the logarithm of the boundaries is used for the algorithm. Algorithm listing 1 shows the algorithm.

Algorithm 1 logarithmic nested intervals

 1: **procedure** Nested Intervals
 2:     $lower \leftarrow log10(lower\ boundary)$
 3:     $upper \leftarrow log10(upper\ boundary)$
 4:     $tol \leftarrow minimum\ goal$
 5:     $resultLower \leftarrow fn(10^{lower})$
 6:     $resultUpper \leftarrow fn(10^{upper})$
 7:     $loop$:
 8:     **while** $(upper - lower) > tol$ **do**
 9:         $mid \leftarrow (upper + lower)/2$
10:         $resultMid \leftarrow fn(10^{mid})$
11:         **if** $resultMid > 0$ **then**
12:             $upper \leftarrow mid$
13:             $resultUpper \leftarrow resultMid$
14:         **if** $resultMid < 0$ **then**
15:             $lower \leftarrow mid$
16:             $resultLower \leftarrow resultMid$
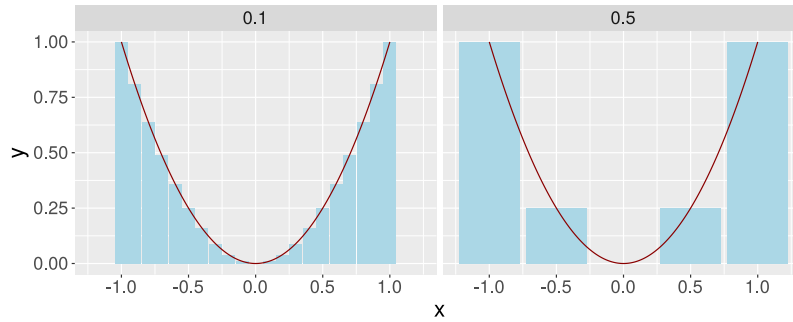   **return** mid
---

Figure 3.14: Riemann sum approximation of x^2. The right shows a coarse approximation with five nodes and the left is a finer approximation with 21 nodes.

3.8.2 Numerical Integration

As Eq. (3.164) is not analytically solvable for most of the interaction forces, numeric integration is used to calculate the frequency shift for a given force. One definition for an integral is the Riemann integral. The Riemann integral defines an integral on the interval $[a, b] \in \mathbb{R}$. The interval is parted into subdivisions like:

$$a = x_0 < x_1 < x_2 < \cdots < x_n = b \tag{3.179}$$

Fig. 3.14 shows an example of the Riemann sum approximation. Using these subdivisions, the Riemann sum is defined as[10]:

$$\sum_{i=0}^{n-1} f(x_i) \cdot (x_{i+1} - x_i) \tag{3.180}$$

The smaller the subdivisions get, the better is the estimate for the integral:

$$\lim_{n \to \infty} \sum_{i=0}^{n-1} f(x_i) \cdot (x_{i+1} - x_i) = \int_a^b f(x) \mathrm{d}x \tag{3.181}$$

From the Riemann integral follows the simplest way to numerically integrate any function $f(x)$, just define the subdivisions and calculate the Riemann sum.

Unfortunately the Riemann sum needs a lot of subdivisions to calculate the integral to an acceptable accuracy, so a number of other approaches are used to increase calculation speed.

3.8.2.1 Gaussian Quadrature

Gaussian quadrature is one of those other methods. It is best for functions of the form:

$$\int_{-1}^{1} f(x) \cdot q(x) \mathrm{d}x \tag{3.182}$$

---

[10]Most of the times, not $f(x_i)$ is used, but instead $f(t_i)$ where $t_i \in [x_i, x_{i+x}]$. But for numeric integration the abstract t_i is not useful, so we use a definition with a defined value.

where a polynomial can approximate $f(x)$ and $q(x)$ is a weight function. The integration transforms into the sum over n chuncks with weights w_k and the integration error $E_n(f)$

$$\int_{-1}^{1} f(x) \cdot q(x) \mathrm{d}x = \sum_{k=1}^{n} w_k f(x_k) + E_n(f) \tag{3.183}$$

The most common Gaussian quadrature is the GaussLegendre quadrature [75, 7.3.3.3]. In this case is $q(x) = 1$. It is based on the Legendre polynomials $P_n(x)$. The n-th polynomial has to be normalized to one: $P_n(1) = 1$. Then x_k is the k-th root of P_n. The weights are:

$$w_k = \frac{2}{\left(1 - x_k^2\right)\left(P_n'(x_k)\right)^2} \tag{3.184}$$

The weights w_k and the nodes x_k are tabulated in Zeidler [75, 7.3.3.3]. An adaptive version of this is the Gauss-Kronrod quadrature where to the n nodes of the Gauss-Legendre quadrature additional $n+1$ Kronrod nodes are used. This method is based on the Stieltjes polynomials, and has the great advantage, that refining the result uses all the results calculated in the first iteration. The Gauss-Kronrod quadrature method is the basis of the Quadpack fortran library [109] [110] which is the basis of most numerical integration functions.

3.8.2.2   ChebyshevGauss Quadrature

Chebyshev-Gauss quadrature [75, 7.3.3.3] is another version of the Gauss quadrature rule. In this case, the weight function is $q(x) = \frac{1}{\sqrt{1-x^2}}$. This means, this method is useful for every integral of the form:

$$\int_{-1}^{1} f(x) \frac{1}{\sqrt{1-x^2}} \mathrm{d}x \tag{3.185}$$

The nodes are:
$$x_k = \cos\left((2k-1)\pi/2n\right) \tag{3.186}$$

and the weights are:
$$w_k = \frac{\pi}{n} \tag{3.187}$$

The quadrature error is:

$$E_n(f) = \frac{2\pi}{2^{2n}(2n)!} \frac{\mathrm{d}^{2n} f}{\mathrm{d}x^{2n}}(\xi) \tag{3.188}$$

with $\xi \in (-1, 1)$. This method of numerical integration obviously fits the needs of Eq. (3.164). This leads to the integration formula:

$$\int_{-1}^{1} F\left(z + a(1+u)\right) u \frac{1}{\sqrt{1-u^2}} \mathrm{d}u =$$

$$\sum_{k=1}^{n} \frac{\pi}{n} F\left(z + a\left(1 + \cos\left((2k-1)\frac{\pi}{2n}\right)\right)\right) \cos\left((2k-1)\frac{\pi}{2n}\right) + E_n(f) \tag{3.189}$$

while the function varies, weight w_k and the nodes x_k can be preevaluated, which decreases integration time. For the electrostatic equation (3.124), the Chebyshev-Gauss quadrature has a relative error of $3 \cdot 10^{-13}$ with only 3 nodes.

3.8.3 Mathematical Optimization

Mathematical optimization has the goal to find the best result for a mathematical function. One major example is fitting the parameters of a function to measured data.

3.8.3.1 Levenberg-Marquardt Algorithm

The Levenberg-Marquardt algorithm is a non-linear least squares method for curve fitting. It is based on the Gauss-Newton algorithm and adds some gradient descent method to it. This means, it is only feasable to find local minima and not necessarily a global minimum [111] [112]. Non-linear least squares method means, that it minimizes the following function:

$$g(p) = \sum_{j=1}^{m} r_j^2(p) \tag{3.190}$$

p is the vector of fitting parameters. r_j are the residuals of a function. For example is $F(x)$ a number of measured values at the points x and $f(x, p)$ is the function that should be fitted to the measured values. Then the residuals are:

$$r_j = F(x_j) - f(x_j, p) \tag{3.191}$$

And r_j^2 is the square in the name for which the sum should be minimized. The Jacobian J of the residuals is:

$$J(p) = \frac{\partial r_j}{\partial p_i} \tag{3.192}$$

with $1 \leq j \leq m$ and $1 \leq i \leq n$, and n is the total number of fitting parameters. At the minimum, the gradient of $g(p)$ is zero and the curvature or second derivative of $g(p)$ is negative. Both are calculated as:

$$\nabla g(p) \quad = \quad \sum_{j=1}^{m} r_j(p) \nabla r_j(p) = J(p)^T r(p) \tag{3.193}$$

$$\nabla^2 g(p) = H \quad = \quad J(p)^T J(p) + \sum_{j=1}^{m} r_j(p) \nabla^2 r_j(p) \tag{3.194}$$

With the assumption that the residuals are nearly linear the Hessian H is reduced to

$$\nabla^2 g(p) = H = J(p)^T J(p) \tag{3.195}$$

The Levenberg-Marquardt algorithm is a stepwise optimiziation method. This means that a new $\hat{p}$ that should be closer to the solution is calculated from the current p. This is done with:

$$\hat{p} = p - (H + \lambda \mathrm{diag}(H))^{-1} \nabla g(p) \tag{3.196}$$

The diagonal of the Hessian was introduced by Marquardt to increase the step size for directions with a small curvature and to reduce the step size in case of a large curvature. A step is accepted if the error smaller than the error before the step. Then λ is decreased by a factor of for example 10. If the step was not accepted, λ gets increased, also for example by a factor of 10. Further details about the algorithm can be found in Madsen et al. [113].

3.8.3.2 Differential Evolution

The Levenberg-Marquardt algorithm can only find a local minimum. This makes the algorithm not useful in cases with a lot of local minima, such as fitting sinusoidal functions. One method to find global minima is called Differential Evolution [114] (DE). DE is inspired by the concept of evolution in biology. This means a population P of possible parameters p is defined. For each member of the population, a so called fitness function is calculated. A possible fitness function could be a reciprocal Eq. (3.190). The best members of the population are the basis for the next generation. Creating members of the population of the new generation is done by mutation. Population P_i means the population of the i-th generation. $p_{i,1}$ is the first member of that population. The mutant v_i is calculated using three random members of the population:

$$v_i = p_{i,1} + \lambda \left(p_{i,2} - p_{i,3} \right) \tag{3.197}$$

λ is a scaling parameter and should be less than 1. The new generation P_{i+1} contains the best members of P_i and a certain number of mutants v_i. This is done until an arbitrary number of iterations is performed or the error is smaller than a threshold. A good introduction to using differential evolution is Ardia et al. [115]. A disadvantage of DE is, that the best member of the last generation is slightly away from the correct solution. In this case the Levenberg-Marquardt algorihm is useful as second step to get a more exact result.

3.8.3.3 Uncertainties of Fit Parameters

A least squares fit optimizes the parameters of a model. But in general it does not say something about the uncertainties of the fit parameters.

Gaussian Distributed Residuals allow calculation of the uncertainties of the fit parameters based on the Hessian matrix, especially when using the Levenberg-Marquardt or related methods. The *curvature matrix A* is defined as one-half of the Hessian matrix [116]:

$$A = \frac{1}{2} H \tag{3.198}$$

This means the components are defined as:

$$A_{jk} = \frac{1}{2} \frac{\partial g^2}{\partial p_j \partial p_k} \tag{3.199}$$

The inverse of the curvature matrix is the covariance matrix C:

$$C = A^{-1} \tag{3.200}$$

The uncertainty α_j of parameter p_j is [117]:

$$\alpha_j = \sqrt{C_{jj}} \tag{3.201}$$

In case of uncorrelated parameters p_j, all non-diagonal elements of the curvature matrix are zero. This leads to the easy way of inverting the matrix and the uncertainty gets:

$$\alpha_j = \sqrt{C_{jj}} = \sqrt{A_{jj}^{-1}} \tag{3.202}$$

But for correlated parameters this method does not apply and the matrix A has to be inverted.

Non-gaussian distributed residuals do not allow to use the Hessian matrix to calculate the uncertainty. And for the *differential evolution* method, the Hessian is not calculated. To calculate uncertainties from measurements based on any distribution, the *bootstrap* method can be used [118]. The bootstrap method is a Monte Carlo method and it goes as following:

1. Perform random sampling with replacement on the original data set, until the new data set has the same amount of data as the original data set. But due to sampling with replacement, some data points of the original data set occur multiple times, and some data points occur not at all.

2. Perform the fit routine (or any other statistics like the mean) on the new data set.

3. Repeat the first two steps a hundred to a thousand times and store each result.

4. Use the distribution of the results to calculate the desired uncertainty, for example the 68% confidence interval for the standard error.

This method was very useful for the data analysis is chapter 5.

Chapter 4

Experimental Setup

This section is about the realization of the experiment.

4.1 Force Sensor

The heart of the experiment is the force sensor. It is based on an idea from Melcher et al. [18]. They reported a force resolution of about $14\,\text{fN}$. The measurement method used in our experiments is basically the same as in frequency modulated atomic force microscopes (FM-AFM). But instead of scanning over the x-y-plane, we used the force measurement technique to measure the z-dependence of the force.
The force sensor shown in Fig. 4.1 is based from a parallelogram flexure (G). On the test mass of the force sensor, we attached a gold-coated ruby half-sphere (F). The gold coating is used as gravitating mass of the measurement. The ruby half-sphere needs an electrical connection to a voltage source. So one leg of the parallelogram flexure is gold coated, with an intermediate layer of titanium to make the gold coating more robust. We also integrated two v-grooves (D, E) on the test mass. Two fibers are attached to the v-grooves as mirrors. One fiber (D) is gold-coated to have a high reflectivity. It is used for the optical actuation. The other fiber (E) is a mirror of the Fabry-Pérot interferometer, that is used to measure the vibration of the force sensor. Opposite to the v-grooves on the test mass are two v-grooves (A, B) on the connection plate (I) of the force sensor. They are axially aligned to the v-grooves on the test mass. Both v-grooves are used to align optical fibers — one aligns the fiber for the optical actuation, and the other is part of the Fabry-Pérot interferometer. There is also a third v-groove on the connection plate. It contains the fiber that is also used as an Fabry-Pérot interferometer to measure the distance of the force sensor to the plate. Its end is aligned with the ruby sphere, but it is about $100\,\mu\text{m}$ farther away from the measurement plate than the sphere.
The force sensor is made using fused silica by *Femtoprint*. The force sensor was placed on a cuboid glass block also made of fused silica using optical contact bonding.

4.1.1 FEM Characterization of the Force Sensor

The force sensor was characterized using FEM simulations. The force sensor has a lot of different vibration modes, at different frequencies. Fig. 4.2 *a)*
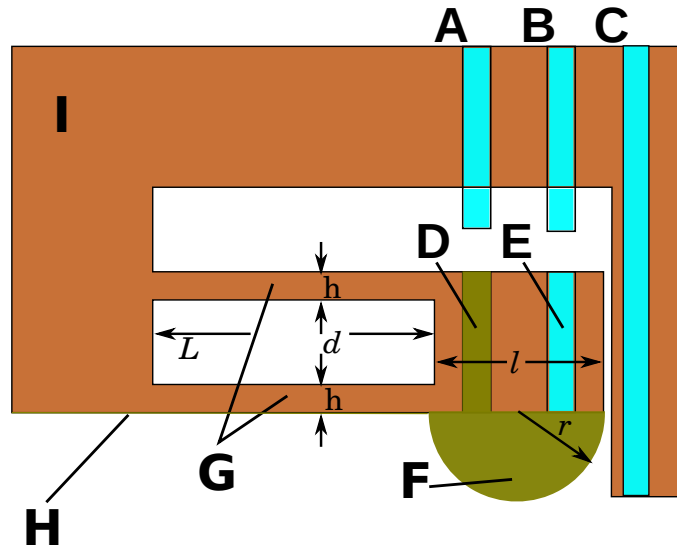
55

Figure 4.1: Complete force sensor. **A** is the optical fiber for the optical actuation, **B** is the fiber to measure the vibration, **C** is the fiber for the distance measurement, **D** is the gold coated mirror fiber for the optical actuation, **E** is the uncoated mirror fiber for the Fabry-Pérot interferometer, **F** is the gold-coated ruby half-sphere, **G** is the parallelogram flexure, **H** is the gold coating to electrically connect the half-sphere to a voltage supply, **I** is the connection plate of the force sensor.

shows the main modes of the sensor.

The geometry of the force sensor and the simulated results are listed in Table 4.1. Notably, the eigenfrequency drops by a third when the half-sphere is attached.

The temperature dependence of the eigenfrequency is also shown. The simulation is based on the temperature dependent Young's modulus. Section 3.5.3 describes how the temperature dependence of Young's modulus was obtained. Using that value in an FEM simulation gives the temperature dependence shown in Table 4.1.

All simulated properties of the force sensor were measured after the force sensor was assembled to obtain a more precise value for them. The simulated values were necessary to design the experiment around them.
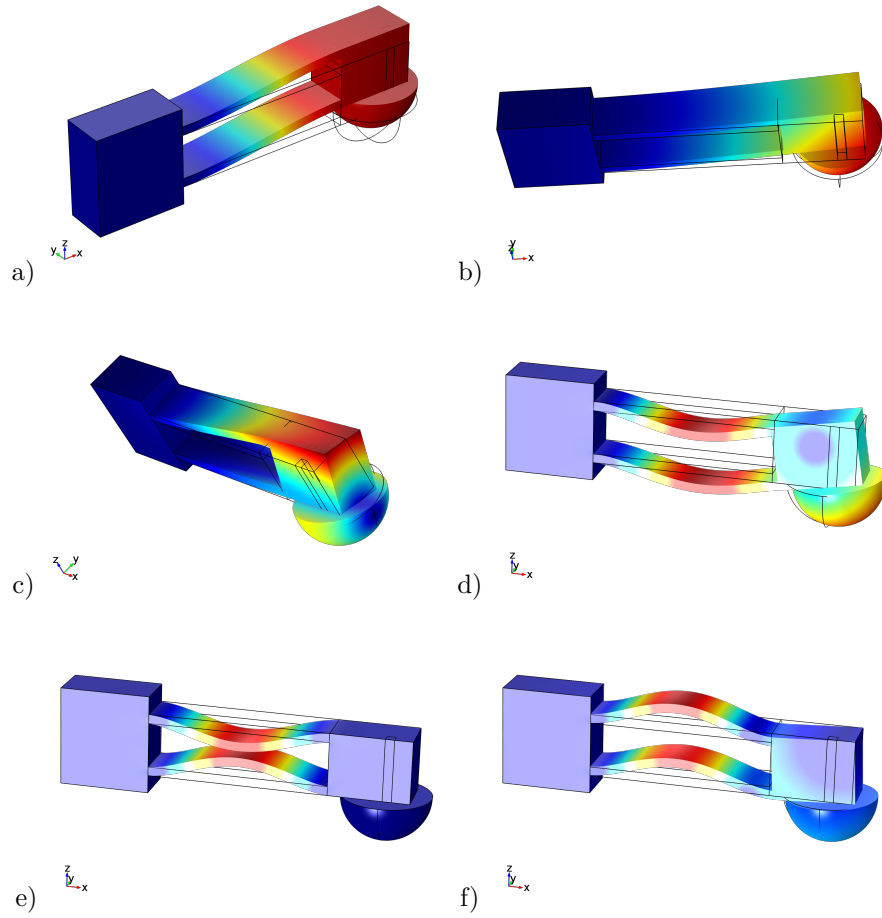
Figure 4.2: The first six modes of the force sensor. a) is the main operation mode of the sensor with frequency ω_0. The color describes the total amount of displacement, where red is maximum displacement, yellow medium displacement and blue low or no displacement. Mode b): $1.53\omega_0$. The third mode is the torsion mode c): $4.29\omega_0$. Mode d): $10.28\omega_0$, mode e): $13.29\omega_0$ and mode f): $14.49\omega_0$.

L	h	t	d	l	r	k	f_0	$f_{K,0}$	$\mathrm{d}f/\mathrm{d}T$
mm	mm	mm	mm	mm	mm	kN/m	kHz	kHz	Hz/K
2	0.1	0.5	0.5	1	0.5	8.2	15	10	1.052

Table 4.1: Parameters of the force sensor. f_0 is the first eigenfrequency without the sphere attached and $f_{K,0}$ is the frequency of the first mode with an attached sphere, $\mathrm{d}f/\mathrm{d}T$ is the simulated temperature dependence of the resonance frequency. and k is the stiffness of the force sensor. t is the thickness of the force sensor, L is the length of the legs of the force sensor, d is the distance between both legs, h is the height of a leg, r is the radius of the half-sphere and l is the length of the test mass. See also Fig. 4.1 for the geometrical description.
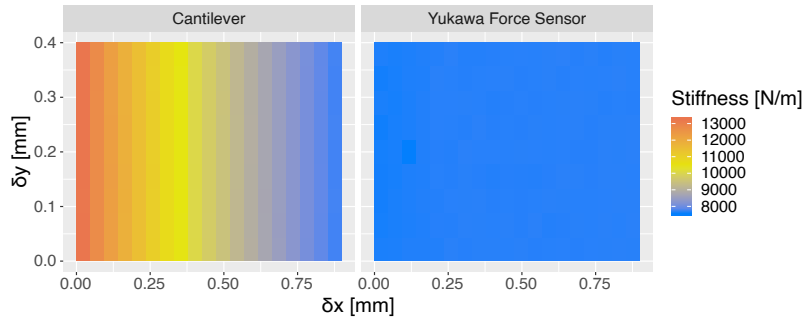
Figure 4.3: On the left is the stiffness of a cantilever dependent on the position of the applied test mass. On the right side is the same plot for the parallelogram flexure. It is obvious that the stiffness is independent of the y-position of the force.
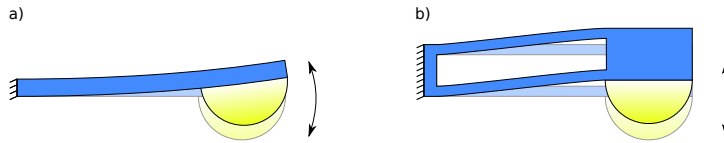

Figure 4.4: a) shows the rotating cantilever movement, and b) shows the linear movement of the parallelogram flexure.

4.1.2   Comparison to a Cantilever

Typical AFMs make measurements using a cantilever. Mostly they use beam deflection and a quadrant photodiode for simultaneous detection of bending and torsion of the cantilever [119]. Other methods are piezoresistivity that uses the change of the cantilevers resistance as it bends to measure the bending [120] and piezoelectric cantilevers that are able to actuate the cantilever at the same time as it is read out [121]. All three methods make it difficult to directly trace the amplitude of the cantilever. The Fabry-Pérot interferometer used in this experiment makes it easy to read out the amplitude and also to fine tune the sensitivity of frequency measurement. This was also done with a cantilever [122]. But as a cantilever bends, it is not easy to trace the amplitude of the Fabry-Pérot read-out on the back of the cantilever directly to the amplitude of an attached sphere. This is due to different bending amplitudes on different positions of the cantilever as an effect of a differing stiffness at different positions of the cantilever as seen in Fig. 4.3. The test mass attached to the parallelogram flexure does not contribute to the stiffness, and therefore has the same stiffness at all positions on it.

The test mass has also the advantage of linear movement. Bending a cantilever results in a rotation of the sphere or cantilever tip, as shown in Fig. 4.4.

4.1.3 Quality Factor

The quality factor Q is defined as the quotient of the stored vibration energy and the energy loss per vibration cycle [123]:

$$Q = 2\pi \frac{\text{energy stored}}{\text{energy dissipation}} \tag{4.1}$$

Alternatively, an identical definition of Q is based on the resonance frequency ω_r and its bandwidth $\Delta\omega$, the bandwidth means the full width at a half maximum:

$$Q = \frac{\omega_r}{\Delta\omega} \tag{4.2}$$

A large Q means a more pure resonance frequency and makes the experiment more sensitive to small changes in the resonance frequency. A higher quality factor is obtained by reducing the energy dissipation. That means it is important to understand the force sensor's energy sinks. For example: air dampens vibration and decreases the quality factor.
Sandberg et al. [124] investigated the most important influences on the quality factor, which leads to the following equation:

$$\frac{1}{Q} = \frac{1}{Q_i} + \frac{1}{Q_s} + \frac{1}{Q_a} + \frac{1}{Q_c} + \frac{1}{Q_g} \tag{4.3}$$

Q_i is the intrinsic quality factor of the material. Slocum [125] gives $Q_i = 10^6$ for fused silica. Q_a is the quality factor of the surrounding gas. For air it is of about $Q_a \approx 10^2$. As for Gerberding et al. [126], the Q_a in vacuum $< 10^{-6}$ mbar does not play a role. Q_s is the energy loss due to the support. A large $10 \times 10 \times 20$ mm^3 cuboid is used as support block, and optical contact bonding is used as adhesion method. In the cuboid, a hole is milled to place the sensor over the hole, and to have full support of the cuboid on the end of the parallelogram flexure. For this setup, the measured Q was about 10^5. Therefore the Q_s has to be $Q_s \approx 1.11 \cdot 10^5$. Another influence comes into play, when the fibers and the sphere are glued to the sensor, Q_g. The last influence comes from the gold coating Q_c.

4.1.3.1 Gold Coating

An electrical contact to the sphere is necessary to measure the distance between the half-sphere and the plate. For this the force sensor was coated with a 10 nm titanium layer and 200 nm layer of gold on top. According to Broch [127] the coating influences the energy loss:

$$\eta \simeq 14 \left(\frac{\eta_2 E_2}{E_1} \right) \left(\frac{d_2}{d_1} \right)^2 \tag{4.4}$$

$$\eta = \frac{1}{Q_c} = 2\xi \tag{4.5}$$

where d_1 is the thickness of the sensor strut, E_1 is Young's modulus of the sensor material, d_2 is the thickness of the coating and E_2 is Young's modulus of the coating. η_2 is the loss factor of the coating material.
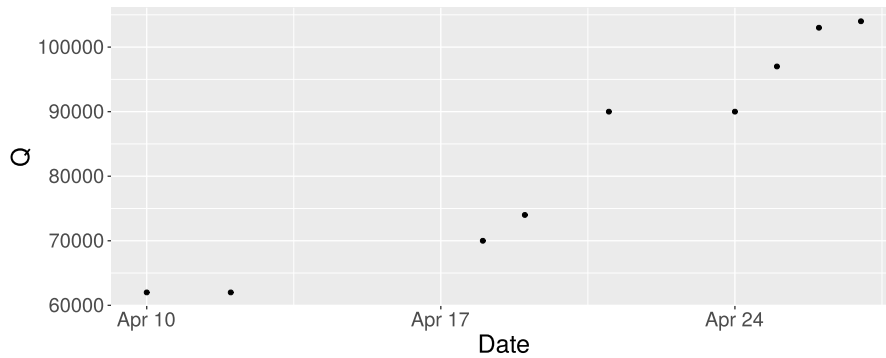
59

Figure 4.5: Different measurements of the quality factor of the same force sensor. The force sensor was in the vacuum chamber for the entire timespan after glueing fibres on it in April 2017. The pressure was about 10^{-6} mbar.

4.1.3.2 Time Dependence of Q

Since a glue takes some time to set, also Q takes some time until it reaches its final value. In one measurement, we glued the fibers to the force sensor, then put it into the vacuum chamber on the 10th of April 2017. Q was measured several times over a period of two weeks. The results are shown in Fig. 4.5. As can be seen, Q increased by about a factor of two in two weeks. For this measurement neither the half-sphere nor the gold coating was applied.

4.1.3.3 Specimen holder

The force sensor itself is a small piece of fused silica with a thickness of 0.5 mm. The energy loss of the oscillator depends a lot on how the the force sensor is attached to the specimen holder. Two bonding types were compared to each other. The first one was optical contact bonding [128] and the second one was hydroxide-catalysis bonding [129].
The quality factor of the oscillator was measured for both bonding types, and both had similar results of about 20000. But the bonding method isn't the only contribution to Q — the position of the force sensor on the specimen holder is another factor. In the first attempts the oscillating part of the sensor was in front of the glass block that was used as specimen holder. This has the disadvantage that the connection of the oscillator to the rest of the sensor was free floating as it is shown in Fig. 4.6. To improve this, a hole was milled in the glass block where the oscillating part of the force sensor is placed. Fig. 4.7 shows how the force sensor is placed on the the glass block and not longer free floating. With this the quality factor of the oscillator improved a lot.
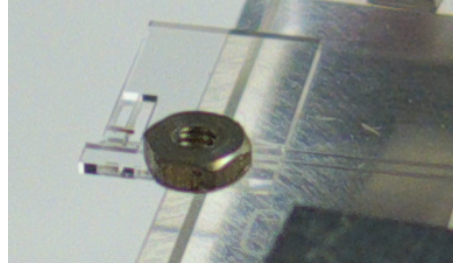
Figure 4.6: The force sensor is placed on a glass block and it is half floating with its connection plate. The screw nut was used to keep the fibers at place before they were glued on the glass block.
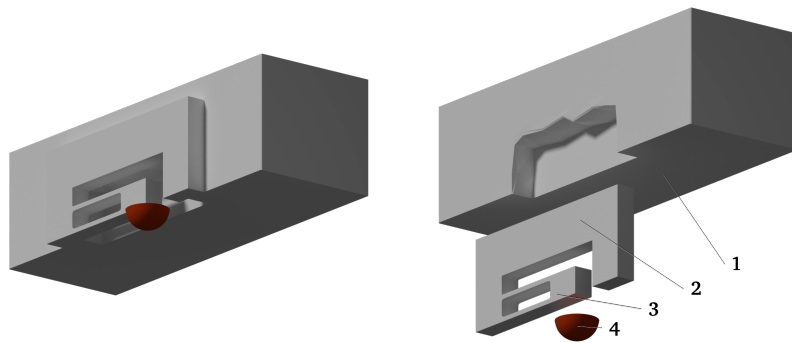

Figure 4.7: 1) is the specimen holder, 2) is the connection plate of the force sensor 3) is the parallelogram flexure of the force sensor and 4) is the ruby half-sphere. As can be seen on the left, the connection plate is not floating, especially is not the left part of it where the parallelogram flexure is attached.
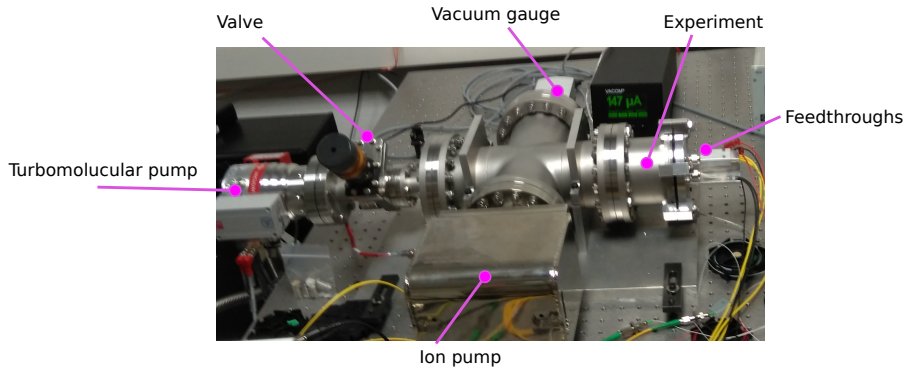
Figure 4.8: Photograph of the vacuum chamber. It shows the turbo pump, the valve between the turbo pump and the rest of the vacuum chamber, the ion pump, the vacuum gauge, the flange with the experiment inside and the fiber and electrical feedthroughs.

4.2 Vacuum Chamber

A high quality factor Q is needed to achieve a good signal for the force measurement. Air dampening is an important influence that reduces the quality factor. To get a high quality factor, the experiment is placed in a vacuum chamber.
The vacuum chamber is built from a cross fitting. On one flange the experiment is attached. Another flange has the vacuum gauge attached. On the third flange is a valve and behind that valve is a turbo pump attached. The turbo pump has a driving frequency of 1500 Hz. The backing pump is attached to the turbo pump. On the fourth flange of the fitting an ion pump is attached. The ion pump needs a high vacuum before it can be started. When this condition is reached and the ion pump runs, the valve will be closed and the turbo pump as well as the backing pump are turned off. The ion pump is needed to avoid coupling the rotation of the turbo pump into the experiment. Fig. 4.8 shows a photograph of the vacuum chamber.

4.2.1 Vacuum Feedthroughs

Measurements inside the vacuum chamber require electrical connections as well as fiber connections. Fig. 4.9 shows the concept of the vacuum feedthrough and Fig. 4.10 shows a photograph of the fiber feedthrough. There are three of those feedthroughs on the flange of the experiment. One feedthrough is for the three optical fibers, and two feedthroughs are for the electrical connections, with four wires per feedthrough. The feedthrough design with the Teflon ferrule comes from Abraham and Cornell [130] and was modified to fit more fibers and wires inside the vacuum chamber. This feedthrough design has the advantage over commercial ones that it uses much less space on the flange and does not need any connectors inside the vacuum chamber. Also with the optical fibers going directly inside the vacuum chamber there is no additional fiber coupling loss [131] [132]. The only disadvantage with this kind of feedthrough is that the pressure inside the vacuum chamber never got below $1 \cdot 10^{-7}$ mbar. With a commercial
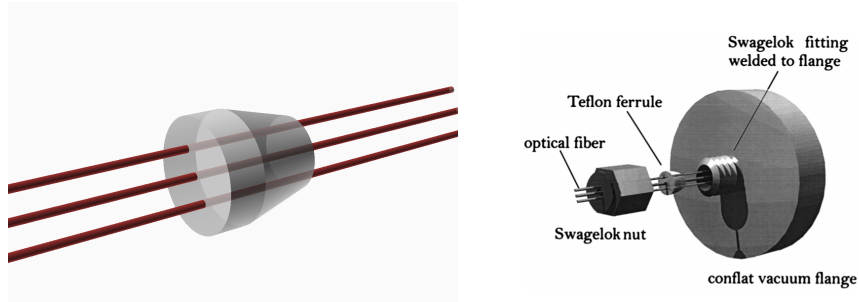
Figure 4.9: The vacuum feedthroughs of the optical fibers and for the electrical contacts are made from a *Swagelok* fitting and a Teflon ferrule. The Teflon ferrule for the optical fibers has three holes with fibers in it. The Teflon ferrule for the electrical contacts has four holes for the wires.
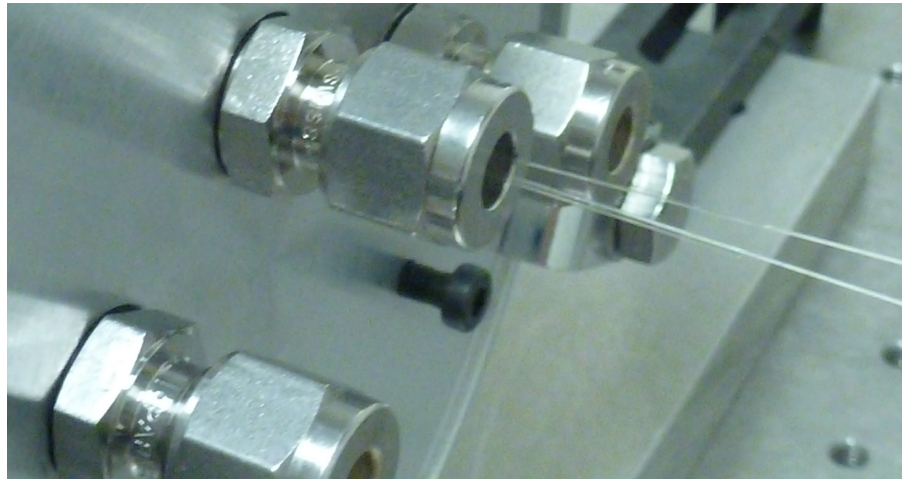

Figure 4.10: Photograph of the fiber feedthrough. It shows the *Swagelok* fitting and the three fibers.

feedthrough ultra high vacuum would be possible [133] but it is not needed for this experiment [18].
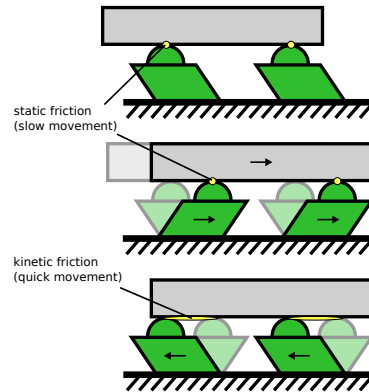
Figure 4.11: Function principle of a stick-slip piezo stage as shown in Breguet et al. [134].

4.3 Piezo Slides

To change the distance between the sphere and the plate, a piezo slide is used. The slide is a MS5 unit from *Scienta Omicron*. The MS5 uses the stick-slip principle. It is shown in Fig. 4.11. A single step is performed, by slowly increasing the voltage, which leads to a movement of the piezo, and the slider of the piezo sticks to the piezo. Then the voltage changes polarity very fast, so the piezo moves fast enough back to the starting position. This fast movement back leads to a slip. The slider stands still and is not traveling back.

With this method, the voltage is only applied during a single step. This has the advantage, that the positioning system applies no additional force due to piezo voltage during the measurements between the steps. The specified minimum step size was 40 nm with a total travel distances of 5 mm. One slide has its movement axis in the force measuring axis. This slide is used for coarse positioning. The other slide is angled by 15 degrees. We were able to reduce a minimum step size to about 12 nm. With the angled slide the average approach of the plate to the sphere is about $3\,\text{nm} \pm 1\,\text{nm}$ as shown in Fig. 4.12.

For the measurement of the step size we used a twenty year old manual controller that was originally built for a scanning tunneling microscope. But for this experiment we wanted to use a computer-controlled controller. So we purchased the new MSCUv4 unit by *Scienta Omicron*. It used a Beckhoff SPS system to program it. Unfortunately, *Scienta Omicron* discontinued the MSCUv4 before they managed to finalize a documentation, and it was not possible to program it directly. Instead, we had an example application that allowed manual control. To use that we started the application inside a virtual machine and simulated the mouse buttons that clicked on the controls in the application. With this setup it was possible to program the piezo slides. As the next step we tried to replicate the results of the step size measurement. Unfortunately we found out that the controller only allowed for specific step size settings that represented percentages of the maximum voltage used to control the piezos. The setting allowed only for 20 %-steps with the minimum being 20 %. That setting resulted in a step size of 40 nm
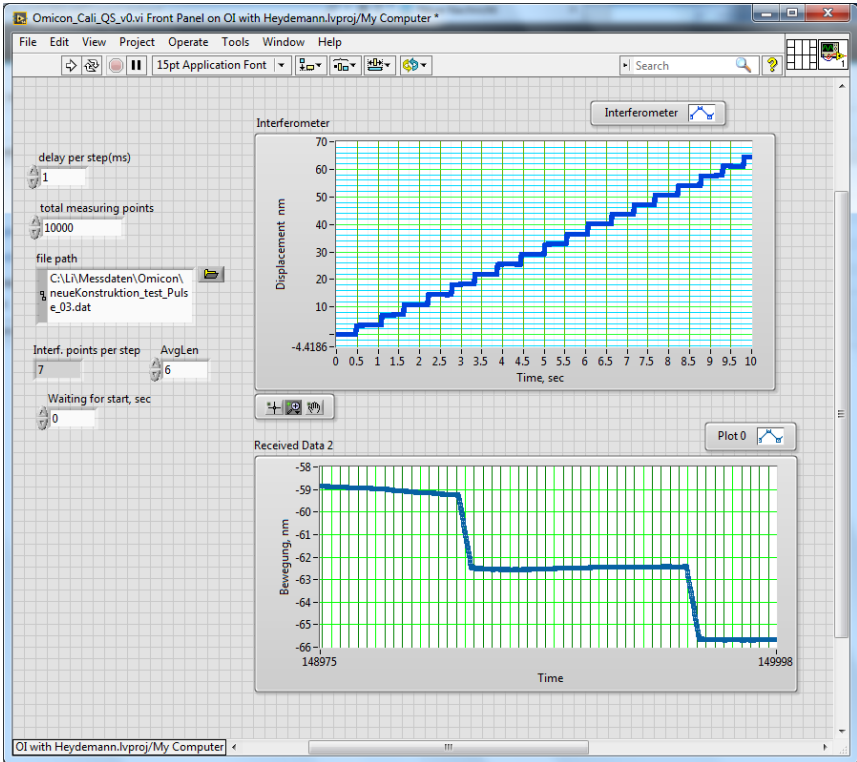
Figure 4.12: Step size measurement of the angled piezo slide. Thanks to Z. Li for providing this measurement.
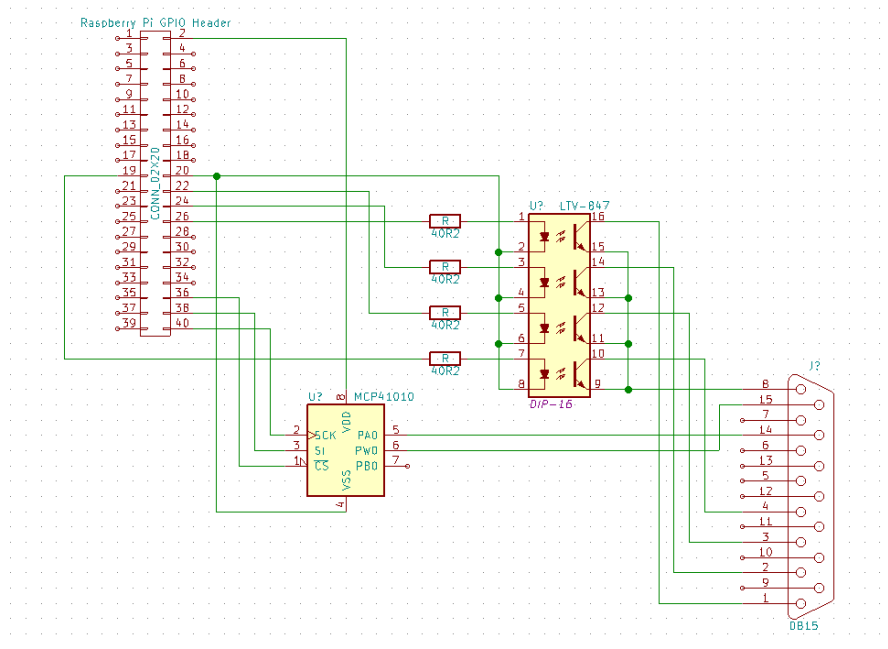
Figure 4.13: Schematic of the opto-couplers attached to the Raspberry Pi and their connection to the old Omicron-controller.

that was documented. On the old controller the step size was adjusted continuously with a potentiometer. Below a certain setting, the piezo slides were not able to move at all, but it was possible to find that setting and go just above it to get a minimum step size.

The logical next step was to analyze the manual control of the old controller and build our own controller that was adjustable by the computer. For the four direction keys, we used four opto-couplers that were attached to GPIOs of a Raspberry Pi mini computer. For the step size control we used a computer adjustable potentiometer that was also attached to the Raspberry Pi. The schematic is shown in Fig. 4.13. A setting of $23.7\,\mathrm{k\Omega}$ proved to be the optimum setting in this case.

Also the step size was found to be not constant. Over a period of several hours the step size drifted from $3\,\mathrm{nm}$ to $4\,\mathrm{nm}$. The measured mean was $3.1\,\mathrm{nm}$ as shown in Fig. 4.14.
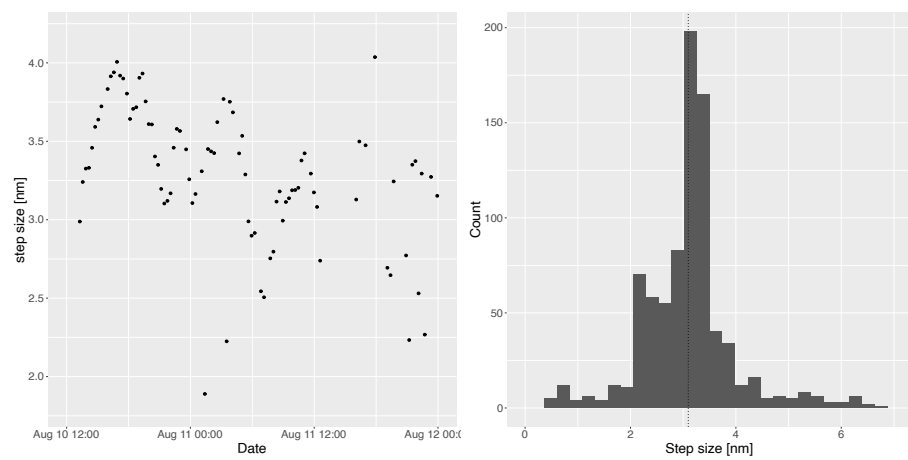
Figure 4.14: The left shows how the step size measured in summer 2016 changed over time and the right shows the distribution of step sizes measured over a whole week. The mean value of the step sizes was 3.1 nm and its standard deviation was 0.9 nm.
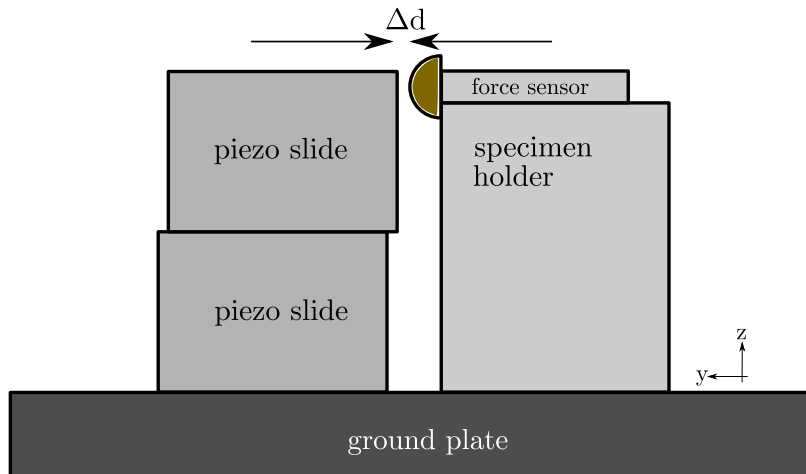
Figure 4.15: Simulation model of the thermal drift. The block at the bottom is the ground plate. The simulations were done for aluminum, Invar and Zerodur as ground plate materials. The specimen holder and the force sensor were simulated as fused silica and the piezo slides were simulated as solid blocks of Invar.

4.4   Thermal Drift

Section 4.1.1 described how the resonance frequency of the force sensor is temperature dependent. But changing the temperature also has other effects. Thermal expansion can also cause the distance between the sphere and the plate to change. This is a parasitic effect that should be avoided. To optimize the experiment for distance changes due to thermal expansion, simulations with different materials as base plate were performed. The three candidates as base plate material were aluminum, Invar and Zerodur. While aluminum is easy to machine, Invar and Zerodur are optimized materials for low thermal expansion. Fig. 4.15 shows the simulation model for this simulation and Table 4.2 shows the results. Zerodur and Invar are an order of magnitude lower in the distance change than aluminum. While Zerodur has a lower thermal expansion coefficient than Invar, Invar wins in the simulation. The reason is, that the piezo slides are made of Invar as well, and the expansion of the Invar ground plates gets partly compensated by the expansion of the piezo slides. Following the results of the simulation, we chose to make the ground plate of the experiment out of Invar. The lateral position change Δy and the height change Δz should in theory not change the experimental outcome, but it's possible that a local change in the surface roughness distribution might cause an effect.

4.4.1   Temperature Measurement

To measure the temperature, a NTC sensor is placed on the Invar ground plate in the vacuum chamber between the fused silica block and the vacuum flange. The nominal resistance value of the NTC is $10\,\mathrm{k\Omega}$. A BK Precision 2831E Multimeter is used to measure the resistance. The resistance measurement is performed once every minute, to reduce the amount of heat

α_L	$\frac{\mu m}{m \cdot K}$	Aluminum		Invar		Zerodur	
		23.1		1.2		0.08	
ΔT	K	1	0.1	1	0.1	1	0.1
distance Δd	nm	500	50	13	1.3	33	3.2
Δy	nm	2	0.2	0.2	0.1	0.1	0.1
height Δz	nm	56	6	35	3.4	33	3.3
Time to steady state	h		<0.5		2		7

Table 4.2: Simulation results of the distance change due to thermal expansion. The distance change between sphere and plate is in the first line Δd, Δy is the lateral change of the position and Δz is the height change between sphere and plate. The simulation model is shown in Fig. 4.15. The values of α_L were taken from *COMSOL 5.1*, the software that also performed the simulation.

caused by taking the measurement to affect the next measurement. The data sheet gives the β value of the used NTC: $R_{ref} = 10000$, $\beta = 3435$, $T_0 = 25\,°\mathrm{C}$

$$T = \left(T_0 \beta \ln \frac{R_{ref}}{R} \right) / \left(\frac{\beta}{\ln \frac{R_{ref}}{R}} - T_0 \right) \tag{4.6}$$

Measuring the temperature on the ground plate means that a temperature increase outside the vacuum chamber would reach the temperature sensor a couple of minutes before reaching the force sensor. This time delay has to be measured and taken into account when correcting the frequency by temperature.
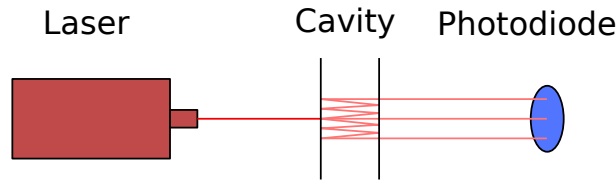
Figure 4.16: Basic Fabry-Pérot design.

4.5 Interferometric Length and Movement Measurement

The oscillation amplitude of the force sensor is below $1\,\text{nm}$. An interferometric method is the best approach to measure these small position changes. In interferometers two or more coherent waves are superposed. The resulting intensity depends on the phase difference of the waves.

Optical interferometers can be divided into general types depending on the amount of interfering beams. A Fabry-Pérot type is based on multiple-beam interference. A Fabry-Pérot is build from two transparent opposing mirrors with a certain reflectivity. The two mirrors form a cavity. Fig. 4.16 shows the basic principle of a Fabry-Pérot. In the base setup [135], a beam is launched into the cavity through a transparent mirror. The beam is subsequently reflected multiple times at the opposing mirrors while transmitting a part of itself through the mirror at each reflection. How much of the light gets reflected in each cycle depends on the reflectivity, which is about $4\,\%$ for uncoated vacuum-glass interface in normal incidence. The geometric phase difference δ to a directly transmitted beam of a Fabry-Pérot is given by:

$$\delta = \frac{4\pi L n}{\lambda}\cos\theta \tag{4.7}$$

where L is the cavity length, n is the refractive index, λ is the laser wavelength and θ is the tilt angle between the parallel mirrors. The intensity of the transmitted light I_t, after summing up all reflected parts of the beam inside the cavity, is as stated by Zinth [135]:

$$I_t = I_0 \frac{(1-R)^2}{1-2R\cos\delta + R^2} \tag{4.8}$$

This experiment uses two such interferometers, but instead of the transmitted light, the reflected light is used. The schematic is shown in Fig. 4.17. The intensity of the reflected light can be calculated with Eq. (4.9) under the assumption of an normal incident angle and a neglectable absorption inside the cavity. The intensity of the reflection at perpendicular incidence and zero absorption is given by [136]:

$$I_r(FP) = 2RI_0 \frac{1-\cos\delta}{1+R^2-2R\cos\delta} \tag{4.9}$$

where I_0 is the induced optical power, R is the reflectivity of the optics.
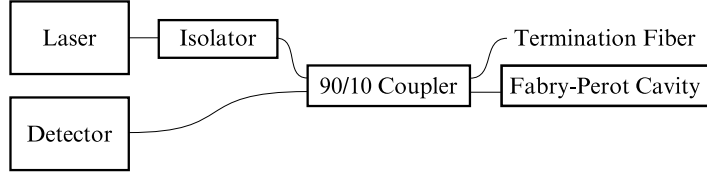
Figure 4.17: Schematic of the fiber Fabry-Pérot interferometer.

Normalizing Eq. (4.9) to the maximal $I_r(FP)$ gives:

$$\frac{I_r(FP)}{I_{max}} = \frac{(1+R)^2}{2}\frac{1-\cos\delta}{1+R^2-2R\cos\delta} \qquad (4.10)$$

The intensity of the reflected light is measured with a photodiode. The resulting current was converted to a voltage with a transimpedance amplifier. We used the avalanche photodiode model PDA10CS-EC by Thorlabs. For the voltage conversion one needs a constant of proportionality V_p that depends on the conversion gain and an offset voltage V_{off}. Then the measured voltage will be [126]:

$$V = V_{off} + V_p\frac{(1+R)^2}{2}\frac{1-\cos\delta}{1+R^2-2R\cos\delta} \qquad (4.11)$$

The parameters of the movement measurement were calibrated using the wavelength of the tunable laser Agilent 8164B as calibration standard. We used two 90/10 Thorlabs 10202Aŋ90ŋAPC fiber couplers and the optical isolator IOŋHŋ1550APC from Thorlabs. Two single mode patch cables (Thorlabs P3-1550A-FC-1) were used to cut one end off and place them into the experiment as ends of the fiber interferometers. The other ends were connected to the fiber couplers using FC/APC mating sleeves. One 50/50 fiber coupler (Thorlabs 10202A-50) was used to split the signal from the laser source into two signals for both interferometers. The optical fibers only have a small aperture and the light emitted at the end of the fibers is divergent. This leads to a deviation from the optimal Fabry-Pérot and a low finesse. A low finesse means, that instead of steep peaks, the measurement result of the intensity vs. cavity length curve is sinusoidal.
To measure the coefficients for the movement measurement the tunable laser was used to shift the wavelength for at least one period of Eq. (4.11). A variation of either the distance between the mirrors or the wavelength results in a periodic signal. Its waveform depends on the offset voltage V_{off}, the conversion gain V_p and the reflectivity of the mirrors R. Therefore the wavelength of the laser was tuned over a range of 1500 nm to 1600 nm. In vacuum $n = 1$. An advantage of the normalization of Eq. 4.9 is that $V_{off} \approx \min V(\lambda)$ and $V_p \approx \max V(\lambda) - \min V(\lambda)$ can be used as a starting point for the fitting routine. To get the other starting points for the fitting, the fit was initialized with a genetic algorithm. Genetic algorithms always have a random component, and tests showed that a quarter of the results for L were too far away for the non-linear fitting routine to find the optimum fit. To overcome this problem, the L_{gen}, the result from the genetic algorithm, is

71
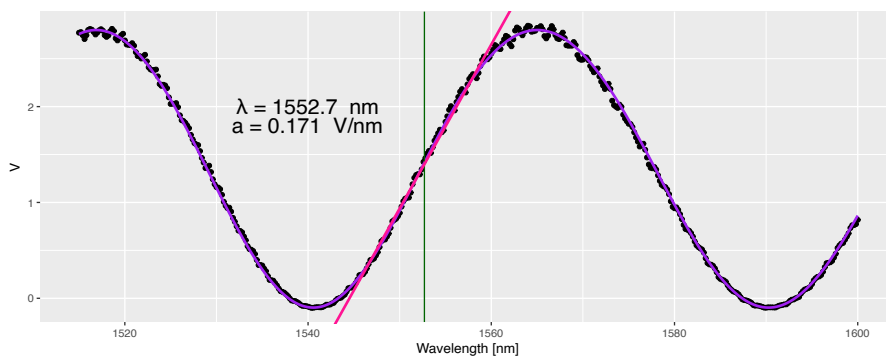
Figure 4.18: Measurement of the vibration cavity on Feb. 2nd 2018. The purple line is the fit of the interferometer, the vertical green line shows λ_{set}. The pink line is the linear fit for the voltage to amplitude conversion from Eq. (4.13).

used and a *grid search* [116] is performed. This means L iterates from $L_{gen} - 5\,\mu\text{m}$ to $L_{gen} + 5\,\mu\text{m}$ with a step-size of $10\,\text{nm}$. For each step, the cross-correlation function between the current fit function and the measured data was calculated. After that, the $\tilde{L}$, for which the cross-correlation function is maximized, is chosen as a starting point for the non-linear fit routine. See chapter 3.8.3.1 for the nonlinear fit routine.

The precision of the distance variation measurement is the highest, where Eq. (4.11) has the steepest slope. The wavelength where the slope is the steepest is λ_{set}, and it is calculated with:

$$\lambda_{\text{set}} = \frac{2L}{\text{round}\left(\frac{2L}{1550\,\text{nm}}\right) + \frac{1}{4}} \tag{4.12}$$

Around λ_{set} the measurement voltage V_{meas} is proportional to the distance variation ΔL. As long as the distance variation is small compared with the wavelength λ_{set}, a linear fit function can be used to calculate the sensitivity factor for the distance variation:

$$\Delta L = a \cdot V_{\text{meas}} + b \tag{4.13}$$

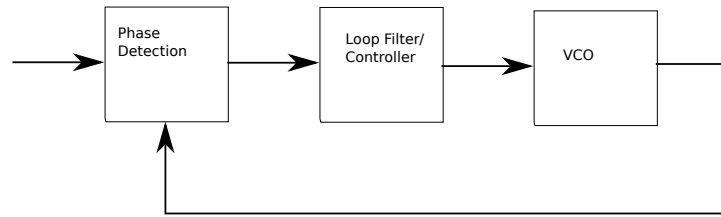The sensitivity factor is a and the offset b. An example of Fabry-Pérot fit is shown in Fig. 4.18.

Figure 4.19: A basic PLL has an input signal (left) and then a phase detector. Afterwards the phase is fed into a loop filter (or a controller) which generates the input signal for the voltage controlled oscillator (VCO). The output of the VCO is used in the phase detection to compare it with the input signal. The VCO is also known as a *local oscillator*.

4.6   Frequency Measurement using a Phase Locked Loop

It is not possible to measure the force directly. Therefore it is necessary to determine the force by means of another effect. In this case, we use the effect whereby a distance dependent force shifts the frequency of an oscillator, as seen in chapter 3.6. The oscillator is driven by an amplitude modulated laser source. We selected the oscillator's resonance frequency as the modulation frequency. This frequency has to be adjusted as the resonance frequency changes during the measurement due to the force. This is done with a feedback loop. The basis of the feedback loop is a phase locked loop, or PLL for short. The basic PLL design is shown in Fig. 4.19.
Usually a PLL is used to lock a local oscillator to an external reference. This allows us to measure the phase and the frequency of the external reference. The local oscillator drives the laser modulation, which drives the oscillation of the force sensor. This oscillation is measured and fed into the PLL as an external reference. This requires some adjustments to the PLL design.
The PLL is implemented as an all digital phase locked loop using the Red Pitaya board. It is built using a Xilinx Zynq 7010 FPGA board and two 14-bit ADCs and two 14-bit DACs. The source code for the FPGA is implemented using Verilog as hardware description language. A very thorough introduction to all digital phase locked loops can be found in the fourth chapter of O. Gerberding's [137] PhD thesis. I will only recount the main aspects as well as my modifications. The design of our PLL is shown in Fig. 4.20.

4.6.1   ADC of the Red Pitaya

The ADC of the Red Pitaya has 14 bit at 125 MHz sampling rate. The PLL uses a lower sampling rate by a factor of 32. That means a sampling rate of 3.90625 MHz. The input voltage of the ADC is in the $[-1, 1]$ V interval.

4.6.2   Phase Detector of the PLL

The input signal of the PLL has a bit depth of 14 bit. The output DAC also has 14 bit, therefore a 14 bit LuT is used for sine and cosine. The 14 bit sine
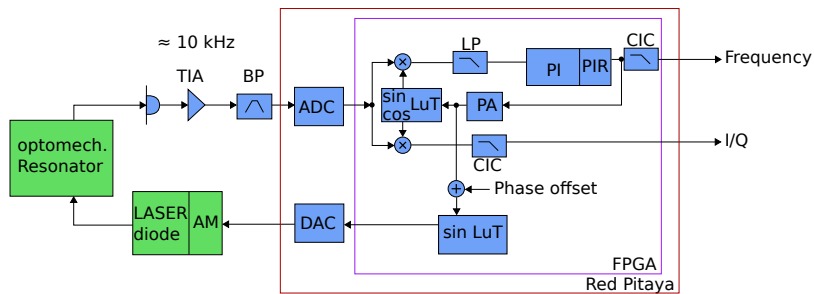
Figure 4.20: Schematic of the phase locked loop. The optical signal hits the photodiode and is transferred with a transimpedance amplifier (TIA) to a voltage signal. To use the whole bit range of the ADC, the signal is bandpass filtered and amplified. The ADC is part of the Red Pitaya board and is connected to the FPGA. On the FPGA the signal is compared with the signal of the local oscillator. The error signal is bandpass filtered and goes into the PI-controller. In the phase increment register (PIR), the phase is stored. The PIR value is accumulated in the phase accumulator (PA) which is fed as phase into the look up tables (LuT). The PIR and the LuT form together the local oscillator. Also another LuT is used for a phase shifted signal, that goes to the DAC. This output signal is optimized to amplitude modulate a laser diode, which drives the optomechanical resonator. And with a laser interferometer, the oscillations of the resonator are measured, and close the loop at the photodiode. With a cascaded integrator comb (CIC), the frequency as well as the in-phase and quadrature components are down sampled and can be read out at a computer interface.

signal is multiplied with the input signal to build up the phase detector, which leads to a 28 bit detected phase signal.

$$\sin \varphi_i \cdot \cos \varphi_{\mathrm{PLL}} = \frac{1}{2} \left(\sin \left(\varphi_i - \varphi_{\mathrm{PLL}} \right) + \sin \left(\varphi_i + \varphi_{\mathrm{PLL}} \right) \right) \tag{4.14}$$

where φ_i is the input phase and φ_{PLL} is the internal phase. $\epsilon = \varphi_i - \varphi_{\mathrm{PLL}}$ is the phase error between the local oscillator and the input. $\sin \left(\epsilon \right) \approx \epsilon$ for the small phase error. The $\varphi_i + \varphi_{\mathrm{PLL}}$ component is filtered out with a low-pass filter.

4.6.3 Low-Pass Filter

As low pass filter, a simple IIR exponential smoothing filter is used. The filter is defined as:

$$\begin{aligned} m_i &= \alpha \epsilon_i + (1 - \alpha) m_{i-1} \tag{4.15} \\ &= \alpha \epsilon_i + m_{i-1} - \alpha m_{i-1} \tag{4.16} \end{aligned}$$

where m_i is the i-th value filter output and ϵ_i is the i-th input value. α is the smoothing factor. With an $\alpha = 2^{-c}$, where c is an integer. For the multiplication, bit shifts are used to make the filter efficient.

4.6.4 Controller inside the PLL

After obtaining the error signal, the signal is fed into a servo. The purpose of the servo is to calculate the control signal to set the output phase to match the input phase. Its output signal goes into the phase increment register or *PIR*. The servo is built using a PI controller with an double integrator added. A double integrator is a second-order control system used to control single degree of freedom motion [138][139] and is therefore suitable to control the motion of our force sensor. The transfer function of the servo is [140][141]:

$$G_{\mathrm{PI}}(s) = \frac{Y(s)}{U(s)} = \kappa_p + \kappa_i \frac{1}{s} + \kappa_{i^2} \frac{1}{s^2} \tag{4.17}$$

The servo has two operational modi.
The first is to measure the frequency of the force sensor without closing the loop. In this case the proportional and the integrator part of the servo are used $\kappa_p \neq 0$ and $\kappa_i \neq 0$ and the double integrator is deactivated with $\kappa_{i^2} = 0$. The second mode has the closed feedback loop, where the PLL drives the force sensor. In this case the proportional part is deactivated $\kappa_p = 0$ and the double integrator is active, i.e. $\kappa_{i^2} \neq 0$.
In the FPGA implementation, both integrators have their own registers. They are implemented as saturating registers. This means, if they overflow, they are set to the maximum possible value. And in case of an underflow, they are set to the minimum possible value.

4.6.5 Phase Accumulator

The servo drives the phase increment register which determines the frequency of the local oscillator. To get a continuous sine one needs a phase accumulator, which is a register where at each cycle the PIR is added to the current value. The periodicity of the phase accumulator is done using a register that overflows. This leads to a saw tooth characteristic for the phase accumulator.

4.6.6 Output Phase Shift

The force sensor as well as the band pass filter that are used to optimize the signal for the ADC on the Red Pitaya introduce a phase shift to the oscillation. This phase shift has to be corrected for when generating the signal to modulate the laser diode. A constant phase shift φ_c is applied to the output signal with respect to the local oscillator.

4.6.7 Sine and Cosine Lookup Table

To generate the sine and cosine signal, a lookup table is used. It uses 16 bit of the phase accumulator as input and has 14 bit output for the DAC and the phase detector. As only one quadrant of a sine has to be present in the lookup table (LuT), it has 2^{14} values, and the other quadrants are derived from that.

4.6.8 Phase and Amplitude Readout

A signal $s(t)$ of a specific frequency ω with a phase modulation $\varphi(t)$ on it can be written as:

$$s(t) = A \cos{(\omega t + \varphi(t))} \tag{4.18}$$

The in-phase $I(s(t))$ component and the quadrature component $Q(s(t))$ are defined by:

$$
\begin{aligned}
I(s(t)) &= A \cos{(\varphi(t))} \tag{4.19} \\
Q(s(t)) &= A \sin{(\varphi(t))} \tag{4.20}
\end{aligned}
$$

To get I and Q from the measured signal, the signal is multiplied by the sine and cosine of the reference frequency [142]:

$$
\begin{aligned}
I(s(t)) &= s(t) \cdot \cos{(\omega t)} \tag{4.21} \\
Q(s(t)) &= s(t) \cdot \sin{(\omega t)} \tag{4.22}
\end{aligned}
$$

The PLL can detect the input phase using the in-phase I and quadrature Q components of the input signal.
The phase is:

$$\varphi = \tan^{-1}\left(\frac{Q}{I}\right) \tag{4.23}$$

And the amplitude is:

$$A = \sqrt{I^2 + Q^2} \tag{4.24}$$

In one measurement procedure, a lot of individual measurements are performed. If the data fits a Gaussian distribution, the arithmetic mean and the standard deviation are calculated to summarize multiple linear measurements. But for a circular quantity a simple mean or standard deviation is not feasible. To get the mean of an angle, one has to calculate the center of mass of all points on a unit circle [143]:

$$\bar{\phi} = \tan\left(\frac{\sum_i \sin{\phi_i}}{\sum_i \cos{\phi_i}}\right) \tag{4.25}$$

and

$$\bar{r} = \sqrt{\left(\frac{1}{N}\sum_i^N \sin\phi_i\right)^2 + \left(\frac{1}{N}\sum_i^N \cos\phi_i\right)^2} \tag{4.26}$$

where ϕ_i is the i-th measured phase angle and $\bar{\phi}$ is the mean phase angle, N the total number of measurements and $\bar{r}$ is the mean radius of the circle. If $r \approx 1$, the $\bar{\phi}$ is sharp at that phase and if $r \approx 0$, the phase are pretty much equally distributed.[1]

4.6.9 Cascaded Integrator Comb

To get data out of the FPGA, a cascaded integrator comb (CIC) was used [144]. The cascaded integrator comb is an accumulator register with $n + m$ bit. n is the number of bits of the output signal and 2^m is the number of FPGA-cycles. In each cycle, the current value is added (*integrated*) to the accumulator. After 2^m cycles, the most significant n bits are stored as down sampled output value. Also the accumulator register is zeroed afterwards. This is equivalent to the mean value out of 2^m samples:

$$\bar{q} = \frac{1}{2^m}\sum_{i=1}^{2^m} q_i \tag{4.27}$$

With $m = 20$, the data is down sampled to $3.73\,\text{Hz}$. With this method, the in-phase component, the quadrature component, and the frequency are sampled from the FPGA and read out by the connected computer.

4.6.10 Bandpass Filter of the Vibration Signal

A bandpass filter was placed between the photodiode of the vibration measurement interferometer and the phase locked loop to optimize the input signal for the ADC of the PLL. Two Sallen-Key bandpass filters were connected in series. Fig. 4.21 shows the transfer function of one bandpass, and Fig. 4.22 shows the schematic and, a picture of the circuit board.

4.6.11 Starting the PLL

To start the PLL, the feedback loop has to be closed. Also a default PIR offset that is near the resonance frequency is used to make coarse adjustments. The servo does the fine readjustment of the PIR. The PLL starts at the coarse offset frequency and it takes some time until the resonant frequency is reached. The frequency read-out using the CIC reads out the PIR and is calculated back to the resonance frequency. Fig. 4.23 shows the transient response of the PLL started at $10906\,\text{Hz}$.

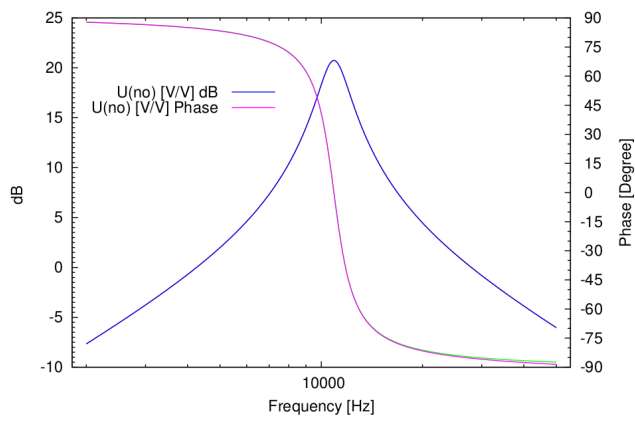[1]See `https://en.wikipedia.org/wiki/Von_Mises_distribution` for the circular equivalent of the normal distribution

Figure 4.21: Transfer function of the bandpass used to optimize the photodiode signal.
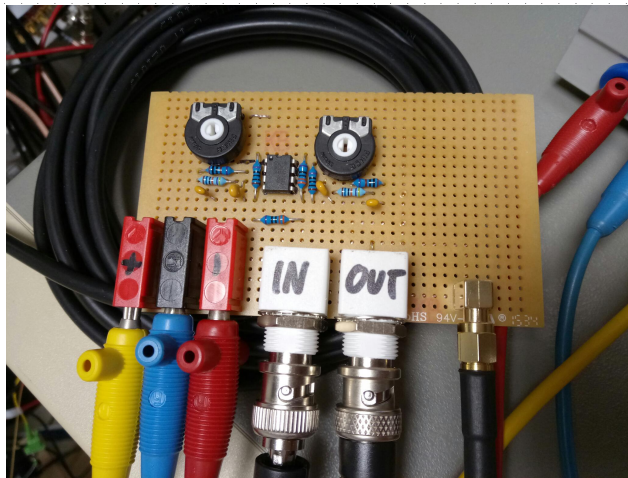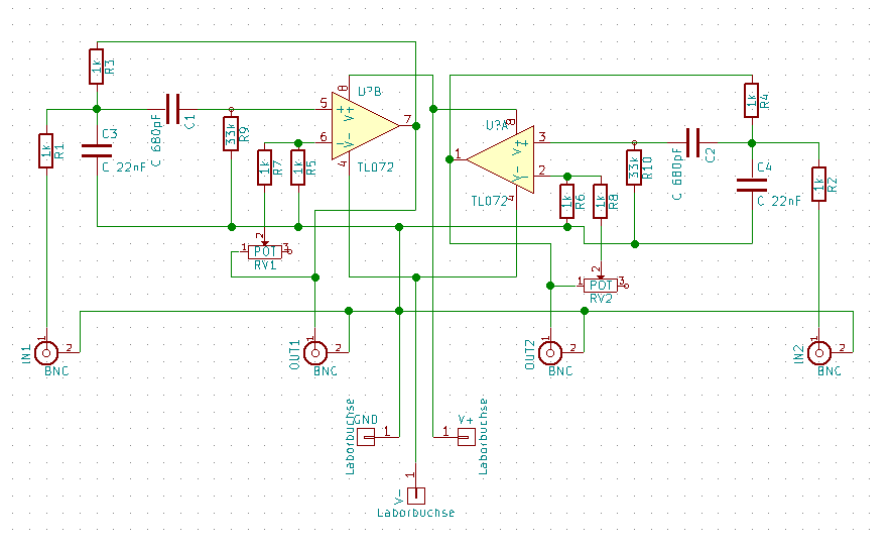
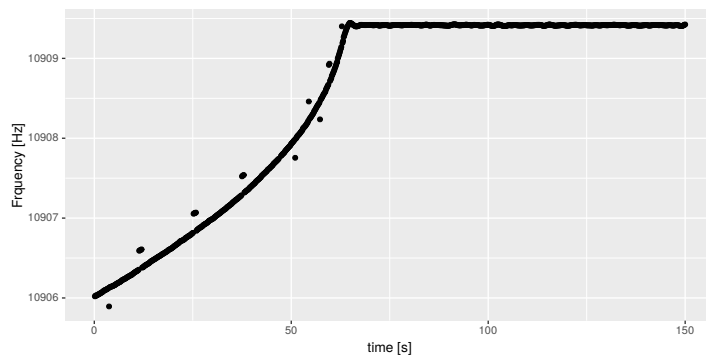Figure 4.22: Bandpass filter. Both Sallen-Key filters have an adjustable filter gain.

Figure 4.23: Transient response of the PLL, when started at a Frequency of 10906 Hz. During the transient response sometimes a phase shift jump occurs. If the output phase shift of the PLL was set to the correct value, the phase jumps did not happen in the settled down PLL.

4.7 Alternative: Frequency Measurement using a Lock-In Amplifier

While the phase locked loop was a great tool to measure and track the resonant frequency, it was not always possible to use it. If the resonance amplitude was very small, the PLL was not sensitive enough to measure. In those cases a different frequency measurement technique was used. The modulation of the laser source was done by a frequency generator. The same signal was also fed to a lock-in amplifier as reference. The lock-in amplifier converted the amplitude of the signal into a constant voltage that was measured with a PicoScope USB oscilloscope. The measurement was done at different frequencies around the expected resonance frequency. That lead into a resonance curve. Afterwards the resonance curve was fitted and resulted in some information about the resonance frequency and the quality factor Q. The main disadvantage of this measurement method was that it took a couple of minutes to measure one resonance curve and is therefore much more prone to thermal drift than the PLL method. We used the SR830 Lock-in amplifier model. It uses two power spectral densities (PSDs) to calculate the amplitude and the phase difference between the signal and the reference signal. However, they state that the phase output works best with higher amplitudes. The analog amplitude output represents V_{rms}.

When plotting the resulting resonance curve with frequency on the x-axis and the squared amplitude V_{rms}, the curve follows a Cauchy-Lorentz distribution:

$$y(f) = y_0 + \frac{A}{\pi} \left(\frac{s}{(f - f_0)^2 + s^2} \right) \tag{4.28}$$

where $y(f)$ is the amplitude function, y_0 is the offset, A is the area scale of the distribution, s is the half width at half maximum, meaning that $2s$ is the full width at half maximum, and f_0 is the resonance frequency. The quality factor is now:

$$Q = \frac{f_0}{2s} \tag{4.29}$$

The maximum $y(f)$ is at the resonance frequency $y_{\mathrm{max}} = y(f_0)$:

$$y_{\mathrm{max}} = \frac{A}{\pi} \left(\frac{s}{s^2} \right) \tag{4.30}$$

With the normalization factor $\bar{n}$, the gain of the lock-in amplifier T and the voltage to digital conversion factor V_x, the real amplitude at resonance is:

$$V_{\mathrm{rms}} = \sqrt{y_{\mathrm{max}}} \cdot \bar{n} \cdot V_x \cdot T^{-1} \tag{4.31}$$

With a 16-bit signed integer representation of a $10\,\mathrm{V}$ signal this leads to a conversion factor of:

$$V_x = \frac{10}{2^{15}} \frac{\mathrm{V}}{\mathrm{skt}} \tag{4.32}$$

In the case of the example resonance curve in Fig. 4.24, the measured parameters are $\bar{n} = 830.2206\,\mathrm{skt}$ and maximum $y_{\mathrm{max}} = 5.50$. The sensitivity setting of the lock-in amplifier was set to $2\,\mathrm{mV}$. That means that an amplitude of $2\,\mathrm{mV}$ would be measured as $10\,\mathrm{V}$ on the output of the lock-in amplifier and it results to a gain factor of $T = 5000\,\frac{\mathrm{V}}{\mathrm{V}}$.
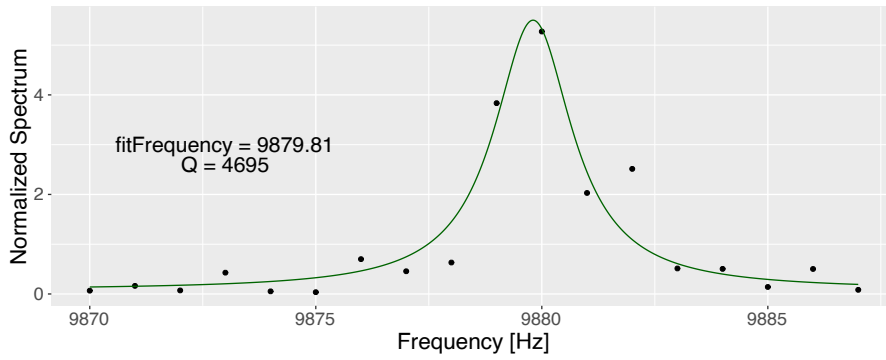
Figure 4.24: Measurement of the resonance curve from 12th December 2016 using the SR830 lock-in amplifier.

The real amplitude voltage V_{rms} is:

$$V_{\mathrm{rms}} = 118.85\,\mu\mathrm{V} \tag{4.33}$$

At the time[2] of the measurement of the resonance curve, the voltage to length calibration factor of the interferometer was:

$$a = (61.546 \pm 0.094)\,\frac{\mathrm{nm}}{\mathrm{V}} \tag{4.34}$$

The amplitude at resonance of the force sensor vibration is now:

$$x_{\mathrm{rms}} = a \cdot V_{\mathrm{rms}} = 7.31\,\mathrm{pm} \tag{4.35}$$

The theoretical amplitude for a perfect square wave shaped $8\,\mathrm{mW}$ laser actuation is, following eq. (4.41):

$$\begin{aligned}
\bar{x}_{\mathrm{pp}} &= Q \cdot 6.37\mathrm{fm} = 29.9\,\mathrm{pm} \tag{4.36} \\
\Rightarrow \bar{x}_{\mathrm{rms}} &= 10.78\,\mathrm{pm} \tag{4.37}
\end{aligned}$$

The theoretical maximum possible amplitude at the given Q is about $45\,\%$ larger than the measured amplitude in this case. Section 4.8.2 describes how the waveform of the $8\,\mathrm{mW}$ laser was optimized.
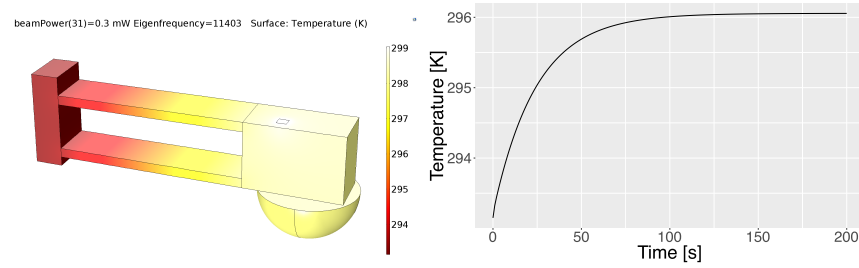
---

[2]2016-12-12

Figure 4.25: On the left: Simulated temperature distribution of the force sensor, the color bar on the right is in Kelvin. The actuation laser radiates at the white spot on the force sensor and heats it up. On the right: Simulated heating up the force sensor, averaged over the right face of the test mass.

4.8 Optical Actuation

To use the frequency modulated AFM technique, the parallelogram flexure has to vibrate. There are different ways to achieve that. Most FM-AFM applications use piezo crystals. Piezos change their size due to an applied voltage (as well as the other way round). To get a vibration, large electric fields are necessary. As shown in section 4.3, these voltages can lead to larger forces than any gravitational effect. Also piezos have displacement hysteresis that lead to heating up the system and the heating increases with frequency [145]. To avoid this, optical actuation is used. Wilkinson et al. at NIST [146] used this method to calibrate the stiffness of a cantilever. The optical actuation is built from an amplitude modulated red laser source. One disadvantage of using the light pressure method is that the light heats up the parallelogram flexure. This means that it is necessary to get to the thermodynamic equilibrium before starting a measurement. This takes about three to five minutes. The temperature distribution through heating up the force sensor is shown in Fig. 4.25. Fig. 4.25 also shows the simulated time to equilibrium.

4.8.1 Amplitude of Vibration at Resonance

As described in section 3.5.4, radiation leads to a force on a mirror. This force was described by Eq (3.143). Taking into account the reflectivity R, it leads to the force F_0:

$$F_0 = \frac{2PR}{c} \tag{4.38}$$

P is the power of the light with perpendicular incident.
Using the Eq. (3.176) for the resonance amplitude derived in section 3.7:

$$A_{\text{res}} = \frac{Q}{\sqrt{1 - (\frac{1}{2Q})^2}} \frac{2PR}{ck} \tag{4.39}$$

With $Q \gg 1$ follows $\sqrt{1 - (\frac{1}{2Q})^2} \approx 1$. This leads to Eq. (3) from Melcher et al. [18]:

$$A_{\text{res}} = \frac{2PRQ}{ck} \tag{4.40}$$

With a Laser power of $P = 8\,\text{mW}$ and the reflectivity of gold of about $R = 0.98$ and a stiffness of $k \approx 8200\,\text{N}\,\text{m}^{-1}$ one gets:

$$A_{\text{res}} = Q \cdot 6.37\text{fm} \tag{4.41}$$

That means an amplitude of $0.6\,\text{nm}$ in case of $Q = 10^5$ and $0.06\,\text{nm}$ in case of $Q = 10^4$. Values between $0.1\,\text{nm}$ and $1\,\text{nm}$ are a good compromise between measuring the force with a lower amplitude as stated in section 3.6 and having a reasonable high sensitivity of measuring the oscillation as stated in section 4.5. Note that the calculated amplitude A_{res} is the peak to peak amplitude.

4.8.2 Optimization of the Optical Waveform

Melcher et al. [18] used the optical actuation of their cantilever to calibrate its stiffness. For this application the optical power that goes into the actuation has to be well known. To achieve this, a pure sine is needed. However to reach the maximum vibration amplitude, by a given maximum amplitude of the light source a square wave at the resonance frequency has the best performance. The Fourier series of a square wave has an amplitude of the first order [135]:

$$f_{\text{square}} = \frac{4}{\pi} \cos\left(\omega_0 t\right) + h.c. \tag{4.42}$$

The energy that goes into the system at the resonance frequency is about $\frac{4}{\pi} \approx 1.27$ times higher that that of a pure sine. The higher harmonics of the Fourier series have no correspondent vibration modes of the oscillator and do not lead to any further excitation of the system.
Unfortunately it is not possible to run the used laser source with a pure sine or a pure square wave signal. The PLL generates a sine wave, and the waveform of the laser source depends on the offset of the electrical signal as well as on the amplitude of the electrical signal. To optimize the oscillation amplitude, the oscillation is measured for a given parameter set and then the power spectrum is calculated. The frequency used for that measurement is set apart from the resonance frequency so that the amplitude does not depend on the frequency shift of the resonance frequency due to temperature variation. The value of the power spectrum at the actuation frequency is used as an optimization value – the higher it gets, the better the parameters are. A genetic algorithm performs the optimization steps. In this case, the fitness function makes a measurement. As most genetic algorithms search for a mathematically optimized parameter set, they store the global best result of the fitness function [114][147]. In this case, a real measurement is performed for that and a real measurement is influenced by many things, and it is possible to get a very good result by chance. Therefore the genetic algorithm for this optimization has to discard every result in each iteration of the algorithm and only uses mutated values. See chapter 3.8.3.2 for a description of the algorithm used.
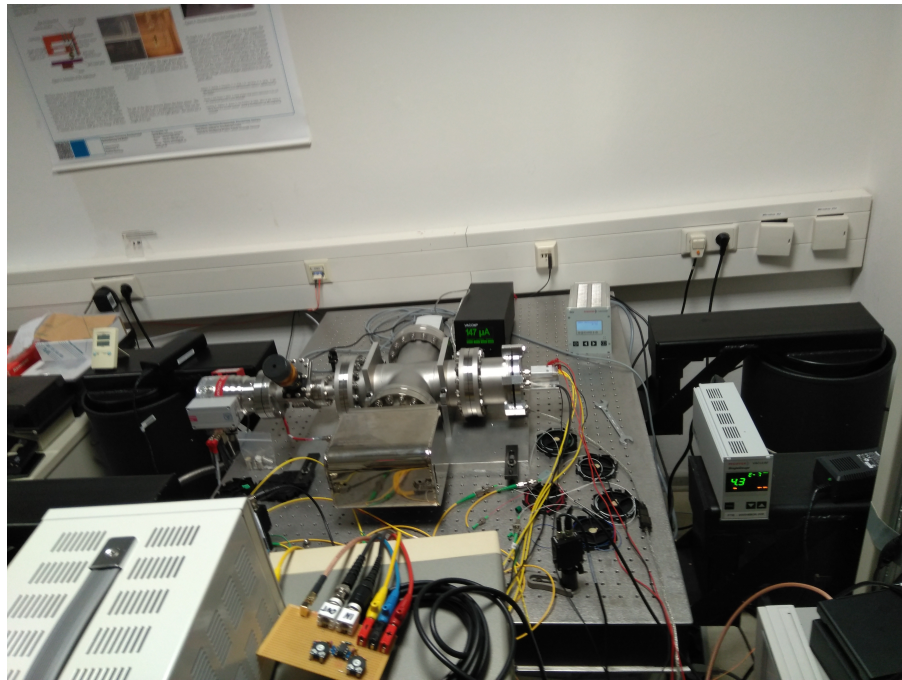
Figure 4.26: Photograph of the whole measurement setup. It shows the dampened optical table with the vacuum chamber on top. Also the Turbo pump, the ion pump and the optical fibers are shown. On the right of the vacuum chamber are the feedthroughs for the optical fibers and the electrical contacts. The experiment was placed inside of that flange.

4.9 Assembled Experiment

Fig. 4.27 shows a schematic of the complete setup and Fig. 4.26 shows a photograph of the optical table and the vacuum chamber on top. It consists of an air damped optical table. The vacuum chamber is attached on top of that table.
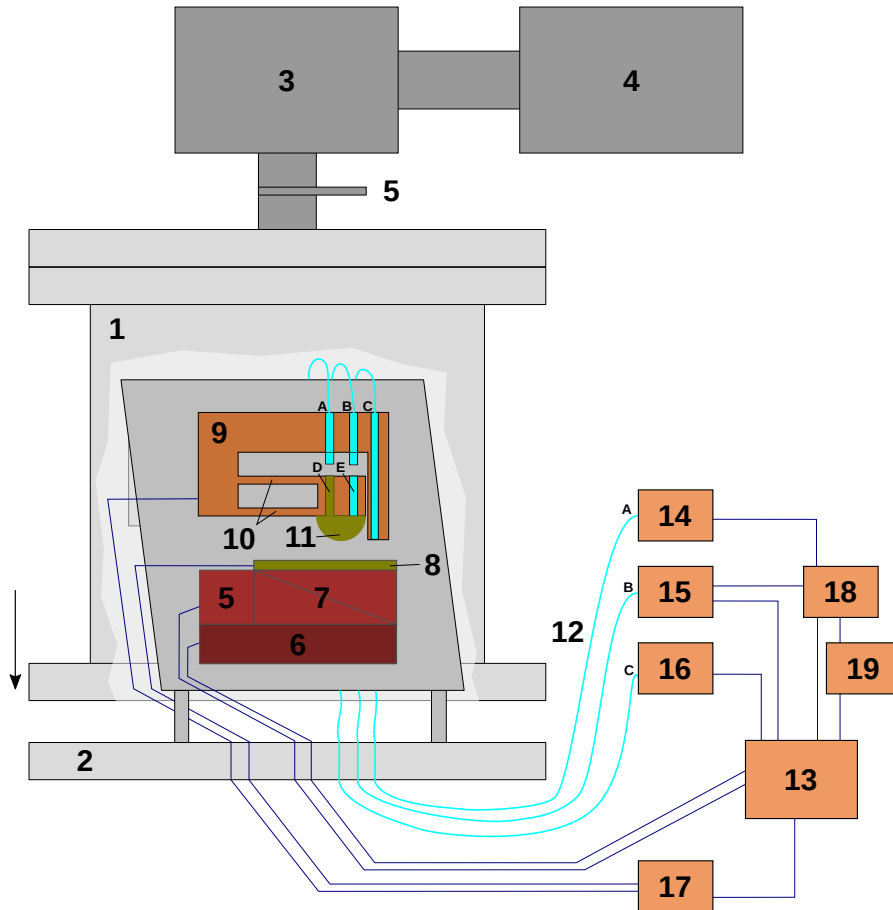
Figure 4.27: Schematic of the experimental setup. 1: vacuum chamber, 2: air damped platform, 3: turbopump, 4: rotary vane pump, 5: valve, 6: coarse positioner, 7: fine positioner, 8: gold coated silicon plate, 9: force sensor, 10: parallelogram flexure, 11: gold coated sphere, 12: optical fiber, 13: measurement computer, 14: actuating laser source, 15: fiber interferometer, 16: second fiber interferometer, 17: voltage source, 18: FPGA/PLL, 19: data accumulation, D: gold coated fiber for optical actuation, F: mirror fiber for vibration measurement.
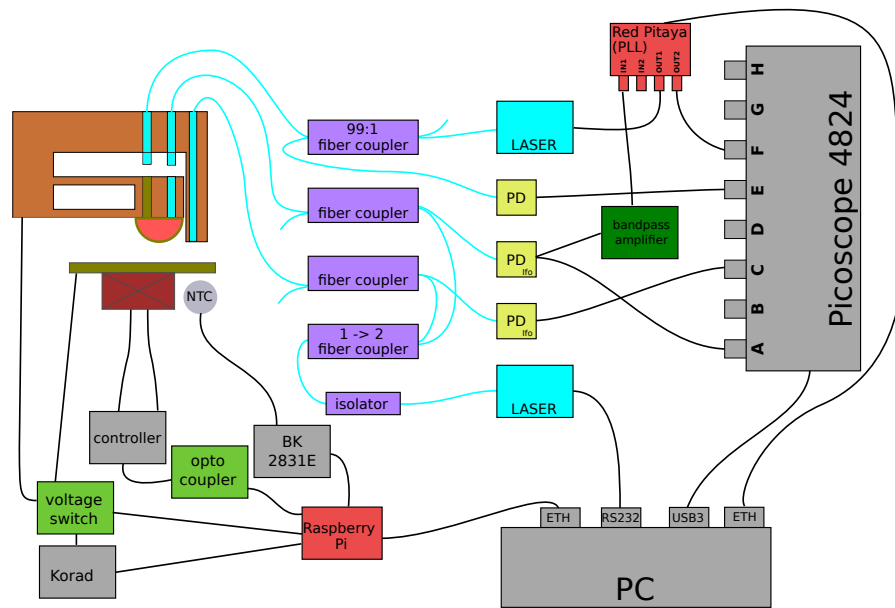
Figure 4.28: Schematic of the signals in the experimental setup.

4.9.1 Signals

Fig. 4.28 shows the details of the fiber connections as well as the electronic signals. The Omicron controller drives the piezo-slides, the Agilent 8164B laser is connected to the computer via an RS232 interface. The computer sets the wavelength of the laser. The computer is connected via Ethernet to a Raspberry Pi. The Pi is connected to a Korad voltage source, and a voltage switch that is also connected to the Korad. The voltage switch is electrically connected to the force sensor and the gold coating of the ruby half-sphere. On the other end the voltage switch is connected to the gold coated plate. The Raspberry Pi is further connected via GPIOs to the opto-coupler board from Fig. 4.13. The opto-coupler board drives the controller which drives the piezo slides. Furthermore the Raspberry Pi is connected to a BK Precision 2831E digital multimeter to measure the resistance of the NTC-sensor placed on the base plate of the experiment behind the glass block of the force sensor. The Agilent laser is connected via an optical fiber to an optical isolator, afterwards a one to two fiber coupler is used to get the signals for both interferometers. The first interferometer is connected to a 90/10 fiber coupler, one end of it is dumped, the other end is glued on the force sensor and placed as the distance interferometer in front of the gold coated plate. The fiber couplers fourth end with the interferometer signal is measured with a photodiode which is read out using the Picoscope. The other fiber of the one to two fiber coupler is also connected to a 90/10 fiber coupler that is connected to the force sensor and builds the vibration interferometer. The output fiber of the interferometer is connected to a photodiode. In this case the signal goes to the Picoscope as well as to a bandpass amplifier that is connected to an input of the Red Pitaya. The connection to the Picoscope is used to measure the absolute cavity length to set the optimum wavelength. The Red Pitaya uses the input signal for the PLL. A reference output of the
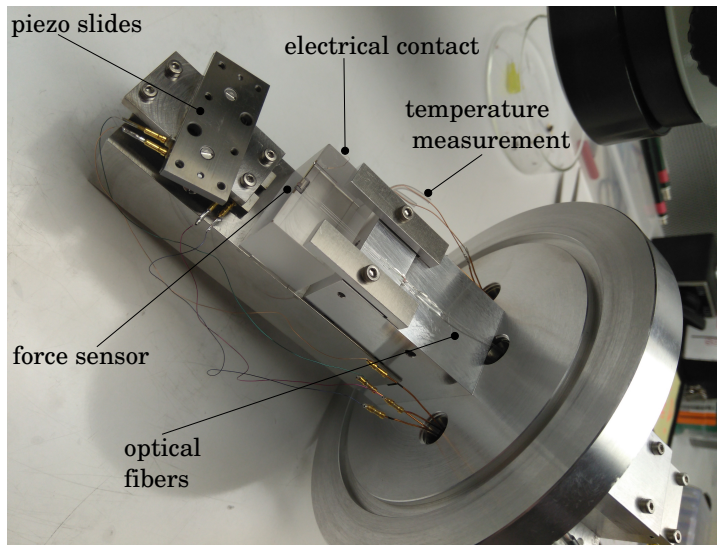
87

Figure 4.29: The photograph shows the assembled experiment inside the vacuum chamber.

Red Pitaya is connected to the Picoscope. The first output of the Red Pitaya is connected to the red fiber laser. The fiber of this laser goes into a 99:1 fiber coupler. The 1% output goes to a photodiode to measure the waveform of the laser with the Picoscope. The 99% output of the fiber coupler is connected to the force sensor for the optical actuation. The Red Pitaya is connected via Ethernet to the computer, and the computer reads out the PLL state this way. The Picoscope is connected via USB3 to the computer.

4.9.2 Assembled Experiment Inside the Vacuum Chamber

Fig. 4.29 shows the inside of the vacuum chamber. The coated plate is shown attached to the piezo slides in Fig. 4.30. On the left are the two angled piezo drives. In front of them is the glass block with the force sensor attached. From the force sensor on are the three optical fibers. The glass block is clamped onto the base plate. The NTC sensor was positioned on top of the base plate between the glass and aluminum blocks.
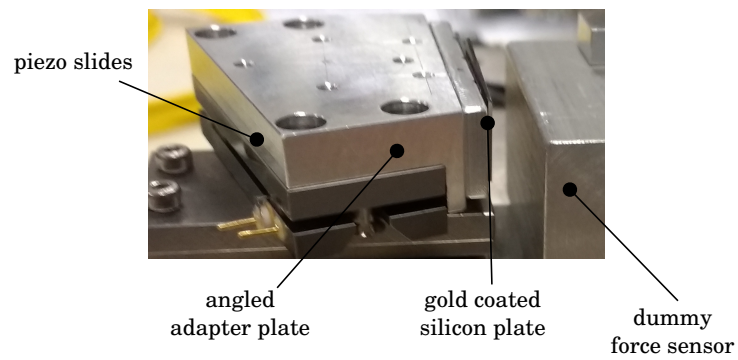
Figure 4.30: This photograph shows the interior of the vacuum chamber with a dummy glass block. The gold coated plate is attached to a connecting plate that is attached to the piezo slides.

Chapter 5

Experiments and Data Analysis

5.1 General Overview

The following subchapters describe different experimental runs. Between those runs the force sensor was changed and there were also changes in other factors of the experiments. Those are described in the corresponding subchapter.

Each measurement consisted of different steps. First the quality factor Q and the resonance frequency f_{res} were measured. Afterwards the optimal wavelength of the Agilent laser for the vibration measurement was obtained. The next step was to drive the plate near the sphere and measure the distance offset for the distance interferometer. The last step was to measure distance-frequency curves. Additionally the surfaces of the sphere and the plate were measured for the measurement runs in summer 2017 and winter 2018.

5.1.1 Distance Measurement between Sphere and Plate

To measure the distance between the sphere and the plate, two methods are implemented. On the side of the force sensor (16/C in Fig. 4.27) is an additional fiber that has been built together with the plate a fiber interferometer. The interferometer can be used to measure each step of the moving plate. With this interferometer it is possible to measure the distance change during the measurement. The fibers were placed in parallel v-grooves to minimize possible errors in distance measurement due to an unexpected angle between interferometer beam and the tangent plane of the sphere. A less than 2° angle error means only 1 nm length error for a 1 μm range, which is smaller than other influences in the current experiment[1]. To get the absolute value of the distance between the half-sphere and the plate in the first place, an electrostatic method is used.

According to Eq. (3.124) from chapter 3.4, the force between the sphere and the plate can be changed by applying a voltage between them. Applying different voltages between $-10\,\mathrm{V}$ and $+10\,\mathrm{V}$ and measuring the force allows us to fit the distance d and the contact potential difference V_m.

---

[1] $\frac{d}{\cos(\alpha)} = d_\alpha$, with α as angle alignment error and d_α as the real distance.

With this it is possible to obtain the distance offset of the interferometer. The distance offset of the interferometer is defined by:

$$d_{\text{offset}} = d_{\text{int}} - d \tag{5.1}$$

d_{int} is the distance of the fiber to the plate measured using the interferometer. Because of Eq. (3.124) the applied voltage produces a force. This force can be combined with Eq. (3.164) to give the frequency shift due to the applied voltage:

$$
\begin{aligned}
\frac{\Delta\omega}{\omega_{res}} &= -\frac{1}{\pi a k} \int_{-1}^{1} \pi\epsilon_0 R \frac{(V - V_m)^2}{d + a(1 + u)} \frac{u}{\sqrt{1 - u^2}} \mathrm{d}u \tag{5.2} \\
&= -\frac{\epsilon_0 R (V - V_m)^2}{a k} \int_{-1}^{1} \frac{1}{d + a(1 + u)} \frac{u}{\sqrt{1 - u^2}} \mathrm{d}u \tag{5.3}
\end{aligned}
$$

k is the spring constant of the force sensor, ω_{res} is the resonance frequency of that cantilever, $\Delta\omega$ is the frequency shift and a is the amplitude of the oscillating cantilever. V is the applied voltage, V_m is the contact potential difference and R the radius of the sphere. While the frequency f_{meas} as well as a are the measured entities, the other free parameters can be fitted. Combining the measured frequency with the resonance frequency to get the frequency shift:

$$\frac{\Delta\omega}{\omega_{\text{res}}} = \frac{|f_{\text{res}} - f_{\text{meas}}|}{f_{\text{res}}} \tag{5.4}$$

The fitting parameters are V_m, d and f_{res}. To fit these parameters, a numerical integration as well as a fitting method is needed. For the numerical integration, the $QUADPACK$ library [110] is used. For the fit, the optimization method of differential evolution by Storn et al. [114] is used. Additionally, the frequency shift of different voltages was measured at multiple distances, not at just one distance.

5.1.2 Temperature Dependence of the Resonance Frequency

Section 4.1.1 described that the frequency of the force sensor is temperature dependent and that simulations were performed using Young's modulus from section 3.5.3. The simulation result was $1.052\,\text{Hz/K}$ as was shown in Table 4.1. In Fig. 5.1, the measured temperature as well as the measured frequency are shown. The frequency change has about 12 minutes delay compared to the temperature change at the NTC sensor. A linear regression gives a factor of $0.9888\,\frac{\text{Hz}}{\text{K}}$ which is only a $6\,\%$ variation from the simulated value.

5.2 Preparations of the Experiments in 2016

Before the first experimental runs were started, the experiment was built and first measurements were done to learn how the system behaves and what was needed for the first experiments.
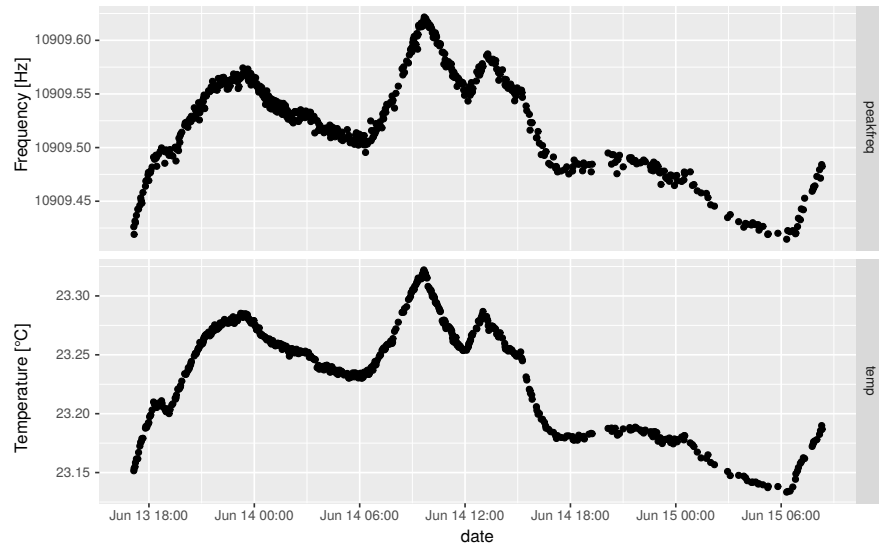The first assembled force sensor is shown in Fig. 5.2.

Figure 5.1: The plot shows the measured frequency and the measured temperature during a whole day. It's clear that both are linearly correlated. The temperature sensor is placed between the oscillator and the vacuum flange, therefore every change in temperature from outside hits the temperature sensor before it hits the oscillator. This leads to about 12 minutes delay between the frequency change and the measured temperature.
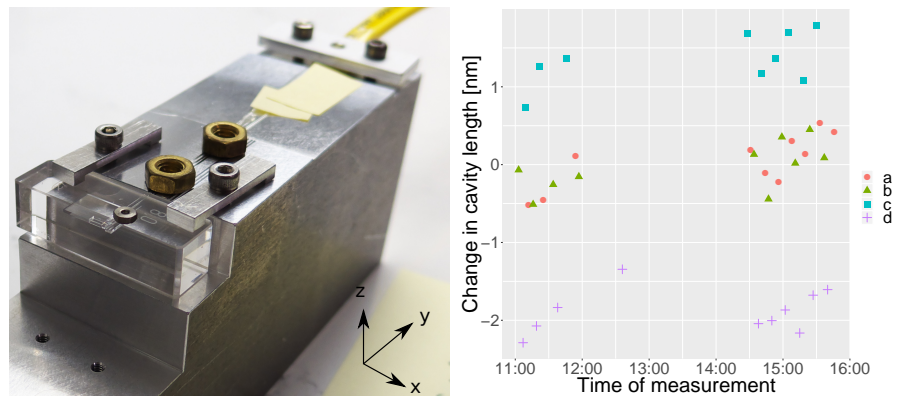

Figure 5.2: On the left a photograph shows the first sensor assembled on a gauge block. The plot on the right shows the cavity length of the vibration measurement interferometer depending on the rotation of the whole force sensor. a is the orientation of the image, b is upside down, c is a 90° rotation around x aka standing vertically d is a $-90°$ rotation around the x aka downward facing. The zero level of the cavity length is 22370.0 nm.
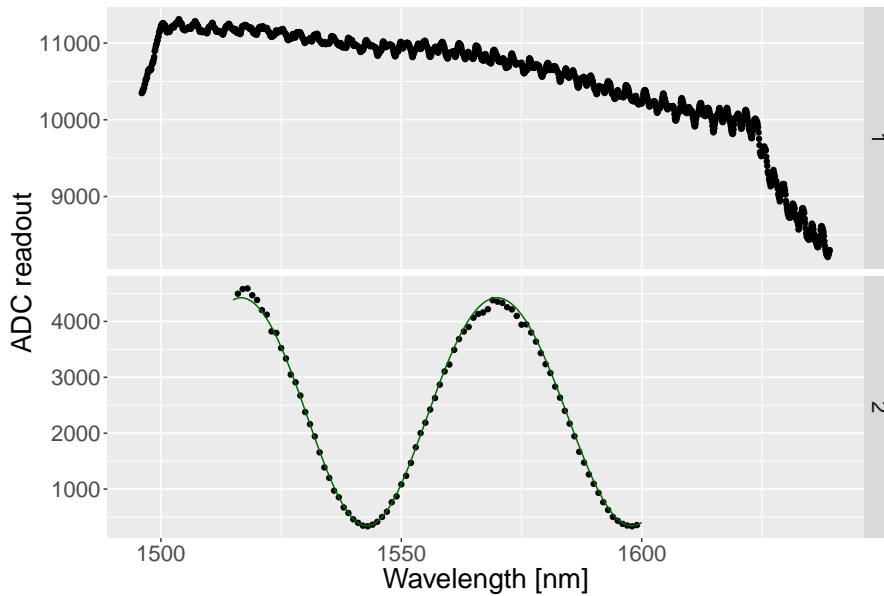
Figure 5.3: On the upper plot, the Agilent 8164B laser power was measured against a photodiode. The result is almost flat between 1500 nm and 1600 nm, but it has a steep slope below 1500 nm and above 1620 nm. The lower plot shows the first Fabry-Pérot measurement as dots, and the fit as an unbroken line.

5.2.1 Fabry-Pérot Measurement

The laser source is the Agilent 8164B. It is a tunable laser with a range of 1490 nm to 1640 nm. The absolute wavelength accuracy was calibrated to about 1 pm over the whole wavelength range with a repeatability of less than 0.2 pm. The power flatness of the used *low SSE* output is less than 0.05 dB across the complete wavelength range, and the power stability over time is less than 0.0005 dB over an hour[2].

First of all, the laser beam, that was supposed to go into the Fabry-Pérot was measured on a photodiode PDA 10CS from Thorlabs directly after the end of the fiber. The result is shown in Fig. 5.3.

As result of the measurement a wavelength range that spanned from 1515 nm to 1600 nm was chosen for the Fabry-Pérot measurements. In that wavelength range both fiber couplers and both interferometers have the best transmission. The Fabry-Pérot analysis is performed using Eq. (4.11). The lower plot in Fig. 5.3 shows one of the first Fabry-Pérot measurements. The result of the Fabry-Pérot measurement is the length of the cavity. This length was measured under different conditions as shown in Fig. 5.2. The two horizontal measurement positions have nearly the same cavity length (*a, b*). But if it is measured perpendicularly, as shown by *c* in Fig. 5.2, the cavity length increases due to gravity. In case of the inverse perpendicular

---

[2]see calibration report

case *d*, the cavity length decreases due to gravity:

$$\Delta L_a = 0.04(\pm 0.11)\,\text{nm} \tag{5.5}$$
$$\Delta L_b = -0.04(\pm 0.10)\,\text{nm} \tag{5.6}$$
$$\Delta L_c = 1.35(\pm 0.11)\,\text{nm} \tag{5.7}$$
$$\Delta L_d = -1.89(\pm 0.09)\,\text{nm} \tag{5.8}$$

After measuring the cavity length of the interferometer, the wavelength of the laser is set to the value where the interferometer can take the most sensitive readings. See Eq. (4.12) for that calculation. With a cavity length of $L = 22370\,\text{nm}$ this means that the laser was adjusted to $\lambda = 1529.6\,\text{nm}$ for further measurements.

5.2.2 Resonance Frequency using a Ringdown Experiment

The resonance frequency can be calculated using a FEM simulation. Parameters such as the exact position of the sphere have an influence on the resonance frequency. Therefore it is necessary to measure the resonance frequency before optimizing the PLL parameters. To measure the resonance frequency, a ringdown experiment is performed. For this experiment, a wrench is knocked against the vacuum chamber. This causes to a high amplitude of the force sensor at its resonance frequency of the first vibration mode. The decay of the vibration is measured and fit to the resonance frequency and the quality factor Q.

$$ADC = O + A \cdot \text{e}^{-\frac{\omega_0 t}{2Q}} \cdot \cos\left(\omega_0 t + \phi\right) \tag{5.9}$$

ADC is the read-out value of the ADC, O is the read-out offset and A is the read-out amplitude. ω_0 is the resonance frequency, t is the time and ϕ is the phase offset. The ringdown experiments shown in Fig. 5.4 characterize the force sensor to a frequency of 12959 Hz and a quality factor of $Q = 499$.

5.2.3 Putting the Force Sensor into the Vacuum Chamber

After finishing the first tests under air conditions, the force sensor was put into the vacuum chamber. Since the optical fibers need a feedthrough, they were removed from the force sensor. Afterwards they were put through the feed-through and then reattached to the force sensor. The description of the feedthrough can be found in section 4.2.1. At a pressure of about 10^{-6} mbar, the quality factor Q was measured again using a ringdown experiment.

5.2.4 Resonance Frequency with a Resonance Curve

After measuring the resonance frequency and the quality factor for the bare force sensor, a gold sphere was glued onto the force sensor. The gold sphere is shown at the left of Fig. 5.6. A ringdown experiment showed the change of the resonance frequency. A higher mass attached to the spring leads to a smaller resonance frequency. Most notably, the quality factor increased by a factor of 10. This led us to the false conclusion that the quality factor can be
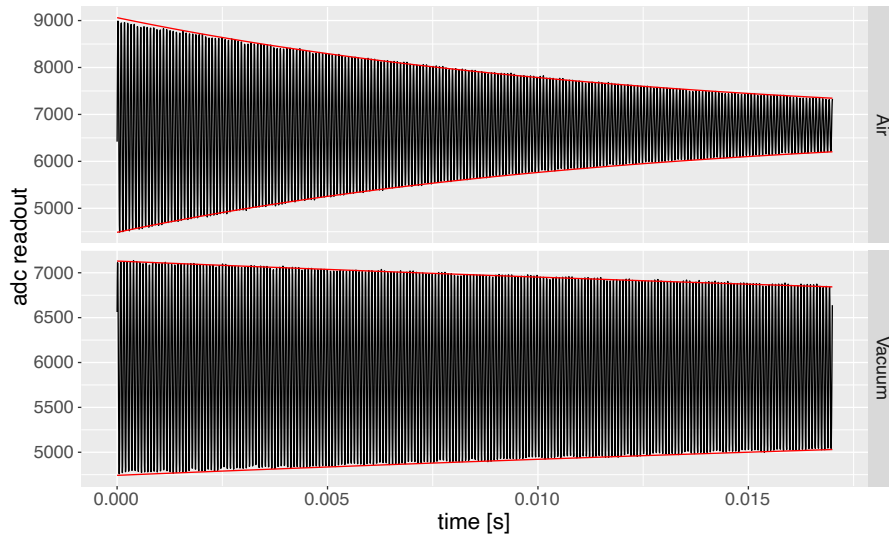
Figure 5.4: Ringdown of the force sensor. The first ringdown of the force sensor was measured under air pressure with a resonance frequency $f_0 = 12959$ Hz and a quality factor $Q = 499$. The second ringdown of the same force sensor was measured in vacuum. The fibers were reglued before bringing the sensor into the vacuum, which led to a small shift in the resonance frequency $f_0 = 13242$ Hz. The new quality factor was $Q = 2564$.
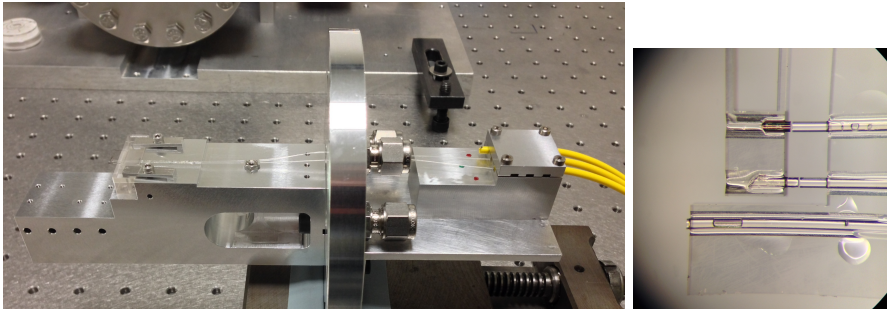

Figure 5.5: The left image shows the flange with the fiber feedthrough and the attached force sensor. The right part of that image shows the strain relief of the optical fibers. The right image shows the newly glued fibers on the force sensor.
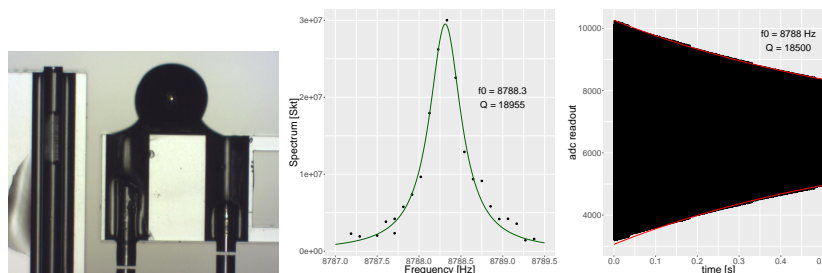
Figure 5.6: Ringdown of the force sensor and its resonance curve after a gold sphere (left) was glued to the force sensor.

increased with a higher mass attached to the force sensor. It is much more likely that the glue caused this change, rather than the material loss.
The next step was to test the optical actuation. For that purpose, a resonance curve was measured. This is also another method to measure the resonance frequency and the quality factor. A function generator is set to specific frequencies, the function generator drives a laser, and the amplitude modulated laser light drives the force sensor.
Two different methods to measure the resonance curve were used. The first method is to directly measuring the voltage of the photodiode with a certain sampling rate. The power spectral density of the measured signal was calculated and the value at the set frequency was taken. These were performed for each of the set frequencies and the result is the resonance curve. The other method is measuring the amplitude with the SR 830 lock-in amplifier as described in section 4.7. The lock-in amplifier takes the set frequency as input signal as well as the photodiode voltage. As output the lock-in calculates the amplitude and the phase of the signal. The resulting amplitude signal is a measurement for the root mean squared voltage V_{rms}. With a correction factor for the voltage that can be set at the lock-in amplifier, V_{rms} is given through the output voltage. To calculate the Cauchy-Lorentz distribution parameter from the lock-in measurement, the signal is squared to be comparable with the data based on the power spectral density method.

5.2.5 Conclusions after the First Measurements

During 2016, a lot of tests were performed and the measurement routine was optimized. The air conditioner of the laboratory did not work properly, and on some days the temperature changed by more than $1\,^\circ\mathrm{C}$. After adding the piezo slides, the controller had issues. For example the step size was far from equidistant. We tried a newer model of the controller, but that one enforced a minimum step size that was too large for the experiment. So we created a new computer controlled interface for the old piezo slide controller using a Raspberry Pi mini computer. Also the PLL was implemented during this period. We tried to measure the absolute distance between the sphere and the plate using different applied voltages between them, but we were unable to measure any frequency change. We later concluded that the gold sphere was not in electrical contact with the gold coating on the force sensor. This means a layer of glue was between them and isolated the contact. Our solid

gold spheres with $d = 0.5\,\text{mm}$ had a high mass, but a bad surface shape. So we chose to change from solid gold to ruby spheres with $d = 1\,\text{mm}$. The ruby sphere was milled to a half-sphere. After gluing the ruby half-sphere to the force sensor, a gold coating was applied. This also enabled us to guarantee an electrical contact of the half-sphere to the measurement system.
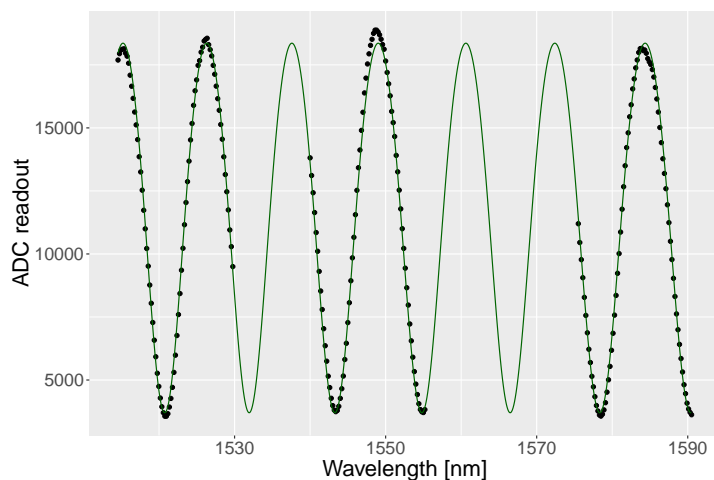
Figure 5.7: Distance measurement using a Fabry-Pérot cavity. The fitted cavity length is $L = (1.041716 \cdot 10^{-4} \pm 4.95 \cdot 10^{-10})$ m.

5.3 Measurements between January 2017 and March 2017

A new force sensor with a higher Q and a gold coated ruby half-sphere was assembled in January 2017.

$$
\begin{aligned}
Q &= (1.820 \pm 0.5) \times 10^4 & (5.10) \\
f_0 &= 9829.13\,\text{Hz} & (5.11)
\end{aligned}
$$

5.3.1 Distance Measurement

The experimental setup consists of two Fabry-Pérot cavities. While the first is used for the vibration measurement, the second is used to measure the distance of the force sensor to the sphere. The distance measurement is done in the same way as the measurement of the first Fabry-Pérot cavity. The wavelength of the laser is shifted and the reflected light in the glass fiber is measured. After fitting this, the distance of the end of the fiber and the gold plate was obtained. Unfortunately, the end of the fiber does not have the same distance as the sphere to the plate. The fiber has to have a larger distance from the plate than the sphere. Before using the Fabry-Pérot cavity to measure the current distance between the half-sphere and the plate, the distance offset has to be obtained.

Section 5.1.1 describes how the distance offset is measured. The frequency shift is parabolic as is the electrostatic force. To get a realistic V_m it would be necessary to use a voltage range from $-V_\text{max}$ to $+V_\text{max}$. With the Korad DC Power Supply it was only possible to set voltages in the $[0\,\text{V}, 30\,\text{V}]$ range. Fig. 5.8 shows the results of the distance measurement. The distance measurement has very high uncertainty levels. Part of the explanation could be that the measurements were done using the resonance curve method.

After the distance calibration on Feb. 9th 2017 the phase locked loop (PLL) was optimized as described in section 4.6.
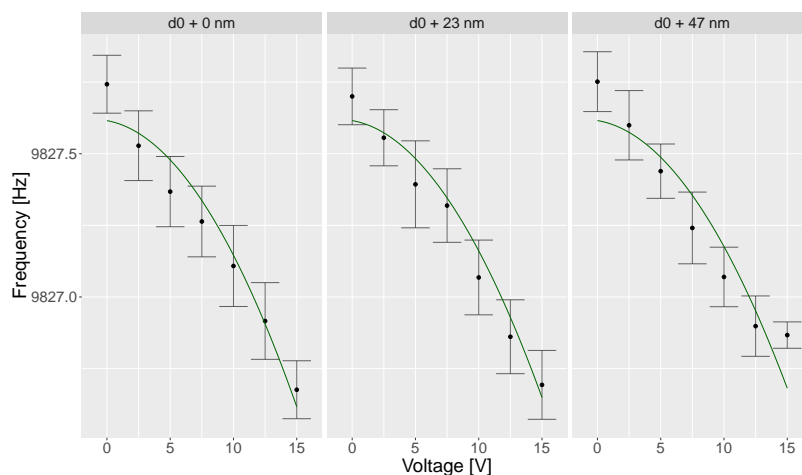
Figure 5.8: Distance offset measurement. The fitted parameters were $d_0 = (1.384 \pm 0.031)$ μm, $V_0 = -1.000$ V, $f_0 = (9827.62 \pm 0.01)$ Hz, $k = (9.09 \pm 0.36)$ kN m^{-1}. This d_0 means, that the distance offset would be $d_O = (102.764 \pm 0.031)$ μm.

On Feb. 28th 2017 a distance frequency curve was measured using the PLL to measure the frequency. The result is shown in Fig. 5.9.
The fitted patch effect voltage of $V_{rms} = (6.07 \pm 0.54)$ V is very high. This could mean, that the electrical connection of the sphere was quite bad or that there were parasitic voltages at the electrodes.

5.3.2 Lessons Learned from the First Experimental Run

After measuring the first frequency shifts due to the electrostatic force and also after measuring the first distance-frequency curve, we came to a couple of conclusions for the next experimental run.
Fig. 5.8 showed that the applied voltage between the half-sphere and the plate was always positive, because the voltage source was only able to provide that. Afterwards we implemented a voltage switch, as described in section 4.9.1, that was able to invert the voltage applied to the sphere and the plate by just inverting the electrical connections. Also, especially after changing the voltage back from $+30$ V to 0 V, the system responded only with delay to the voltage change with its frequency. So a waiting delay after applying a different voltage was added for the next experiments. Also in the first experimental run, we had not yet added a temperature sensor inside the vacuum chamber and were not able to correct the measured frequency by the measured temperature. This was also changed before the next experimental run. When fitting the distance offset, the fitted absolute distance d_0 and the fitted stiffness k were highly correlated with a Pearson correlation coefficient of -0.86. This means it is necessary to independently measure the stiffness of the force sensor.
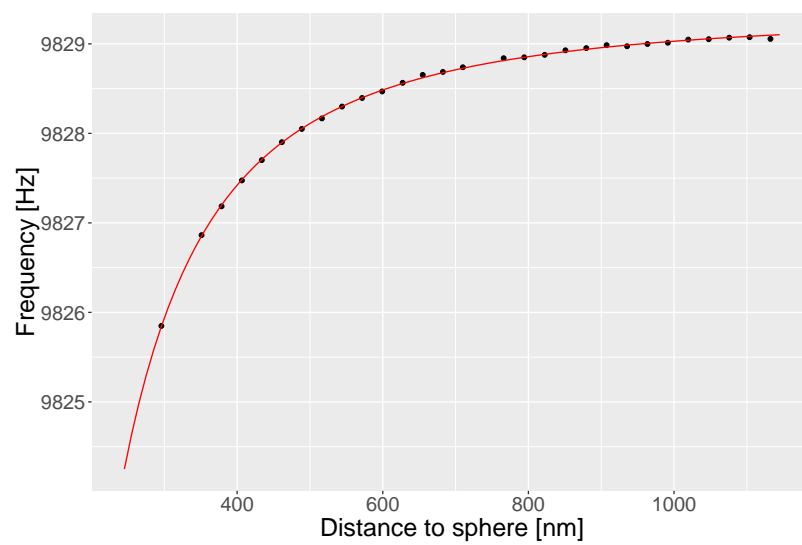
Figure 5.9: Distance frequency curve measurement from Feb. 28th in 2017. The dots are measurements taken during the experiment, the solid line is the fit function. The fit parameters were $f_0 = 9829.34\,\text{Hz}$ and $V_{rms} = (6.07 \pm 0.54)\,\text{V}$.

5.4 Measuring the Stiffness of the Force Sensor

After all measurements were concluded, the force sensor used in the experiments of summer 2017 and winter 2017/2018 were analyzed. During fitting of the force measurement results, the stiffness and the distance are correlated. To overcome this, the result of the stiffness measurement is needed to better analyze the force measurement. The stiffness measurement was performed by Uwe Brand in summer 2018. The force was measured with a compensation balance and a 1D positioner (PIFoc) with $100\,\mu$m travel. It was used to deflect the parallelogram flexure by $5\,\mu$m [148][149]. The result of the stiffness measurement is shown in Fig. 5.10.

$$
\begin{aligned}
k_{S17,load} &= (7703.34 \pm 0.14)\ \text{N/m} & (5.12)\\
k_{S17,unload} &= (7723.61 \pm 0.15)\ \text{N/m} & (5.13)\\
k_{W18,load} &= (6114.62 \pm 0.24)\ \text{N/m} & (5.14)\\
k_{W18,unload} &= (6122.87 \pm 0.24)\ \text{N/m} & (5.15)
\end{aligned}
$$

It is obvious, that the stiffness for loading and unloading is different. For the force sensor used between April 2017 and August 2017 the difference was larger than it was for the force sensor used from September 2017 until February 2018. A possible explanation for the difference in stiffness for loading and unloading the parallelogram flexure is the glue that was used to glue the ruby half-sphere to the parallelogram flexure.
The temperature dependence of the stiffness was not explicitly measured. But for the force sensor used in the next subchapter, the stiffness measurement for a total deflection of $10\,\mu$m was done twice, with different temperatures. The measurement result is shown in Fig. 5.11.

$$
\begin{aligned}
k_{load,22.50\,°C} &= (7682.66 \pm 0.59)\ \text{N/m} & (5.16)\\
k_{load,22.60\,°C} &= (7675.41 \pm 0.20)\ \text{N/m} & (5.17)\\
k_{unload,22.50\,°C} &= (7700.28 \pm 0.60)\ \text{N/m} & (5.18)\\
k_{unload,22.60\,°C} &= (7690.08 \pm 0.22)\ \text{N/m} & (5.19)
\end{aligned}
$$

Assuming a linear temperature dependence of the stiffness, it is:

$$
\begin{aligned}
\Delta k_{load} &= (-73 \pm 6)\ \text{N/mK} & (5.20)\\
\Delta k_{unload} &= (-102 \pm 6)\ \text{N/mK} & (5.21)
\end{aligned}
$$

The large difference of temperature dependence between loading and unloading suggests that at least part of the temperature dependence comes from the same reason as the difference of the stiffness when loading and unloading. The temperature dependence of k was not measured for the force sensor used in the last measurements taken after September 2017. Also the result of the stiffness measurement at $10\,\mu$m deflection of the force sensor differs from the stiffness measured at $5\,\mu$m deflection. Since the vibration amplitude is much smaller than the deflection during the stiffness measurement, the result for the $5\,\mu$m deflection is used in the further analysis.
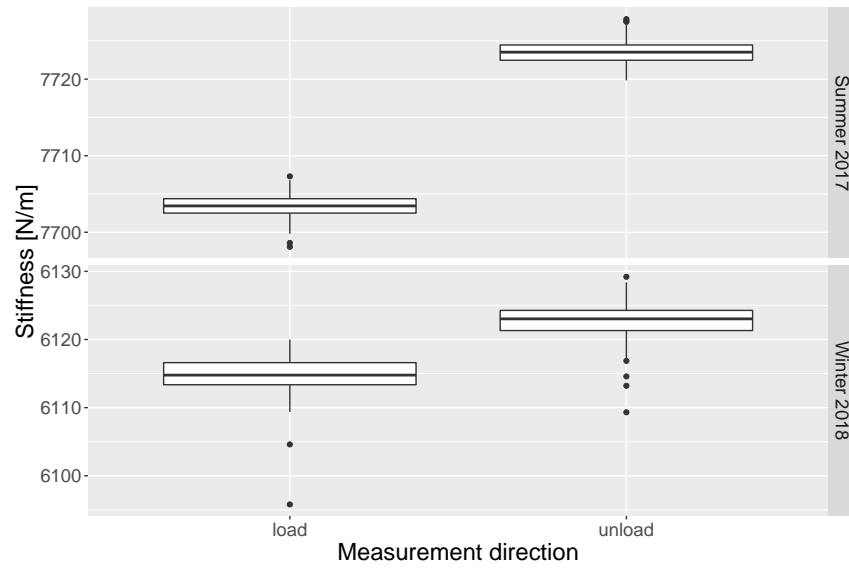
Figure 5.10: Stiffness measurement of the two force sensors used in the last two experimental runs. On the left is the stiffness when a force is applied until the force sensor deflects 5 μm and, on the right is the stiffness when the force is unloaded from the force sensor. The ambient temperature during the measurement of the Summer 2017 parallelogram flexure was 22.50 °C and for the Winter 2018 parallelogram cantilever it was 22.70 °C.
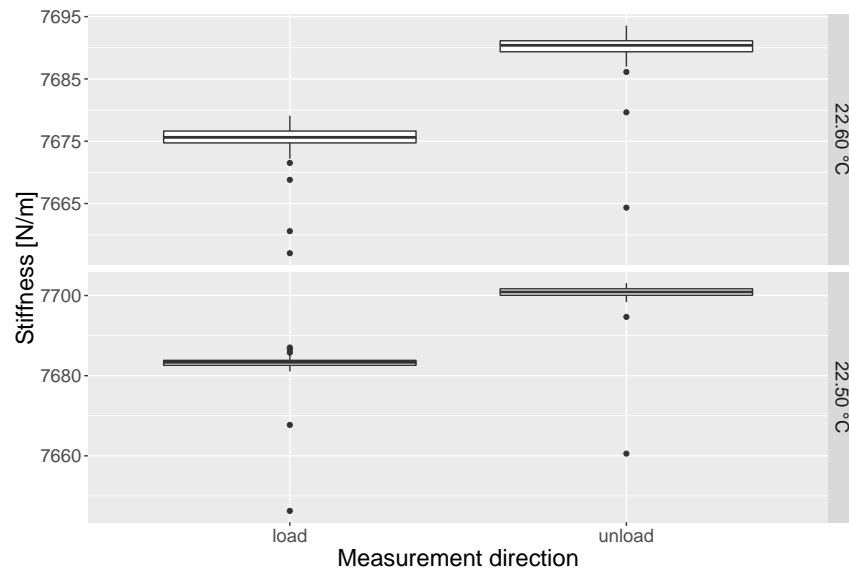

Figure 5.11: Temperature dependence of the force sensor stiffness.

The stiffness used for the data analysis of the experiments is the mean of the first measurement:

$$k_{S17} = 7713\,\text{N/m} \tag{5.22}$$
$$k_{W18} = 6619\,\text{N/m} \tag{5.23}$$

Due to the different stiffness values on loading and on unloading, the uncertainty of k_{S17} and k_{W18} was not obtained. One could argue to use the difference between both stiffnesses as uncertainty.
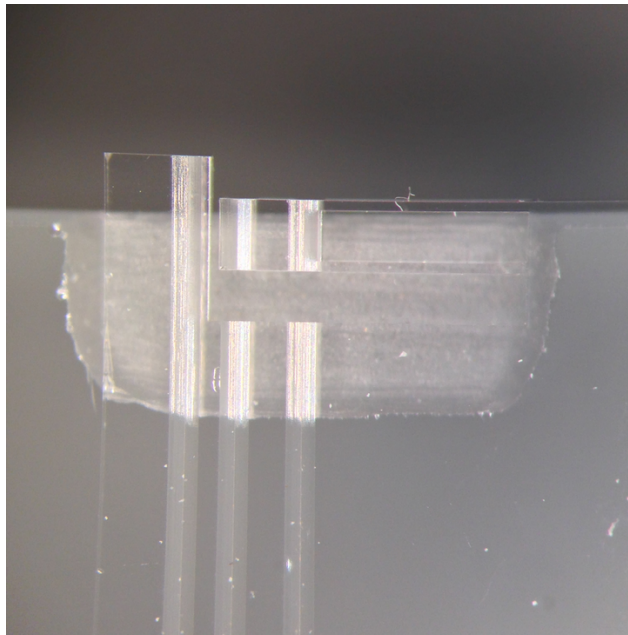
Figure 5.12: A new force sensor was prepared. It was placed on a glass block with a milled hole right below the moving part of the force sensor. The idea of this method was, that the energy loss would be lower with the glass plate attached to the glass block on the right of the force sensor.

5.5 Measurements between April and August 2017

5.5.1 Preparation of the Experiment

A new force sensor was built and attached over a hole in the glass plate to increase the quality factor as seen in Fig. 5.12. A force sensor without anything else attached with rounded edges inside the parallelogram flexure had a quality factor of about 125000. A new ruby half-sphere with $R = 0.5\,\mathrm{mm}$ was attached to the sensor. Both were then coated with a $200\,\mathrm{nm}$ thick layer of gold. A new plate was cut out of a silicon wafer and this was also coated with a $200\,\mathrm{nm}$ thick layer of gold. After attaching everything to the new force sensor, the new quality factor was around 35000. The new resonance frequency was about $10.9\,\mathrm{kHz}$.
Before starting this experiment we added a $10\,\mathrm{k\Omega}$-NTC sensor to measure the temperature.

5.5.1.1 Distance Calibration

The distance calibration was performed similarly to how the distance measurement was performed in the previous experiment. The results of the distance calibration are shown in Fig. 5.13.
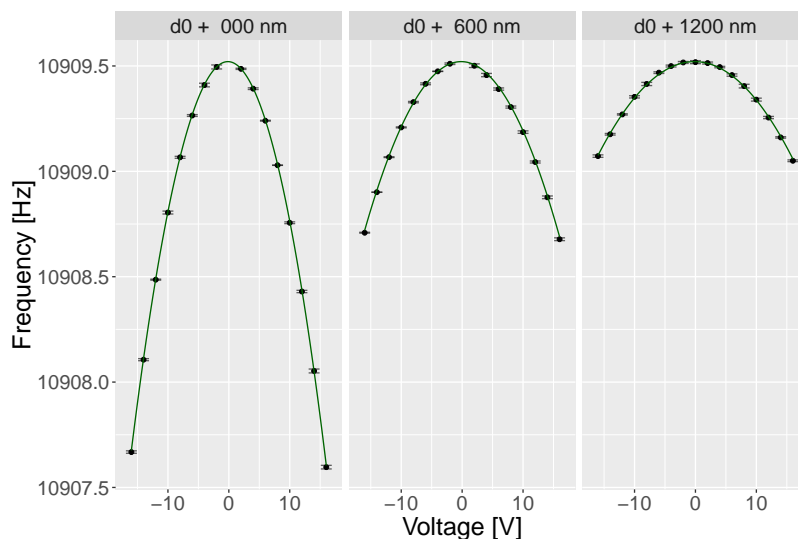
5.5.1.2 Measurement 2017-08-11

Figure 5.13: $d_0 = (1.1575 \pm 0.0005)\,\mu$m which means that the offset of the distance Fabry-Pérot cavity is $96.404\,\mu$m. $V_m = (-152 \pm 4)$ mV and $f_0 = 10909.52$ Hz.

After the preparations with the new force sensor were done, we performed a measurement of the distance-frequency curve on August 11th.

For each step approaching the force sensor with the plate, the distance is measured by using the wavelength sweep of the Fabry-Pérot interferometer. Since both Fabry-Pérot cavities are powered by the same laser source, the cavity length is measured for both cavities simultaneously. The vibration measurement cavity has a constant length, when averaging the vibration. If the detected cavity length changes after a step of the plate, this means that the force sensor was moved by the moving plate, which indicates a collision. After a detected collision, the plate is moved away from the sphere. The measurement routine was programmed to stop the measurement when the distance is below 30 nm. Unfortunately, the collision detection was always triggered first. The measurement from Aug. 11th is seen in Fig. 5.14. It was performed at an applied voltage of 2 V between the half-sphere and the plate. The idea of using an applied voltage was to make sure that the measurement routine works as expected and the measurement can be done in principle. Unfortunately 441 nm was the closest approach possible. At this distance, the Casimir effect would change the resonance frequency by $73\,\mu$Hz, which was out of reach of the PLL. For a frequency change of 1 mHz a distance of 230 nm would be needed and for a frequency change of 10 mHz a distance of 128 nm would be needed. As seen in Fig. 5.14 this would easily detectable with the measurement setup used in this experiment.

5.5.2 Analyzing the Sphere Surface after the Experiment

After disassembling the experiment in September 2017, the force sensor was placed under a LeXT laser scanning microscope. The goal was to measure the
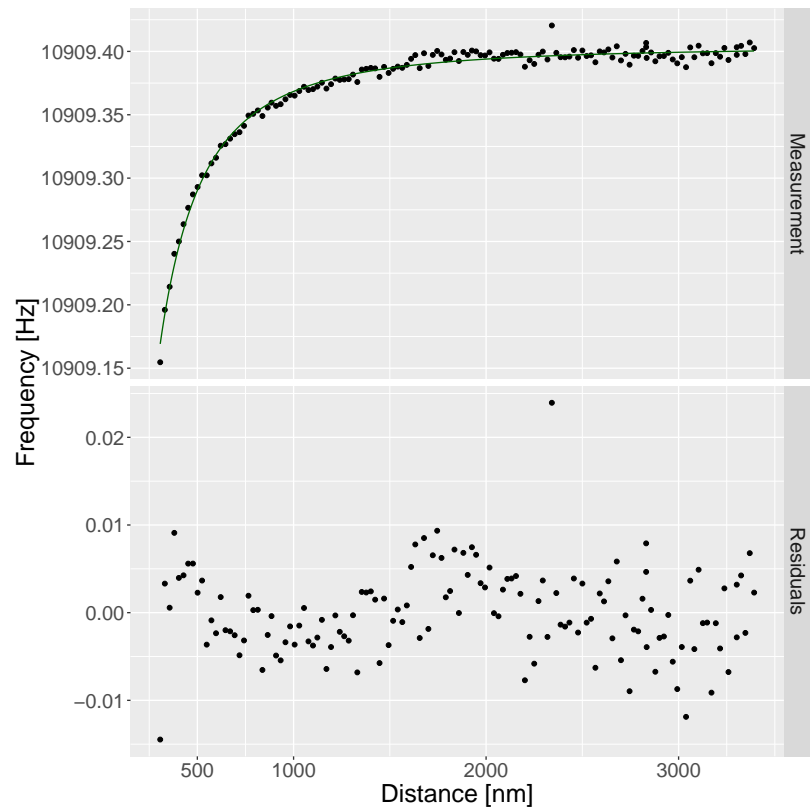
Figure 5.14: Measurement from Aug. 11, 2017. A voltage of 2 V was applied between the half-sphere and the plate. The measurement stopped because of a detected collision. This may have been the result of a particle on the half-sphere or the plate.
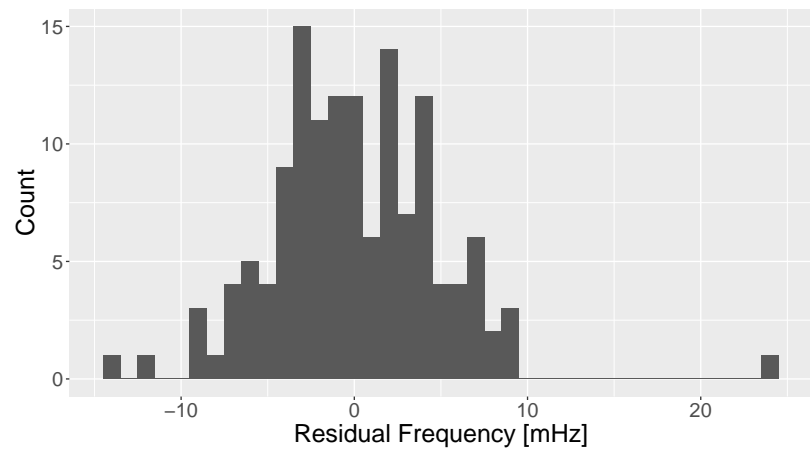

Figure 5.15: Histogram of the residuals of the measurement from Aug. 11, 2017. The binwidth is 1 mHz.
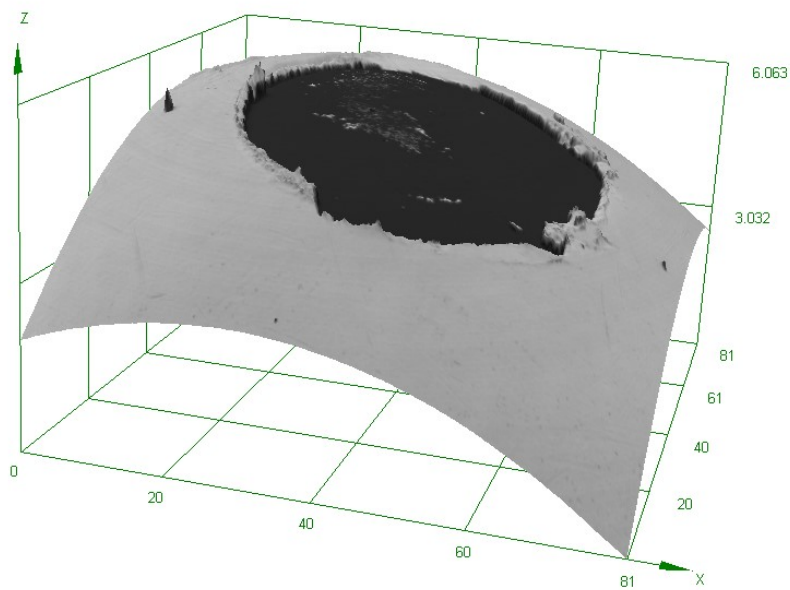
Figure 5.16: The gold sphere used for the experiments in this chapter. The image was taken using a LeXT laser scanning microscope. It is obvious that on top of the surface the height of the sphere is different from the outer surface of the half-sphere. The LeXT is not capable of measuring steep slopes, so the measurements shown in the transition between the gray and black surfaces may be too high. It seems that the gold coating on the gray area is missing in the middle of the sphere. Fig. 5.18 shows a patch on the gold plate that could be the missing gold coating.

Figure 5.17: The gold coated sphere after subtracting the gold surface. A line cut in the LeXT software indicates that the black area is about 310 nm below the height of the intact gold coating. Also the line cut indicated a diameter of the missing gold coating of 53 μm.
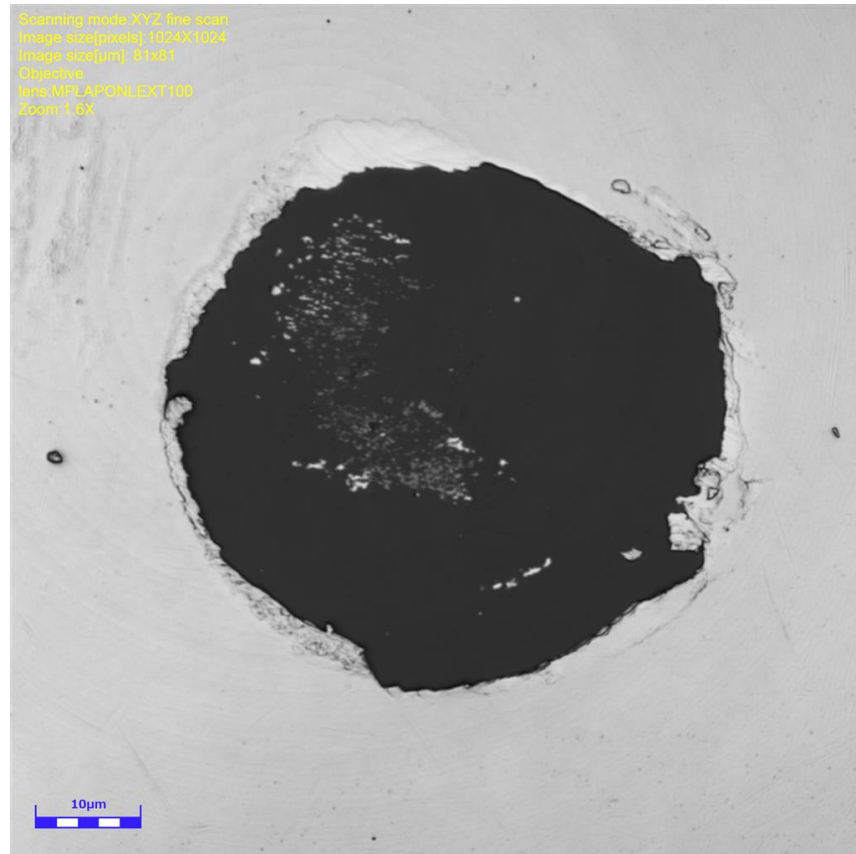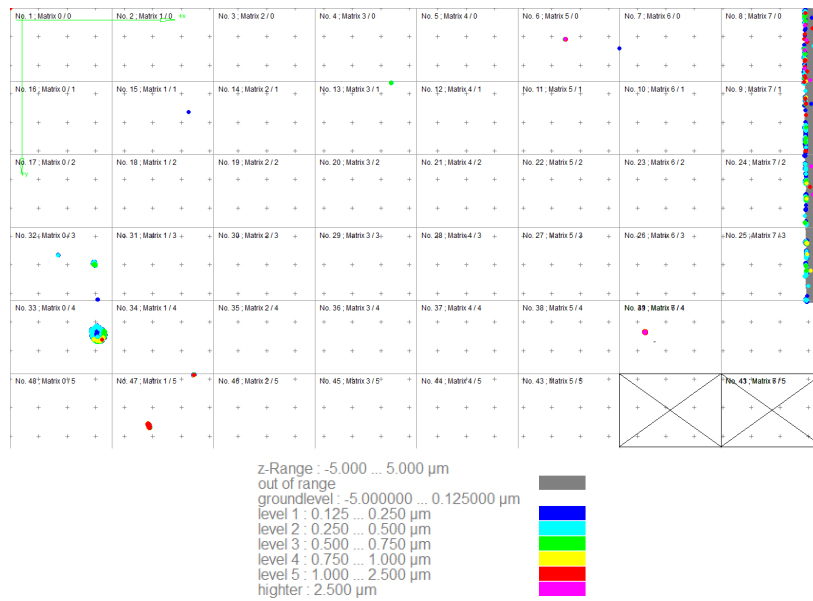
Figure 5.18: Measurement of particles on the gold plate using the Sensofar SNeox. This figure shows roughly 5 % of the surface of the plate. Particles of at least a height of 125 nm are marked as blue dots. For larger particles see the legend. On the bottom left a larger patch between 200 nm and 750 nm in size is visible. That could be the missing gold coating from Fig. 5.16.

exact radius of the half-sphere. Unfortunately a large patch of missing gold coating was found on the half-sphere as seen in Fig. 5.16. After subtracting a sphere from the 3D model, it was possible to measure the height of the missing patch. It was almost constant and about 310 nm deep and had a diameter of 53 μm. The most obvious explanation for this large patch of missing gold is a collision of the force sensor with the sphere with a severe impact speed. Most likely is that this happened during the first approach when the offset for the distance Fabry-Pérot was still unknown. This means that the results of the experiments with this force sensor are not usable anymore. This could also explain why in each approach phase during the measurement a collision was detected: without this large patch of gold, the distance calibration generated a wrong result. Fig. 5.18 shows a measurement of the plate after disassembling the experiment. It shows detected particles on the plate with at least 125 nm height. On field 33 a larger amount of mass was detected, which could have been the gold fragments from the sphere.
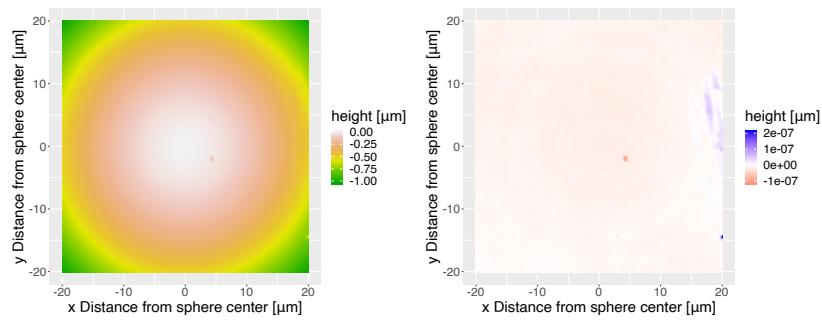
Figure 5.19: On the left is the half-sphere as a heat map. On the right is only the surface of the half-sphere.

5.6 Measurements between September 2017 and February 2018

After the large patch of missing gold was detected on the surface of the gold coated half-sphere, a new measurement was planned.

5.6.1 Surface of the Probes

5.6.1.1 Sphere

Fig. 5.19 shows a measurement with the LeXT confocal laser scanning microscope.

5.6.1.2 Gold-coated plate

The complete surface of the gold plate was measured with a *SNeox* confocal white light interferometer. With a $50\times$ objective it has a lateral resolution of $260\,\text{nm}$ and a height resolution of $10\,\text{nm}$. It was used to search the area for particles. In one measurement the *SNeox* has a field of view of $(351 \times 264)\,\mu\text{m}$, therefore the complete surface of $10 \times 10\text{mm}^2$ was scanned with 1131 single data acquisitions. A height of $50\,\text{nm}$ was used for the particle threshold. Every pixel above $50\,\text{nm}$ was marked as particle and there were approximately approximately $645\,000$ particles on the plate in total. After the measurement, the largest square without any particle on the surface was searched. The result of that analysis was that an area of $2 \times 2\text{mm}^2$ was particle free. This means that the plate is feasible for the measurement. This measurement is shown in Fig. 5.20.

5.6.2 Force Sensor Characteristics

5.6.2.1 Vibration Measurement Cavity

The vibration measurement cavity has a length of $19.73735\,\mu\text{m}$ with a fit error of $0.114\,\text{nm}$ and a repeatability of $0.137\,\text{nm}$ for 20 measurements. This leads to an optimal wavelength for the vibration measurement of $1563.335\,\text{nm}$, with a repeatability of $0.011\,\text{nm}$.
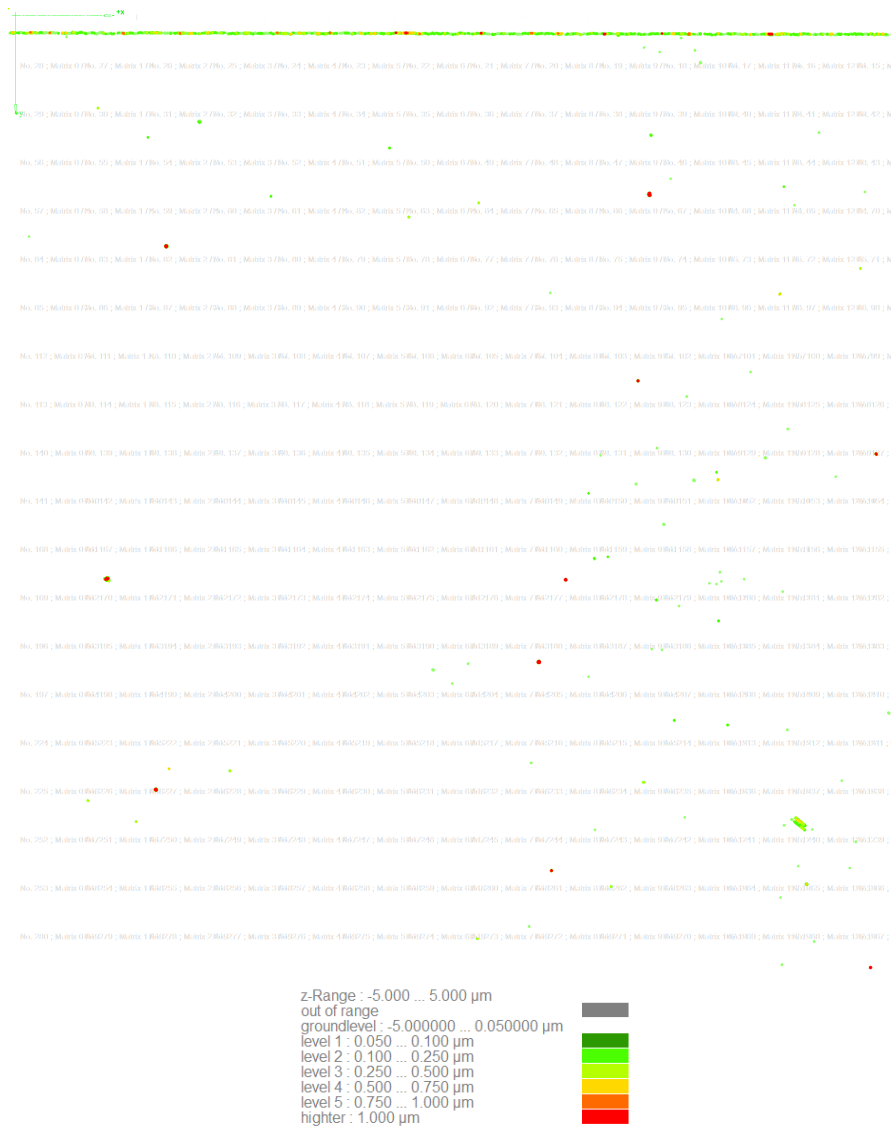
Figure 5.20: One quadrant of the particle measurement of the gold plate is shown. The quadrant shows $(5 \times 5)\,\mathrm{mm}^2$. At the center of the quadrant is a $2\,\mathrm{mm}$ large area which is particle free.
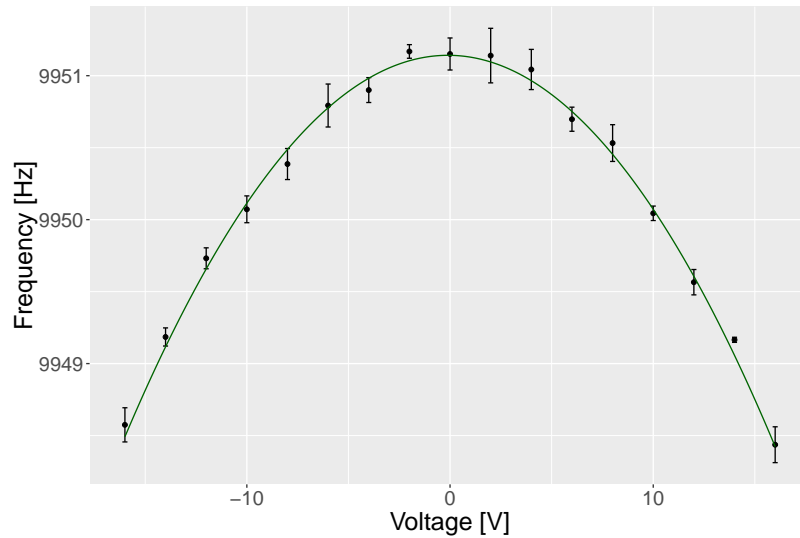
Figure 5.21: Distance calibration. $d_{\text{Offset}} = (90.697 \pm 0.008)$ μm at the distance $d_0 = (999 \pm 8)$ nm, $V_m = -(0.10 \pm 0.07)$ V.

5.6.2.2 Resonance Frequency and Quality Factor

The new measured quality factor and resonance frequency are:

$$f_0 = (9511.14 \pm 0.02) \text{ Hz} \tag{5.24}$$
$$Q = 5540 \pm 490 \tag{5.25}$$

Unfortunately the low quality factor means, that the vibration amplitude is lower than in the experiments before. This meant that the PLL was unable to lock onto the vibration. For all measurements using this force sensor the resonance curve method was used to measure frequency changes.

5.6.3 Distance Calibration

The distance calibration for the new force sensor and its gold plate was done at the beginning of February 2018. The approach of the plate to the sphere was done slowly. After each step the frequency was measured with a high voltage applied. And since the resonance curve method was used to measure the frequency, measuring one frequency took about 15 minutes. Fig. 5.21 shows the result of the distance calibration. As can be seen, the measurement noise is higher than it was in the measurement period of summer 2017. This comes from the low quality factor and the missing PLL. The standard error of the distance measurement is with 8.2 nm much higher than it was for the measurement in summer 2017 ($1 <$ nm).

5.6.4 Distance Frequency Curve Measurement

Three distance-frequency curves were measured in this measurement run. The first one is shown in Fig. 5.22. The contact potential was compensated for by applying a voltage of 102 mV, which was measured in the distance
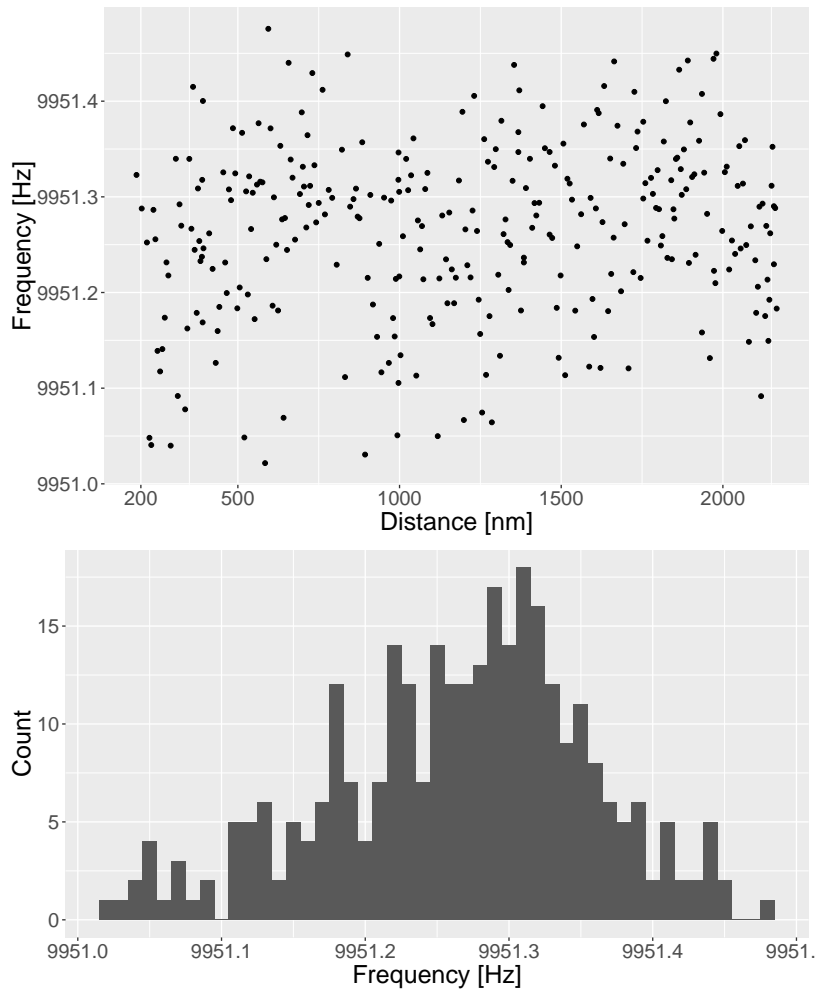
Figure 5.22: Measurement on February 20th 2018. $V_m = 102\,\text{mV}$ was compensated accordingly to the contact potential during the distance measurement. It was not possible to measure any resonance curve below the distance of approximately $200\,\text{nm}$. The lower plot shows the histogram of the measurement with a binwidth of $10\,\text{mHz}$.
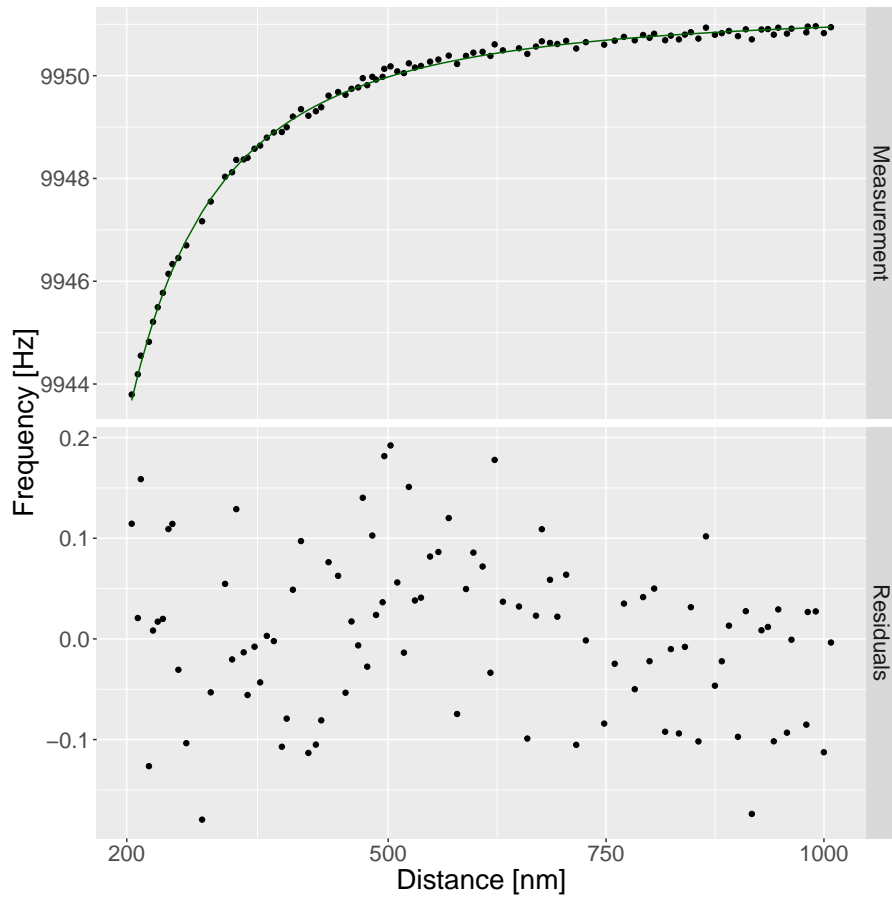
Figure 5.23: Measurement taken on February 24th 2018. The measurement was done with a voltage of 6 V applied between the half-sphere and the plate. The lower plot shows the residuals after subtracting the calculated frequency for the electrostatic force due to the applied voltage.
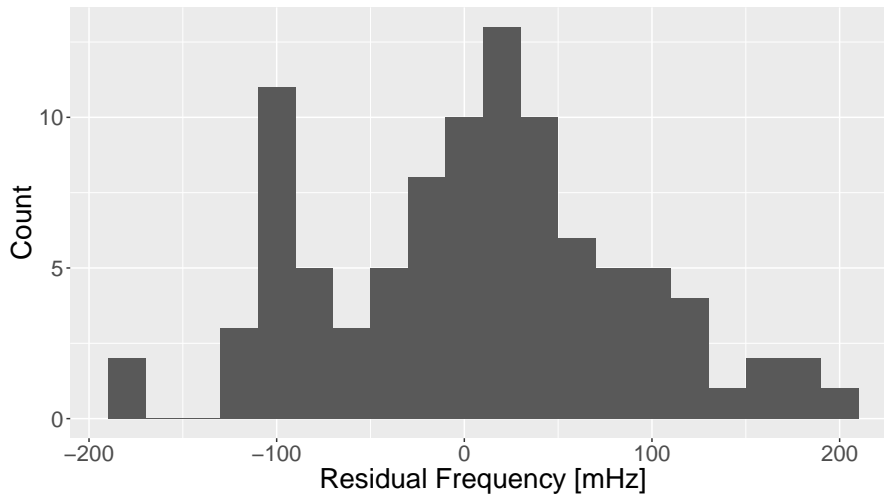
Figure 5.24: Histogram of the measurement taken on February 24th 2018. The binwidth is 20 mHz. The small peak at -100 mHz has a too small effect size to assume anything other than noise for it.

offset measurement. There were two results of the first measurement. First: it was not possible to measure a resonance curve below a distance of 200 nm. Possible reasons could be that the amplitude was too low to be detected or perhaps due to some kind of a particle on the surface let the vibration vanish altogether. A jump-into-contact was not visible, the cavity length of the vibration interferometer was the same as before. Second: Above that distance, there was no trend in the data. A trend could have come for example from the Casimir force, but the sensitivity of the experiment was not large enough to measure that.

For the next measurement, a voltage of 6 V was applied between the half-sphere and the plate. The result is shown in Fig. 5.23. The electrostatic force is visible, but the residuals do not suggest any additional force. Also in these cases the Casimir effect was not measured due to a lack in sensitivity. Their distribution is plotted as histogram in Fig. 5.24. The measurement with an applied voltage of 6 V was repeated. The results are the same and shown in Fig. 5.25. Also the distribution of residuals is plotted in Fig. 5.26. The residuals have a standard deviation of 0.1 Hz. At a distance of 200 nm this results in not detecting any additional Yukawa-like gravitational effect; and the corresponding curve as shown as α-λ-plot in Fig. 5.27. As expected, the result is still in the yellow part of that plot.
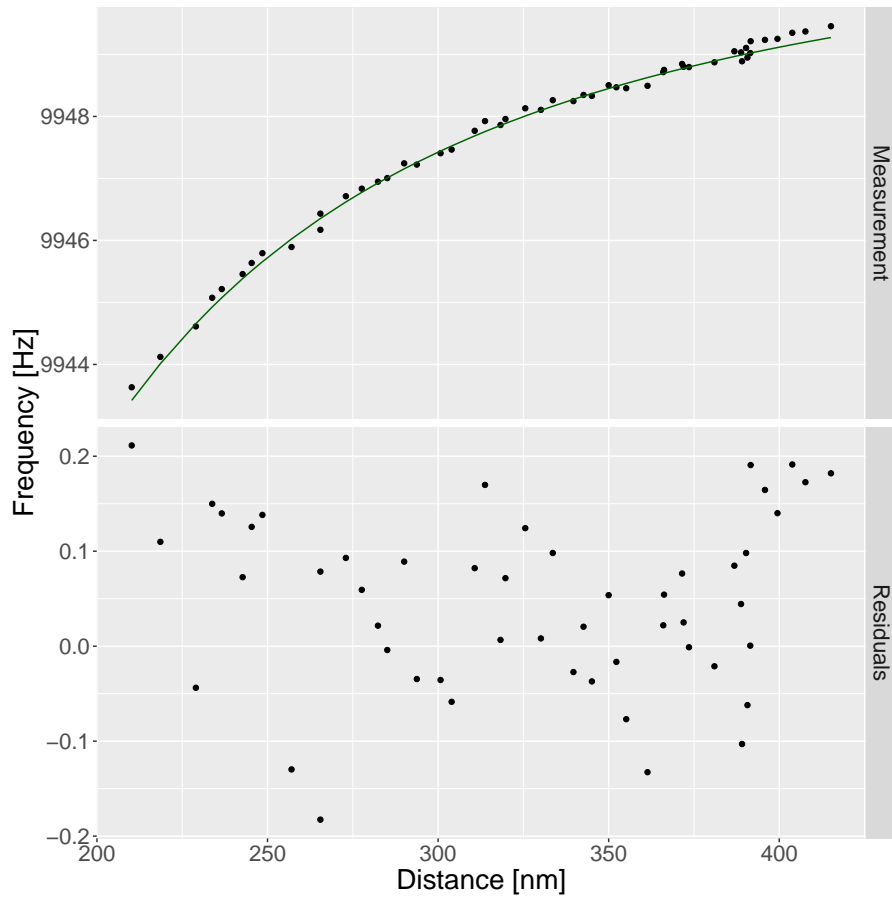
Figure 5.25: Measurement taken on February 25th 2018. The measurement was done like the former measurement with an voltage of 6 V applied between the half-sphere and the plate. The lower plot shows the residuals after subtracting the calculated frequency.
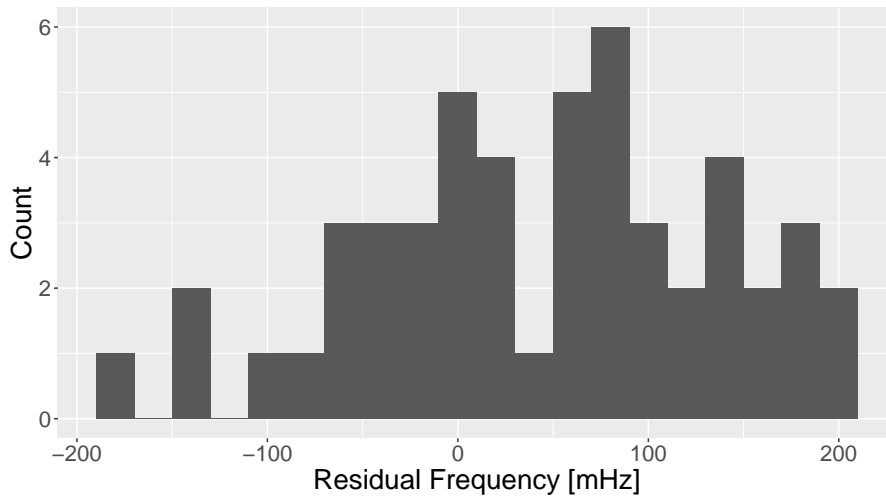
Figure 5.26: Histogram of the measurement on February 25th 2018. The binwidth is 20 mHz. The count in each bin is too small to give meaning to the peaks in the histogram.
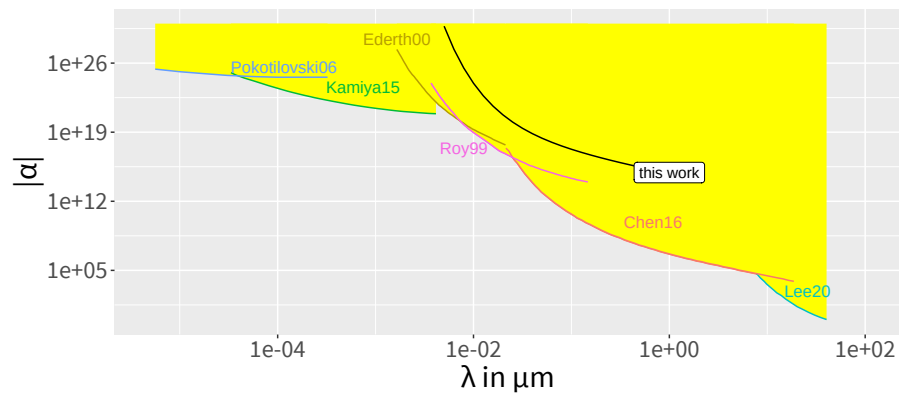
Figure 5.27: This experiment placed into the Yukawa α-λ-plot. The result is calculated with a distance of 200 nm and 0.1 Hz frequency accuracy. Both values were chosen from the previous measurements, where no significant change in frequency was measured down to 200 nm that could account to an effect size of 0.1 Hz.

Chapter 6

Lessons Learned and Suggestions for Future Experiments

In summer 2013 I started working on an experiment to search for deviations from Newtonian Gravity. Section 6.1 describes the first approach and why it finally failed. From the mid of 2015 I was developing a new experimental concept to find deviations from gravity. We faced some difficulties during the preparation. Some of those difficulties could be solved, but some were not solved. The two most pressing difficulties were the quality factor of the force sensor, and the fact that below a distance of 200 nm we were unable to detect any vibrations of the force sensor. The issue of the quality factor was a problem in the final experimental run that ran until Feb. 2018, but the force sensor from summer 2017 had a feasible quality factor. Those ideas are described from section 6.2 onward.

6.1   Failed First Approach with Shielding Membranes

My first approach for the experiment [150] was a concept with a parallel plates geometry instead of the plate sphere geometry. It was based on the nanonewton force facility developed by Brand et al. [151] shown in Fig. 6.1. The goal was to measure the force between two parallel plates with a resolution of 10^{-12} N after integrating $2 \cdot 10^4$ s. The hard part of the experiment was shielding it from the Casimir force, to have an experiment that only measures a gravitational force and not electrical and Casimir forces. For this purpose S. Bütefisch developed the design of the nanostructured silicon based Yukawaattraktor. The design of the Yukawaattraktor is shown in Fig. 6.3. The idea was not to use one large membrane, but ten thousand small membranes. The plate was split into ten thousand silicon sticks with a gold coating. The membranes should have been held by a silicon based grid structure.

The plate parallel to the Yukawaattraktor was called the detector plate. The pendulum of the nanonewton force facility was placed inside an electrical field with a small hole in the middle to measure probes on the pendulum.
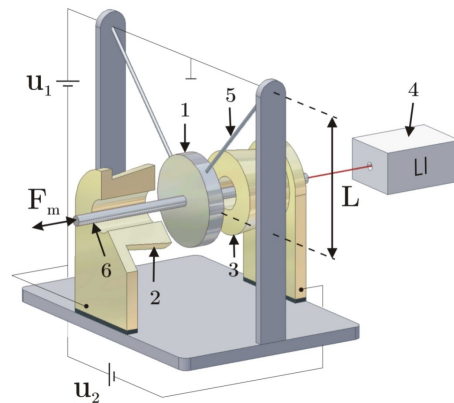
Figure 6.1: Nanonewton force facility developed by Brand et al.[151]. A gold coated plate is suspended between two annulus formed electrodes. The electrodes are used to reduce the stiffness of the pendulum to increase the force sensitivity. The aimed force sensitivity was planned to be 10^{-12} N.

But we didn't want the gravity measurement to be influenced by the electrical field and we wanted to have larger surface area for the Yukawaattraktor. So we chose to attach two plates connected with a copper stick to the pendulum. One of those plates was the detector plate and the other was to counter balance the detector plate and it was used for the interferometer that measured the movement of the pendulum. Fig. 6.2 shows the detector plate and the pendulum.

Also shown in Fig. 6.3 is another important part of the experiment. Since the goal was to measure the force between parallel plates, it was necessary to measure any tilting of the plates. The concept was to use two laser beams, one that reflects on the back of the Yukawaattraktor and one that reflects on the detector plate. Both beams are split after the reflection using a beam splitter and are measured at the center of four quadrant photo diodes. With a four quadrant photodiode it is possible to measure the tilt of a plate.

We had two major issues during building the experiment, which finally led us stop the the two parallel plates experiment:

1st: After S. Buetefisch tried a few times, we discovered that the membrane fabrication was not good enough to generate about 10000 intact membranes. Even a few broken membranes would lead to very large measurement errors. A picture of the fabricated gold membranes is shown in Fig. 6.4.

2nd: The other problem was that the size needed for the necessary measurement accuracy of more than a centimeter has the disadvantage that the surface shape of the two plates was not accurate to a nanometer. Measurements showed that deviations from a perfect plate were more than a micrometer. With an aimed distance of a micrometer for the measurement, this shape of the silicon based plate was unusable. Fig. 6.5 shows the measurement of the disc pendulum without a copper stick glued on and one disc pendulum with a copper stick glued on. We also tried an adhesive filled with micrometer-sized spheres, that work as spacer to reduce shrinkage effects of the adhesive.

A better solution to shield the Casimir effect for experiments at distances
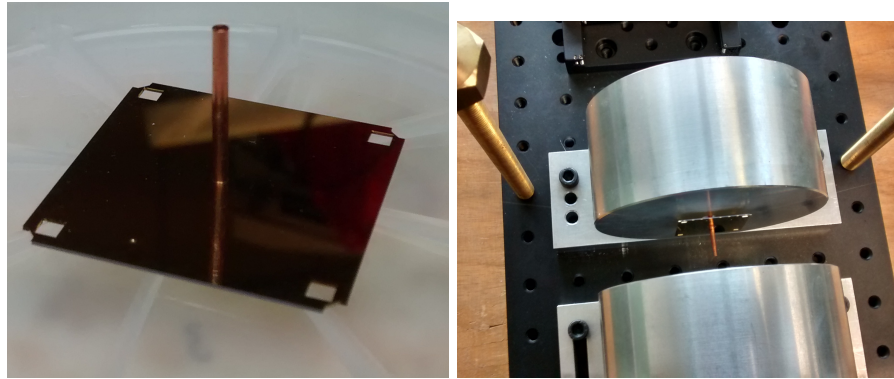
Figure 6.2: The left shows the detector plate with the glued copper stick. The right image shows the pendulum with the copper clamp attached during a detector plate assemble trial. The round aluminum cylinders were used as dummy for the electrodes. Also the $25\,\mu$m gold wire suspension of the pendulum is visible.
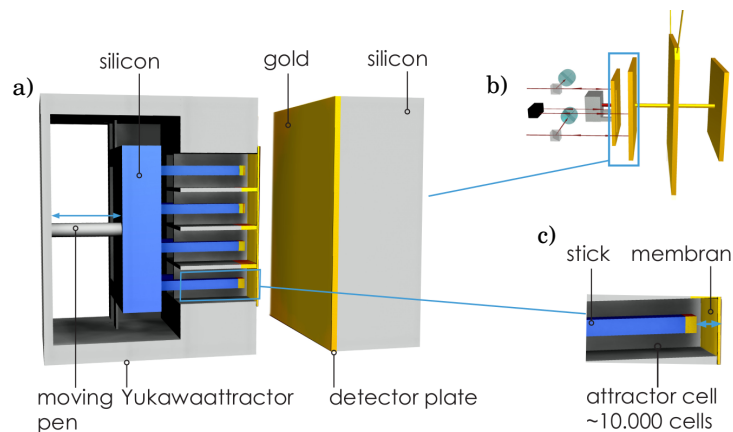
Figure 6.3: Measurement concept as shown in my talk at the DPG spring meeting 2014 [150]. b) shows the whole measurement setup. The pendulum is shown with both plates attached. The additional plates on the pendulum were needed to measure outside of the electrodes that were shown in Fig. 6.1. The left part of b) shows the four quadrant photodiodes. Their purpose was to measure any tilting of the detector plate and the Yukawaattraktor. a) shows the Yukawaattraktor facing the detector plate. c) shows a single cell of the Yukawaattraktor. The stick inside each cell is attached to the silicon base plate which itself is connected to a piezo slide. The silicon grid that holds the membrane is also shown at a).
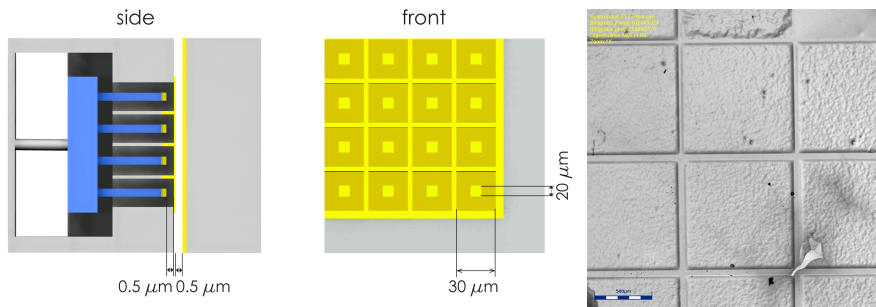
Figure 6.4: Picture of the gold membranes in a grid. The image to the left
shows a side view of the Yukawaattraktor. It shows the planned distances
between the sticks and the membrane, as well as the distance to the detector
plate. The planned sizes of the sticks and the membranes are shown in the
middle image, which is the front view of the Yukawaattraktor. The image to
the right shows a picture of fabricated membranes on the grid. There are also
some visible imperfections.
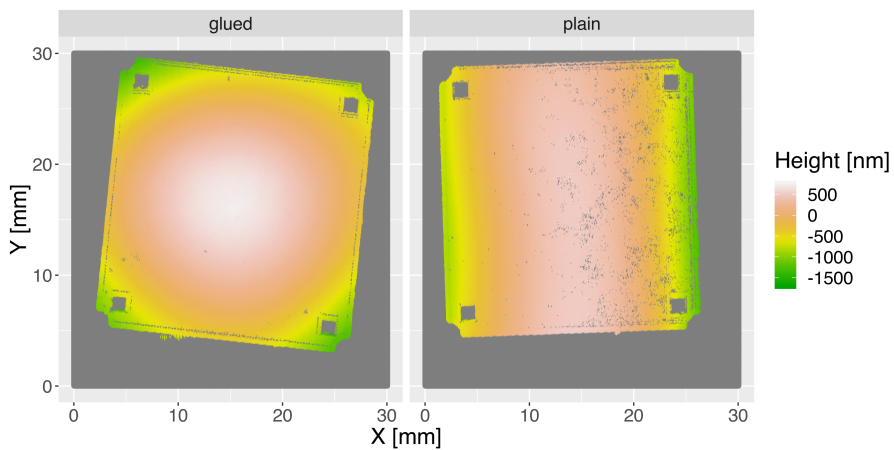
Figure 6.5: Shapes of gold coated silicon wafer used as a pendulum in the
nanonewton force facility. On the left is the wafer with a copper stick glued
in the middle. On the right is the pendulum without a copper stick.

larger than 200 nm was published at end of 2014 on the website *arXiv.org*, and finally published 2016 by Chen et al. [51]. The experiment was discussed in section 2.2.4.
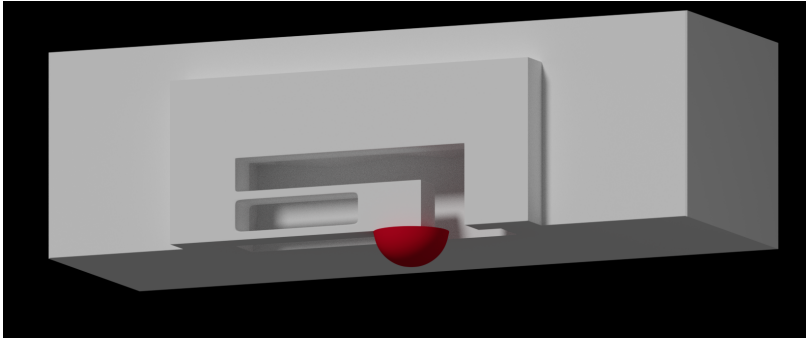
Figure 6.6: 3D image of the force sensor attached to a glass block. Two
important lessons we learned during our experiments were: First: Use rounded
edges inside the parallelogram flexure. Second: Place the force sensor on the
left where the parallelogram flexure is connected to the glass block completely
on the glass block, and place the moving part of the force sensor over a milled
hole in the glass block.

6.2   Increase Surface Quality

Not being able to measure any vibrations below a distance of 200 nm was one
of the major issues we faced during each experiment. One likely reason for
this problem was the surface imperfections. Figure 5.20 shows particles found
on the plate used in the last experiment. While large parts of the plate have
no particles of a size of 50 nm or larger, there are some larger particles that
are of a size of $1\,\mu$m and above. We would need to reduce the amount of
particles on the surface to get clearer results. One necessary step against
particles on surfaces is to perform all the preparations inside a clean room.
Large plates with a small roughness can have a larger waviness. This type of
surface imperfection could lead to wrong results of the distance calibration
and should also be avoided. This can occur when gluing a plate to the
specimen holder.
Fig. 5.19 shows another type of imperfection – the sphere has a small hole
that is about 150 nm deep. It is several micrometers away from the center of
the sphere. It would be best to avoid these kinds of imperfections. Bezerra et
al. [152] argues that such small surface imperfections make it impossible to
perform accurate measurements of the Casimir force between a plate and a
sphere. However, the surface imperfections they use for their calculations are
merely artificial and do not represent real surfaces.

6.3   Optimize the Quality Factor

In the last measurement run in winter 2017/2018, the vibration amplitude of
the force sensor was too low to use the PLL. The reason was a low quality
factor Q. During all experiments, we had different quality factors from $2 \cdot 10^3$
to 10^5. We learned about different influences that correspond to the quality
factor.
Fig. 6.6 shows how the force sensor should be attached on top of the glass
block, and our experiments taught us that rounded edges inside of the
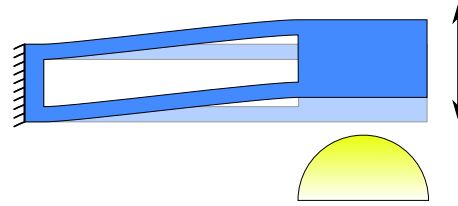
Figure 6.7: Using the force sensor as the plate, and the half-sphere approaches it. The relative distance measurement must be performed from the side of the sphere.

parallelogram flexure are important for a higher quality factor. The gold coating described in section 4.1.3.1 has a major impact on the quality factor. It is important to have an electrical connection, but there could be some other options. For example, if the gold coating is applied not on the side of the force sensor that faces to the gold plate but just on top of the force sensor, how does it impact the quality factor? Another idea is not to use fused silica, but a force sensor made of doted silicon. This would have the advantage that the bulk material is conducting and no gold coating on the parallelogram flexure is needed anymore. A gold coating is still needed on the test mass and the sphere. But it would be sufficient to coat the sphere on top only, as long as it is electrically connected to the force sensor. But connecting the sphere to the force sensor electrically without coating the flexure of the force sensor would be more difficult than just coating everything with gold after the force sensor and sphere are assembled, however, gluing the sphere to the test mass of the force sensor is also suboptimal for the quality factor. One option for this would be to gold coat only the test mass of the force sensor and use it as plate. The sphere would be the approaching object as seen in Fig. 6.7. In this case, the distance measurement Fabry-Pérot should be attached to the specimen holder that moves the sphere. A 3D positioning system moves the sphere to the center of the test mass. Using the force sensor as the plate would also have the advantage of providing a higher resonance frequency. The resonance frequencies of the force sensor with the half-sphere attached is by 50% lower than resonance frequency without the half-sphere. A higher resonance frequency means that the measured signal (Δf) for the same force is higher.
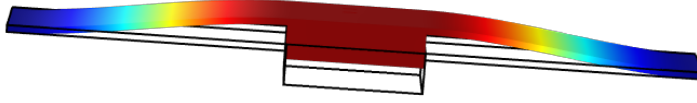
Figure 6.8: A two-legged force sensor with the test mass in the middle. Both ends are fixed. It has a depth of 0.5 mm with a length of the legs of 2 mm. The height of the legs is 0.05 mm. The test mass has a length of 1 mm and a height of 0.3 mm.

6.4 Changing the Force Sensor to a Smaller Stiffness

In Eq. (3.164) the stiffness k is inversely proportional to the frequency shift. This means that a higher stiffness means a lower frequency shift. But if we could reduce the stiffness while leaving every other property the same, the frequency shift increases and also increases the measurement sensitivity. The main obstacle to a small stiffness is the jump-into-contact. This means the stiffness should be much greater than the force gradient:

$$\frac{\mathrm{d}F}{\mathrm{d}x} \ll k \tag{6.1}$$

The force gradient for a sphere with radius $R = 0.5$ mm at a distance of 10 nm is about 20 N/m.
At the parallelogram flexure there are several parameters that influence the stiffness. Unfortunately, each of these parameters influence the resonance frequency as well. For example the length, the thickness, and the height of the flexures. The two-legged force sensor shown in Fig. 6.8 has an eigenfrequency of 8 kHz and a stiffness of 1 kN/m. Decreasing the height of the flexures of the parallelogram flexure decreases the stiffness. Increasing the length of the flexures also reduces stiffness. Both also decreases the frequency. When the separation of the flexures decreases, the total mass of the test mass decreases also, which leads to a higher frequency. When gluing a sphere to the parallelogram flexure, a higher stiffness is necessary to make sure the force sensor does not bend under the increased weight. But when using the force sensor as plate, it would be possible to go to an even lower stiffness. For example, a height of each flexure of 25 μm and a length of 2.5 mm and a flexure separation of 300 μm leads to a stiffness of 72 N/m at a resonance frequency of 2 kHz. This would increase the frequency shift compared to the experiments in this thesis by a factor of 35. But the stiffness is not that much larger than the force gradient can be. So this stiffness would a risky choice.

6.5 Using a Different Positioning System

A piezo positioner needs an applied voltage to hold a position, and the stick-slip positioners can hold the position without an applied voltage. The stick-slip principle has one large disadvantage. When performing one step,
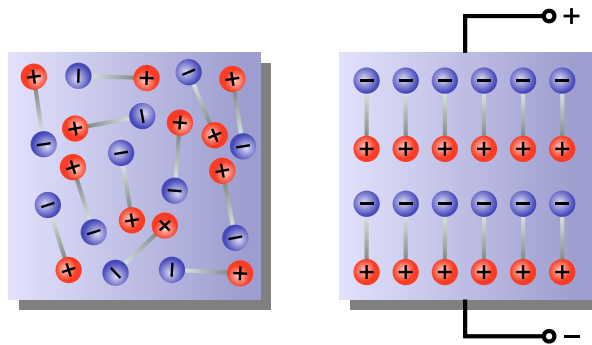
Figure 6.9: The Weiss domains [153] are randomly ordered (left). Applying a large voltage leads to completely polarized Weiss domains in the piezo (right).

the piezo movement gives an impulse to the whole system and the force sensor vibrates with a large amplitude of about 50 nm, which would lead to a collision during steps at small distances.
Before a piezoceramic is used as a positioner, the Weiss domains have to be polarized, as shown in Fig. 6.9. After the polarization procedure, it is possible to deform the piezoceramic with an applied force linear to the applied voltage [154]. But it is also possible to use an unpolarized piezoceramic. An applied voltage changes the Weiss domains of the ceramic and therefore also the size. Changing the Weiss domains means that no applied voltage is needed to hold the position. On the other hand, a negative voltage is needed at the piezo to change the Weiss domains back. Most piezocontrollers do not have the capability to change to an inverse voltage, because the polarization can be destroyed. Therefore it is necessary to implement a new controller for that operation mode of a piezo positioner. At the moment, this is done at PI and called *PIRest*, as mentioned by their employees H. Marth and J. Reiser [155]. Since 2018 they are available for purchase and have a adjustable step size of something below 10 nm.

6.6 High Finesse Fabry-Pérot Cavity

The experiment in this thesis used a low finesse Fabry-Pérot cavity to measure the vibration and the distance between force sensor and plate. If the finesse of the vibration measurement cavity was about $3 \cdot 10^5$, the line width of one signal maximum would be about 1 nm as can be seen in Fig. 6.10. This would increase the signal for the phase locked loop and make it easier to measure the frequency. A low amplitude of vibration is harder to measure, but it is better to estimate the force gradient at a specific distance. A larger amplitude means that the frequency change depends on different distances. So an amplitude below 1 nm is better for the measurement, but harder to measure. A high finesse Fabry-Pérot cavity can help here. Guzmán et al. [156] were able to achieve a displacement sensitivity of 200 $\frac{am}{\sqrt{Hz}}$, for example. A high finesse could be achieved by using focused-ion-beams to mill the fibers at both ends to get the light collimated after the fiber and then coating the ends with higher reflecting coatings for example.
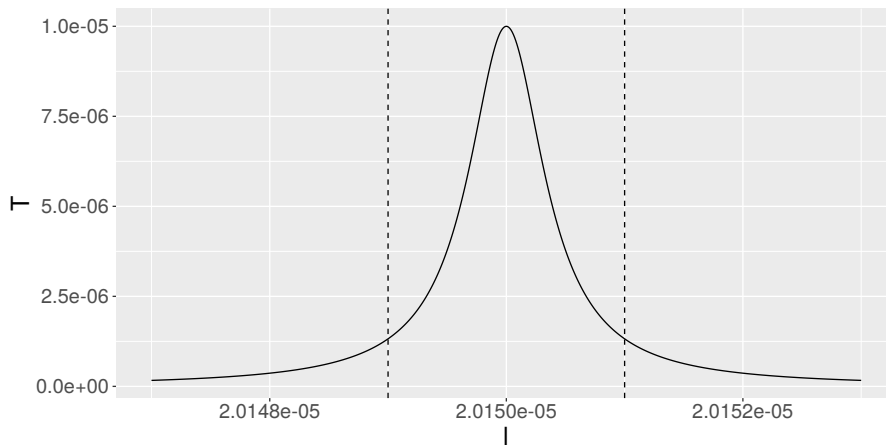
Figure 6.10: Intensity over the cavity length of a high-finesse Fabry-Pérot.
The dashed lines are $2\,\mathrm{nm}$ apart.

6.7 Separate Laser Sources for both Interferometers

In this experiment, the laser source for both interferometers was the same.
This means, when sweeping the wavelength of the distance interferometer to
measure the current distance, the frequency measurement does not work and
the PLL has to lock again afterwards. So it might be better to use different
laser sources for both interferometers. In the experiments of this thesis, the
current cavity length of the vibration measurement interferometer was used
to detect collisions. So while measuring the frequency with a PLL measuring
the absolute value of the vibration interferometer can be done for a collision
detection. Also it would be possible to continuously measure the distance
during the experiments. This could make it easier to make corrections for
temperature changes.

Scenario	k $[\frac{\text{N}}{\text{m}}]$	Q	R [mm]	f_0 [kHz]	Δf [Hz]	d_0 [nm]
A	1000	10^5	0.5	8	0.001	50
B	72	10^5	0.5	2	0.001	50

Table 6.1: Both scenarios are based on the force sensors described in section 6.4. The assumption is to achieve a Q of at least 10^5, using the same spheres with radii R that were used for this thesis. The stiffness k and the eigenfrequencies f_0 came from simulations. The goal is to measure the force gradient at a minimum distance of d_0 at a frequency shift due to the Casimir force of Δf.
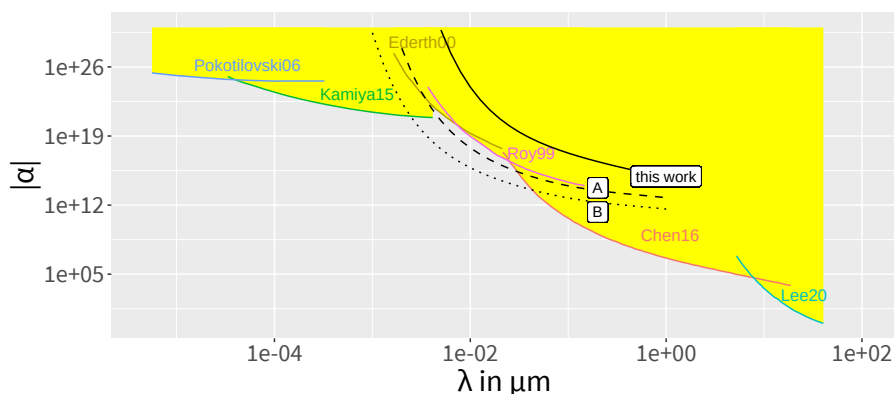
Figure 6.11: The dotted and the dashed lines are scenarios for improved experiments as described by Table 6.1. The results from this thesis are displayed for comparison.

6.8 Measurement Scenarios of an Improved Experiment

The above sections described how an improved experiment could look like. They can be combined into two scenarios: A, and B. The scenarios are described in Table 6.1. Both scenarios assume that it is possible to measure data at a distance between the half-sphere and the plate of $d_0 = 50\,\text{nm}$, and that the frequency shift due to the Casimir effect is matched with an accuracy of $1\,\text{mHz}$. We did not reach a distance below $d_0 = 200\,\text{nm}$ and measuring still a signal. We do not know the reason for that but surface imperfections are the best guess so far. All in all to achieve both assumptions, the hardest part would be to increase the surface quality enough to measure the Casimir effect with the desired precision; it is not easy to calculate the Casimir force for real surface imperfections as stated by Bezerra et al. [152]. In case of scenario B, a lower precision of $10\,\text{mHz}$ would be good enough to get the same boundaries as for scenario A. The possible new boundaries for both scenarios are shown in Fig. 6.11.

Chapter 7

Outlook and Conclusion

7.1 Conclusion

During our first experimental approach, it took us two and a half years to realize that it was not possible with our resources to get an experiment running to measure gravitational forces. However, we were able to construct a completely new experiment within a year. In the year afterwards we learned a lot while doing experiments with the new setup. Unfortunately, one year is not enough for this and my contract ended without moving the boundaries of Newtonian gravity. But, the new experimental setup is looking promising for any future attempts, and I hope this thesis can help to build an improved version of the experiment.

7.2 Outlook

In September 2018 the University of Hannover and the PTB were awarded a grant by the DFG as excellence cluster. The goal of the cluster is to improve metrology at the quantum frontier. This could be an opportunity to improve the experiment of this thesis and move forwards in the search for quantum gravity.

7.3 Acknowledgments

Special thanks to Sebastian Bütefisch for helping me with the first approach and a realistic view on the possibility to realize it. Thanks to Ludger Koenders for providing me with the resources to make my yukawa force spectroscopy experiment possible. Thanks to Felipe Guzman for providing me with an idea for a new force sensor. Thanks to Gerhard Heinzel for providing me advice on fiber interferometers, phase locked loops and bandpass amplifiers. Thanks to Lars Andresen for building electrical circuits to optimize the PLL input and to use the old school positional system from software using a *Raspberry Pi* mini computer. Special thanks to Helmut Wolf who assembled my experiment.

Appendix A

Appendix: Math

A.1 Plausibility check for Eq. (3.164)

Assume a force that follows Hooke's Law:

$$F(x) = k_2 x \tag{A.1}$$

Put it into the integral part of 3.164:

$$F\left(z + a(1+u)\frac{u}{\sqrt{1-u^2}}\right) \tag{A.2}$$

$$\Rightarrow k_2\left(x + a(1+u)\frac{u}{\sqrt{1-u^2}}\right) \tag{A.3}$$

Put this back into the integral:

$$\int_{-1}^{1} \frac{uk_2 z + k_2 au + k_2 au^2}{\sqrt{1-u^2}} \, \mathrm{d}u \tag{A.4}$$

$$\Rightarrow k_2\left(\sqrt{1-u^2}\left(-a - \frac{au}{2} - z\right) + \frac{1}{2}a\sin^{-1}u\right)\Big|_{-1}^{1} \tag{A.5}$$

$$\Rightarrow \frac{1}{2}k_2 a\left(\frac{\pi}{2} - \left(-\frac{\pi}{2}\right)\right) = \frac{1}{2}k_2 a\pi \tag{A.6}$$

$$\Rightarrow^{(3.164)} -\frac{1}{\pi a k_1}\frac{1}{2}k_2 a\pi = \frac{\Delta\omega}{\omega_{\mathrm{res}}} \tag{A.7}$$

$$\Rightarrow -\frac{1}{2}\frac{k_2}{k_1} = \frac{\Delta\omega}{\omega_{\mathrm{res}}} \tag{A.8}$$

ω_2 is the resonance frequency of the whole system build by two parallel springs. Parallel springs mean that the stiffness for both of them is the sum of both spring constants. For $\Delta\omega/\omega_{\mathrm{res}}$ this means:

$$\omega_{\mathrm{res}} = \sqrt{\frac{k_1}{m}} \tag{A.9}$$

$$\omega_2 = \sqrt{\frac{k_1 + k_2}{m}} \tag{A.10}$$

$$\frac{\omega_{\mathrm{res}} - \omega_2}{\omega_{\mathrm{res}}} = 1 - \frac{\omega_2}{\omega_{\mathrm{res}}} \tag{A.11}$$

$$= 1 - \frac{\sqrt{\frac{k_1 + k_2}{m}}}{\sqrt{\frac{k_1}{m}}} = 1 - \sqrt{\frac{k_1 + k_2}{m} \cdot \frac{m}{k_1}} \tag{A.12}$$

$$= 1 - \sqrt{\frac{k_1 + k_2}{k_1}} = 1 - \sqrt{1 + \frac{k_2}{k_1}} \tag{A.13}$$

And put it all together:

$$-\frac{1}{2}\frac{k_2}{k1} = 1 - \sqrt{1 + \frac{k_2}{k_1}} \tag{A.14}$$

$$\sqrt{1 + \frac{k_2}{k_1}} = 1 + \frac{1}{2}\frac{k_2}{k1} \qquad |()^2 \tag{A.15}$$

$$1 + \frac{k_2}{k_1} = \left(1 + \frac{1}{2}\frac{k_2}{k_1}\right)^2 \tag{A.16}$$

$$1 + \frac{k_2}{k_1} = 1^2 + 2\frac{1}{2}\frac{k_2}{k_1} + \frac{1}{4}\left(\frac{k_2}{k_1}\right)^2 \tag{A.17}$$

$$1 + \frac{k_2}{k_1} = 1 + \frac{k_2}{k_1} + \frac{1}{4}\left(\frac{k_2}{k_1}\right)^2 \tag{A.18}$$

And with $|k_2| \ll |k_1|$, $\left(\frac{k_2}{k_1}\right)^2 \to 0$, are both results approximately equal.

Bibliography

[1] Henry Cavendish. Experiments to Determine the Density of the Earth. By Henry Cavendish, Esq. F. R. S. and A. S. *Philosophical Transactions of the Royal Society of London*, 88:469–526, 1798. ISSN 02610523. doi: 10.2307/106988. URL http://www.jstor.org/stable/106988.

[2] Chris Burks. Cavendish Torsion Balance Diagram, August 2007. URL https://commons.wikimedia.org/wiki/File:Cavendish_Torsion_Balance_Diagram.svg.

[3] R. D. Reasenberg, J. F. Chandler, N. R. Colmenares, N. H. Johnson, T. W. Murphy, and I. I. Shapiro. Modeling and Analysis of the APOLLO Lunar Laser Ranging Data. *ArXiv e-prints*, August 2016.

[4] Ephraim Fischbach, Daniel Sudarsky, Aaron Szafer, Carrick Talmadge, and S. H. Aronson. Reanalysis of the Eo *uml* tvös experiment. *Phys. Rev. Lett.*, 56(1):3–6, January 1986. doi: 10.1103/PhysRevLett.56.3. URL http://link.aps.org/doi/10.1103/PhysRevLett.56.3.

[5] A. J. Krasznahorkay, M. Csatlós, L. Csige, Z. Gácsi, J. Gulyás, M. Hunyadi, I. Kuti, B. M. Nyakó, L. Stuhl, J. Timár, T. G. Tornyi, Zs. Vajta, T. J. Ketel, and A. Krasznahorkay. Observation of Anomalous Internal Pair Creation in $^8\mathrm{Be}$: A Possible Indication of a Light, Neutral Boson. *Phys. Rev. Lett.*, 116(4):042501, January 2016. doi: 10.1103/PhysRevLett.116.042501. URL https://link.aps.org/doi/10.1103/PhysRevLett.116.042501.

[6] A. J. Krasznahorkay, M. Csatlos, L. Csige, J. Gulyas, M. Koszta, B. Szihalmi, J. Timar, D. S. Firak, A. Nagy, N. J. Sas, and A. Krasznahorkay. New evidence supporting the existence of the hypothetic X17 particle. *arXiv e-prints*, page arXiv:1910.10459, October 2019.

[7] Wikipedia contributors. *List of unsolved problems in physics*. April 2017. URL https://en.wikipedia.org/w/index.php?title=List_of_unsolved_problems_in_physics&oldid=776623791.

[8] Steven Weinberg. The cosmological constant problem. *Rev. Mod. Phys.*, 61(1):1–23, January 1989. doi: 10.1103/RevModPhys.61.1. URL http://link.aps.org/doi/10.1103/RevModPhys.61.1.

[9] Hendrik B. G. Casimir. On the attraction between two perfectly conducting plates. *Proceedings Koninklijke Nederlandsche Akademie van Wetenschappen*, 51(6-10), 1948.

[10] Jérôme Martin. Everything you always wanted to know about the cosmological constant problem (but were afraid to ask). *Comptes Rendus Physique*, 13(6):566 – 665, 2012. ISSN 1631-0705. doi: http://dx.doi.org/10.1016/j.crhy.2012.04.008. URL http://www.sciencedirect.com/science/article/pii/S1631070512000497.

[11] Ignatios Antoniadis, Nima Arkani-Hamed, Savas Dimopoulos, and Georgi (Gia) Dvali. New dimensions at a millimeter to a fermi and superstring at a TeV. *Physics Letters B*, (436):257–263, September 1998. doi: 10.1016/S0370-2693(98)00860-0.

[12] R. D. Peccei and Helen R. Quinn. CP Conservation in the Presence of Pseudoparticles. *Phys. Rev. Lett.*, 38(25):1440–1443, June 1977. doi: 10.1103/PhysRevLett.38.1440. URL http://link.aps.org/doi/10.1103/PhysRevLett.38.1440.

[13] G. Dvali and L. Funcke. Domestic Axion. *ArXiv e-prints*, (1608.08969v1), August 2016.

[14] J. Khoury and A. Weltman. Chameleon cosmology. *Phys. Rev. D*, 69 (4):044026, February 2004. doi: 10.1103/PhysRevD.69.044026.

[15] J. Edholm, A. S. Koshelev, and A. Mazumdar. Universality of testing ghost-free gravity. *ArXiv e-prints*, (arXiv:1604.01989), April 2016.

[16] G. Binnig, C. F. Quate, and Ch. Gerber. Atomic Force Microscope. *Phys. Rev. Lett.*, 56(9):930–933, March 1986. doi: 10.1103/PhysRevLett.56.930. URL https://link.aps.org/doi/10.1103/PhysRevLett.56.930.

[17] Franz J. Giessibl. Advances in atomic force microscopy. *Rev. Mod. Phys.*, 75(3):949–983, July 2003. doi: 10.1103/RevModPhys.75.949. URL http://link.aps.org/doi/10.1103/RevModPhys.75.949.

[18] John Melcher, Julian Stirling, Felipe Guzmán Cervantes, Jon R. Pratt, and Gordon A. Shaw. A self-calibrating optomechanical force sensor with femtonewton resolution. *Applied Physics Letters*, 105(23):–, 2014. doi: http://dx.doi.org/10.1063/1.4903801. URL http://scitation.aip.org/content/aip/journal/apl/105/23/10.1063/1.4903801.

[19] Clifford M. Will. The Confrontation between General Relativity and Experiment. *Living Reviews in Relativity*, 17(1):4, June 2014. ISSN 1433-8351. doi: 10.12942/lrr-2014-4. URL https://doi.org/10.12942/lrr-2014-4.

[20] Frank Watson Dyson, Arthur Stanley Eddington, and Charles Davidson. IX. A determination of the deflection of light by the sun's gravitational field, from observations made at the total eclipse of May 29, 1919. *Philosophical Transactions of the Royal Society of London. Series A, Containing Papers of a Mathematical or Physical Character*, 220 (571-581):291–333, 1920.

[21] George Frederick Dodwell and Charles R Davidson. Determination of the deflection of light by the Sun's gravitational field from observations made at Cordillo Downs, South Australia, during the total eclipse of 1922 September 21. *Monthly Notices of the Royal Astronomical Society*, 84:150, 1924.

[22] L.J. King, N. Jackson, R.D. Blandford, M.N. Bremer, I.W.A. Browne, A.G. De Bruyn, C. Fassnacht, L. Koopmans, D. Marlow, and P.N. Wilkinson. A complete infrared Einstein ring in the gravitational lens system B1938 + 666. *Monthly Notices of the Royal Astronomical Society*, 295(2):L41–L44, 1998. ISSN 0035-8711. doi: 10.1046/j.1365-8711. 1998.295241.x. URL `https://doi.org/10.1046/j.1365-8711.1998.295241.x`.

[23] M. Froeschle, F. Mignard, and F. Arenou. Determination of the PPN Parameter gamma with the HIPPARCOS Data. In R. M. Bonnet, E. Høg, P. L. Bernacca, L. Emiliani, A. Blaauw, C. Turon, J. Kovalevsky, L. Lindegren, H. Hassan, and M. Bouffard, editors, *Hipparcos - Venice '97*, volume 402 of *ESA Special Publication*, pages 49–52, August 1997.

[24] Aurélien Hees, Christophe Le Poncin-Lafitte, Daniel Hestroffer, and Pedro David. Local tests of gravitation with Gaia observations of Solar System Objects. *Proceedings of the International Astronomical Union*, 12(S330):63–66, 2017. doi: 10.1017/S1743921317005907.

[25] SB Lambert and Chr Le Poncin-Lafitte. Improved determination of by VLBI. *Astronomy & Astrophysics*, 529:A70, 2011.

[26] Irwin I. Shapiro. Fourth Test of General Relativity. *Phys. Rev. Lett.*, 13 (26):789–791, December 1964. doi: 10.1103/PhysRevLett.13.789. URL `https://link.aps.org/doi/10.1103/PhysRevLett.13.789`.

[27] R. D. Reasenberg, I. I. Shapiro, P. E. MacNeil, R. B. Goldstein, J. C. Breidenthal, J. P. Brenkle, D. L. Cain, T. M. Kaufman, T. A. Komarek, and A. I. Zygielbaum. Viking relativity experiment - Verification of signal retardation by solar gravity. \apjl, 234:L219–L221, December 1979. doi: 10.1086/183144.

[28] B. Bertotti, L. Iess, and P. Tortora. A test of general relativity using radio links with the Cassini spacecraft. \nat, 425(6956):374–376, September 2003. doi: 10.1038/nature01997.

[29] C. W. Chou, D. B. Hume, T. Rosenband, and D. J. Wineland. Optical Clocks and Relativity. *Science*, 329(5999):1630–1633, 2010. ISSN 0036-8075. doi: 10.1126/science.1192720. URL `https://science.sciencemag.org/content/329/5999/1630`.

[30] Thomas B. Bahder. Relativity of GPS measurement. *Phys. Rev. D*, 68 (6):063005, September 2003. doi: 10.1103/PhysRevD.68.063005. URL `https://link.aps.org/doi/10.1103/PhysRevD.68.063005`.

[31] Michael J. Longo. New Precision Tests of the Einstein Equivalence Principle from Sn1987a. *Phys. Rev. Lett.*, 60(3):173–175, January 1988. doi: 10.1103/PhysRevLett.60.173. URL `https://link.aps.org/doi/10.1103/PhysRevLett.60.173`.

[32] E. O. Kahya. A decisive test to confirm or rule out the existence of dark matter emulators using gravitational wave observations. *Classical and Quantum Gravity*, 25(18):184008, September 2008. doi: 10.1088/0264-9381/25/18/184008. URL `https://doi.org/10.1088%2F0264-9381%2F25%2F18%2F184008`.

[33] S. Boran, S. Desai, E. O. Kahya, and R. P. Woodard. GW170817 falsifies dark matter emulators. *Phys. Rev. D*, 97(4):041501, February 2018. doi: 10.1103/PhysRevD.97.041501. URL `https://link.aps.org/doi/10.1103/PhysRevD.97.041501`.

[34] Eolo Di Casola, Stefano Liberati, and Sebastiano Sonego. Nonequivalence of equivalence principles. *American Journal of Physics*, 83(1):39–46, 2015. doi: 10.1119/1.4895342. URL `https://doi.org/10.1119/1.4895342`.

[35] Ben-Oni. Das Bild soll das Äquivalenzprinzip der allgemeinen Relativitätstheorie illustrieren., December 2006. URL `https://de.wikipedia.org/w/index.php?title=Datei:%C3%84P.gif`.

[36] J. W. MOFFAT and V. T. TOTH. MODIFIED JORDANBRANS-DICKE THEORY WITH SCALAR CURRENT AND THE EDDINGTONROBERTSON -PARAMETER. *International Journal of Modern Physics D*, 21(12):1250084, 2012. doi: 10.1142/S0218271812500848. URL `https://doi.org/10.1142/S0218271812500848`.

[37] M. A. Green, J. W. Moffat, and V. T. Toth. Modified gravity (MOG), the speed of gravitational radiation and the event GW170817/GRB170817A. *Physics Letters B*, 780:300 – 302, 2018. ISSN 0370-2693. doi: https://doi.org/10.1016/j.physletb.2018.03.015. URL `http://www.sciencedirect.com/science/article/pii/S0370269318302041`.

[38] S. M. Ransom, I. H. Stairs, A. M. Archibald, J. W. T. Hessels, D. L. Kaplan, M. H. van Kerkwijk, J. Boyles, A. T. Deller, S. Chatterjee, and A. Schechtman-Rook. A millisecond pulsar in a stellar triple system. \nat, 505(7484):520–524, January 2014. doi: 10.1038/nature12917.

[39] Anne M. Archibald, Nina V. Gusinskaia, Jason W. T. Hessels, Adam T. Deller, David L. Kaplan, Duncan R. Lorimer, Ryan S. Lynch, Scott M. Ransom, and Ingrid H. Stairs. Universality of free fall from the orbital motion of a pulsar in a stellar triple system. \nat, 559(7712):73–76, July 2018. doi: 10.1038/s41586-018-0265-1.

[40] Antonio Genova, Erwan Mazarico, Sander Goossens, Frank G Lemoine, Gregory A Neumann, David E Smith, and Maria T Zuber. Solar system expansion and strong equivalence principle as seen by the NASA MESSENGER mission. *Nature communications*, 9(1):289, 2018.

[41] James G. Williams, Slava G. Turyshev, and Dale H. Boggs. Lunar laser ranging tests of the equivalence principle. *Classical and Quantum Gravity*, 29(18):184004, August 2012. doi: 10.1088/0264-9381/29/18/184004. URL `https://doi.org/10.1088%2F0264-9381%2F29%2F18%2F184004`.

[42] A. S. Konopliv, S. W. Asmar, W. M. Folkner, Ö. Karatekin, D. C. Nunes, S. E. Smrekar, C. F. Yoder, and M. T. Zuber. Mars high resolution gravity fields from MRO, Mars seasonal gravity, and other dynamical parameters. *carus*, 211:401–428, January 2011. doi: 10.1016/j.icarus.2010.10.004.

[43] Albert Einstein. Über gravitationswellen. *Sitzungsberichte der Königlich Preu\s sischen Akademie der Wissenschaften (Berlin), Seite 154-167.*, 1918.

[44] B. P. Abbott, R. Abbott, T. D. Abbott, M. R. Abernathy, F. Acernese, K. Ackley, C. Adams, T. Adams, P. Addesso, R. X. Adhikari, V. B. Adya, C. Affeldt, M. Agathos, K. Agatsuma, N. Aggarwal, O. D. Aguiar, L. Aiello, A. Ain, P. Ajith, B. Allen, A. Allocca, P. A. Altin, S. B. Anderson, W. G. Anderson, K. Arai, M. A. Arain, M. C. Araya, C. C. Arceneaux, J. S. Areeda, N. Arnaud, K. G. Arun, S. Ascenzi, G. Ashton, M. Ast, S. M. Aston, P. Astone, P. Aufmuth, C. Aulbert, S. Babak, P. Bacon, M. K. M. Bader, P. T. Baker, F. Baldaccini, G. Ballardin, S. W. Ballmer, J. C. Barayoga, S. E. Barclay, B. C. Barish, D. Barker, F. Barone, B. Barr, L. Barsotti, M. Barsuglia, D. Barta, J. Bartlett, M. A. Barton, I. Bartos, R. Bassiri, A. Basti, J. C. Batch, C. Baune, V. Bavigadda, M. Bazzan, B. Behnke, M. Bejger, C. Belczynski, A. S. Bell, C. J. Bell, B. K. Berger, J. Bergman, G. Bergmann, C. P. L. Berry, D. Bersanetti, A. Bertolini, J. Betzwieser, S. Bhagwat, R. Bhandare, I. A. Bilenko, G. Billingsley, J. Birch, R. Birney, O. Birnholtz, S. Biscans, A. Bisht, M. Bitossi, C. Biwer, M. A. Bizouard, J. K. Blackburn, C. D. Blair, D. G. Blair, R. M. Blair, S. Bloemen, O. Bock, T. P. Bodiya, M. Boer, G. Bogaert, C. Bogan, A. Bohe, P. Bojtos, C. Bond, F. Bondu, R. Bonnand, B. A. Boom, R. Bork, V. Boschi, S. Bose, Y. Bouffanais, A. Bozzi, C. Bradaschia, P. R. Brady, V. B. Braginsky, M. Branchesi, J. E. Brau, T. Briant, A. Brillet, M. Brinkmann, V. Brisson, P. Brockill, A. F. Brooks, D. A. Brown, D. D. Brown, N. M. Brown, C. C. Buchanan, A. Buikema, T. Bulik, H. J. Bulten, A. Buonanno, D. Buskulic, C. Buy, R. L. Byer, M. Cabero, L. Cadonati, G. Cagnoli, C. Cahillane, J. Calderón Bustillo, T. Callister, E. Calloni, J. B. Camp, K. C. Cannon, J. Cao, C. D. Capano, E. Capocasa, F. Carbognani, S. Caride, J. Casanueva Diaz, C. Casentini, S. Caudill, M. Cavaglià, F. Cavalier, R. Cavalieri, G. Cella, C. B. Cepeda, L. Cerboni Baiardi, G. Cerretani, E. Cesarini, R. Chakraborty, T. Chalermsongsak, S. J. Chamberlin, M. Chan, S. Chao, P. Charlton, E. Chassande-Mottin, H. Y. Chen, Y. Chen, C. Cheng, A. Chincarini, A. Chiummo, H. S. Cho, M. Cho, J. H. Chow, N. Christensen, Q. Chu, S. Chua, S. Chung, G. Ciani, F. Clara, J. A. Clark, F. Cleva, E. Coccia, P.-F. Cohadon, A. Colla, C. G. Collette, L. Cominsky, M. Constancio, A. Conte, L. Conti, D. Cook, T. R. Corbitt, N. Cornish, A. Corsi, S. Cortese, C. A. Costa, M. W. Coughlin, S. B. Coughlin, J.-P. Coulon, S. T. Countryman, P. Couvares, E. E. Cowan, D. M. Coward, M. J. Cowart, D. C. Coyne, R. Coyne, K. Craig, J. D. E. Creighton, T. D. Creighton, J. Cripe, S. G. Crowder, A. M. Cruise, A. Cumming, L. Cunningham, E. Cuoco, T. Dal Canton, S. L. Danilishin, S. D'Antonio, K. Danzmann, N. S. Darman, C. F. Da Silva Costa, V. Dattilo, I. Dave, H. P. Daveloza, M. Davier, G. S. Davies, E. J. Daw, R. Day, S. De, D. DeBra, G. Debreczeni, J. Degallaix, M. De Laurentis, S. Deléglise, W. Del Pozzo, T. Denker, T. Dent, H. Dereli, V. Dergachev, R. T. DeRosa, R. De Rosa, R. DeSalvo, S. Dhurandhar, M. C. Díaz, L. Di Fiore, M. Di Giovanni, A. Di Lieto, S. Di Pace, I. Di Palma, A. Di Virgilio, G. Dojcinoski, V. Dolique, F. Donovan, K. L. Dooley, S. Doravari, R. Douglas, T. P. Downes, M. Drago, R. W. P. Drever, J. C. Driggers, Z. Du, M. Ducrot, S. E. Dwyer, T. B. Edo, M. C. Edwards, A. Effler, H.-B. Eggenstein, P. Ehrens, J. Eichholz, S. S. Eikenberry, W. Engels, R. C. Essick, T. Etzel, M. Evans, T. M. Evans, R. Everett, M. Factourovich, V. Fafone, H. Fair, S. Fairhurst,

X. Fan, Q. Fang, S. Farinon, B. Farr, W. M. Farr, M. Favata, M. Fays, H. Fehrmann, M. M. Fejer, D. Feldbaum, I. Ferrante, E. C. Ferreira, F. Ferrini, F. Fidecaro, L. S. Finn, I. Fiori, D. Fiorucci, R. P. Fisher, R. Flaminio, M. Fletcher, H. Fong, J.-D. Fournier, S. Franco, S. Frasca, F. Frasconi, M. Frede, Z. Frei, A. Freise, R. Frey, V. Frey, T. T. Fricke, P. Fritschel, V. V. Frolov, P. Fulda, M. Fyffe, H. A. G. Gabbard, J. R. Gair, L. Gammaitoni, S. G. Gaonkar, F. Garufi, A. Gatto, G. Gaur, N. Gehrels, G. Gemme, B. Gendre, E. Genin, A. Gennai, J. George, L. Gergely, V. Germain, Abhirup Ghosh, Archisman Ghosh, S. Ghosh, J. A. Giaime, K. D. Giardina, A. Giazotto, K. Gill, A. Glaefke, J. R. Gleason, E. Goetz, R. Goetz, L. Gondan, G. González, J. M. Gonzalez Castro, A. Gopakumar, N. A. Gordon, M. L. Gorodetsky, S. E. Gossan, M. Gosselin, R. Gouaty, C. Graef, P. B. Graff, M. Granata, A. Grant, S. Gras, C. Gray, G. Greco, A. C. Green, R. J. S. Greenhalgh, P. Groot, H. Grote, S. Grunewald, G. M. Guidi, X. Guo, A. Gupta, M. K. Gupta, K. E. Gushwa, E. K. Gustafson, R. Gustafson, J. J. Hacker, B. R. Hall, E. D. Hall, G. Hammond, M. Haney, M. M. Hanke, J. Hanks, C. Hanna, M. D. Hannam, J. Hanson, T. Hardwick, J. Harms, G. M. Harry, I. W. Harry, M. J. Hart, M. T. Hartman, C.-J. Haster, K. Haughian, J. Healy, J. Heefner, A. Heidmann, M. C. Heintze, G. Heinzel, H. Heitmann, P. Hello, G. Hemming, M. Hendry, I. S. Heng, J. Hennig, A. W. Heptonstall, M. Heurs, S. Hild, D. Hoak, K. A. Hodge, D. Hofman, S. E. Hollitt, K. Holt, D. E. Holz, P. Hopkins, D. J. Hosken, J. Hough, E. A. Houston, E. J. Howell, Y. M. Hu, S. Huang, E. A. Huerta, D. Huet, B. Hughey, S. Husa, S. H. Huttner, T. Huynh-Dinh, A. Idrisy, N. Indik, D. R. Ingram, R. Inta, H. N. Isa, J.-M. Isac, M. Isi, G. Islas, T. Isogai, B. R. Iyer, K. Izumi, M. B. Jacobson, T. Jacqmin, H. Jang, K. Jani, P. Jaranowski, S. Jawahar, F. Jiménez-Forteza, W. W. Johnson, N. K. Johnson-McDaniel, D. I. Jones, R. Jones, R. J. G. Jonker, L. Ju, K. Haris, C. V. Kalaghatgi, V. Kalogera, S. Kandhasamy, G. Kang, J. B. Kanner, S. Karki, M. Kasprzack, E. Katsavounidis, W. Katzman, S. Kaufer, T. Kaur, K. Kawabe, F. Kawazoe, F. Kéfélian, M. S. Kehl, D. Keitel, D. B. Kelley, W. Kells, R. Kennedy, D. G. Keppel, J. S. Key, A. Khalaidovski, F. Y. Khalili, I. Khan, S. Khan, Z. Khan, E. A. Khazanov, N. Kijbunchoo, C. Kim, J. Kim, K. Kim, Nam-Gyu Kim, Namjun Kim, Y.-M. Kim, E. J. King, P. J. King, D. L. Kinzel, J. S. Kissel, L. Kleybolte, S. Klimenko, S. M. Koehlenbeck, K. Kokeyama, S. Koley, V. Kondrashov, A. Kontos, S. Koranda, M. Korobko, W. Z. Korth, I. Kowalska, D. B. Kozak, V. Kringel, B. Krishnan, A. Królak, C. Krueger, G. Kuehn, P. Kumar, R. Kumar, L. Kuo, A. Kutynia, P. Kwee, B. D. Lackey, M. Landry, J. Lange, B. Lantz, P. D. Lasky, A. Lazzarini, C. Lazzaro, P. Leaci, S. Leavey, E. O. Lebigot, C. H. Lee, H. K. Lee, H. M. Lee, K. Lee, A. Lenon, M. Leonardi, J. R. Leong, N. Leroy, N. Letendre, Y. Levin, B. M. Levine, T. G. F. Li, A. Libson, T. B. Littenberg, N. A. Lockerbie, J. Logue, A. L. Lombardi, L. T. London, J. E. Lord, M. Lorenzini, V. Loriette, M. Lormand, G. Losurdo, J. D. Lough, C. O. Lousto, G. Lovelace, H. Lück, A. P. Lundgren, J. Luo, R. Lynch, Y. Ma, T. MacDonald, B. Machenschalk, M. MacInnis, D. M. Macleod, F. Magaña-Sandoval, R. M. Magee, M. Mageswaran, E. Majorana, I. Maksimovic, V. Malvezzi, N. Man, I. Mandel, V. Mandic, V. Mangano, G. L. Mansell, M. Manske, M. Mantovani, F. Marchesoni, F. Marion, S. Márka, Z. Márka, A. S. Markosyan, E. Maros,

F. Martelli, L. Martellini, I. W. Martin, R. M. Martin, D. V. Martynov, J. N. Marx, K. Mason, A. Masserot, T. J. Massinger, M. Masso-Reid, F. Matichard, L. Matone, N. Mavalvala, N. Mazumder, G. Mazzolo, R. McCarthy, D. E. McClelland, S. McCormick, S. C. McGuire, G. McIntyre, J. McIver, D. J. McManus, S. T. McWilliams, D. Meacher, G. D. Meadors, J. Meidam, A. Melatos, G. Mendell, D. Mendoza-Gandara, R. A. Mercer, E. Merilh, M. Merzougui, S. Meshkov, C. Messenger, C. Messick, P. M. Meyers, F. Mezzani, H. Miao, C. Michel, H. Middleton, E. E. Mikhailov, L. Milano, J. Miller, M. Millhouse, Y. Minenkov, J. Ming, S. Mirshekari, C. Mishra, S. Mitra, V. P. Mitrofanov, G. Mitselmakher, R. Mittleman, A. Moggi, M. Mohan, S. R. P. Mohapatra, M. Montani, B. C. Moore, C. J. Moore, D. Moraru, G. Moreno, S. R. Morriss, K. Mossavi, B. Mours, C. M. Mow-Lowry, C. L. Mueller, G. Mueller, A. W. Muir, Arunava Mukherjee, D. Mukherjee, S. Mukherjee, N. Mukund, A. Mullavey, J. Munch, D. J. Murphy, P. G. Murray, A. Mytidis, I. Nardecchia, L. Naticchioni, R. K. Nayak, V. Necula, K. Nedkova, G. Nelemans, M. Neri, A. Neunzert, G. Newton, T. T. Nguyen, A. B. Nielsen, S. Nissanke, A. Nitz, F. Nocera, D. Nolting, M. E. N. Normandin, L. K. Nuttall, J. Oberling, E. Ochsner, J. O'Dell, E. Oelker, G. H. Ogin, J. J. Oh, S. H. Oh, F. Ohme, M. Oliver, P. Oppermann, Richard J. Oram, B. O'Reilly, R. O'Shaughnessy, C. D. Ott, D. J. Ottaway, R. S. Ottens, H. Overmier, B. J. Owen, A. Pai, S. A. Pai, J. R. Palamos, O. Palashov, C. Palomba, A. Pal-Singh, H. Pan, Y. Pan, C. Pankow, F. Pannarale, B. C. Pant, F. Paoletti, A. Paoli, M. A. Papa, H. R. Paris, W. Parker, D. Pascucci, A. Pasqualetti, R. Passaquieti, D. Passuello, B. Patricelli, Z. Patrick, B. L. Pearlstone, M. Pedraza, R. Pedurand, L. Pekowsky, A. Pele, S. Penn, A. Perreca, H. P. Pfeiffer, M. Phelps, O. Piccinni, M. Pichot, M. Pickenpack, F. Piergiovanni, V. Pierro, G. Pillant, L. Pinard, I. M. Pinto, M. Pitkin, J. H. Poeld, R. Poggiani, P. Popolizio, A. Post, J. Powell, J. Prasad, V. Predoi, S. S. Premachandra, T. Prestegard, L. R. Price, M. Prijatelj, M. Principe, S. Privitera, R. Prix, G. A. Prodi, L. Prokhorov, O. Puncken, M. Punturo, P. Puppo, M. Pürrer, H. Qi, J. Qin, V. Quetschke, E. A. Quintero, R. Quitzow-James, F. J. Raab, D. S. Rabeling, H. Radkins, P. Raffai, S. Raja, M. Rakhmanov, C. R. Ramet, P. Rapagnani, V. Raymond, M. Razzano, V. Re, J. Read, C. M. Reed, T. Regimbau, L. Rei, S. Reid, D. H. Reitze, H. Rew, S. D. Reyes, F. Ricci, K. Riles, N. A. Robertson, R. Robie, F. Robinet, A. Rocchi, L. Rolland, J. G. Rollins, V. J. Roma, J. D. Romano, R. Romano, G. Romanov, J. H. Romie, D. Rosińska \textbackslashacuten\textbackslashelse \textbackslashfiska, S. Rowan, A. Rüdiger, P. Ruggi, K. Ryan, S. Sachdev, T. Sadecki, L. Sadeghian, L. Salconi, M. Saleem, F. Salemi, A. Samajdar, L. Sammut, L. M. Sampson, E. J. Sanchez, V. Sandberg, B. Sandeen, G. H. Sanders, J. R. Sanders, B. Sassolas, B. S. Sathyaprakash, P. R. Saulson, O. Sauter, R. L. Savage, A. Sawadsky, P. Schale, R. Schilling, J. Schmidt, P. Schmidt, R. Schnabel, R. M. S. Schofield, A. Schönbeck, E. Schreiber, D. Schuette, B. F. Schutz, J. Scott, S. M. Scott, D. Sellers, A. S. Sengupta, D. Sentenac, V. Sequino, A. Sergeev, G. Serna, Y. Setyawati, A. Sevigny, D. A. Shaddock, T. Shaffer, S. Shah, M. S. Shahriar, M. Shaltev, Z. Shao, B. Shapiro, P. Shawhan, A. Sheperd, D. H. Shoemaker, D. M. Shoemaker, K. Siellez, X. Siemens, D. Sigg, A. D. Silva, D. Simakov, A. Singer, L. P. Singer, A. Singh, R. Singh, A. Singhal,

A. M. Sintes, B. J. J. Slagmolen, J. R. Smith, M. R. Smith, N. D. Smith, R. J. E. Smith, E. J. Son, B. Sorazu, F. Sorrentino, T. Souradeep, A. K. Srivastava, A. Staley, M. Steinke, J. Steinlechner, S. Steinlechner, D. Steinmeyer, B. C. Stephens, S. P. Stevenson, R. Stone, K. A. Strain, N. Straniero, G. Stratta, N. A. Strauss, S. Strigin, R. Sturani, A. L. Stuver, T. Z. Summerscales, L. Sun, P. J. Sutton, B. L. Swinkels, M. J. Szczepafmmode \textbackslashacuten\textbackslashelse \textbackslashficzyk, M. Tacca, D. Talukder, D. B. Tanner, M. Tápai, S. P. Tarabrin, A. Taracchini, R. Taylor, T. Theeg, M. P. Thirugnanasambandam, E. G. Thomas, M. Thomas, P. Thomas, K. A. Thorne, K. S. Thorne, E. Thrane, S. Tiwari, V. Tiwari, K. V. Tokmakov, C. Tomlinson, M. Tonelli, C. V. Torres, C. I. Torrie, D. Töyrä, F. Travasso, G. Traylor, D. Trifirò, M. C. Tringali, L. Trozzo, M. Tse, M. Turconi, D. Tuyenbayev, D. Ugolini, C. S. Unnikrishnan, A. L. Urban, S. A. Usman, H. Vahlbruch, G. Vajente, G. Valdes, M. Vallisneri, N. van Bakel, M. van Beuzekom, J. F. J. van den Brand, C. Van Den Broeck, D. C. Vander-Hyde, L. van der Schaaf, J. V. van Heijningen, A. A. van Veggel, M. Vardaro, S. Vass, M. Vasúth, R. Vaulin, A. Vecchio, G. Vedovato, J. Veitch, P. J. Veitch, K. Venkateswara, D. Verkindt, F. Vetrano, A. Viceré, S. Vinciguerra, D. J. Vine, J.-Y. Vinet, S. Vitale, T. Vo, H. Vocca, C. Vorvick, D. Voss, W. D. Vousden, S. P. Vyatchanin, A. R. Wade, L. E. Wade, M. Wade, S. J. Waldman, M. Walker, L. Wallace, S. Walsh, G. Wang, H. Wang, M. Wang, X. Wang, Y. Wang, H. Ward, R. L. Ward, J. Warner, M. Was, B. Weaver, L.-W. Wei, M. Weinert, A. J. Weinstein, R. Weiss, T. Welborn, L. Wen, P. WeSSels, T. Westphal, K. Wette, J. T. Whelan, S. E. Whitcomb, D. J. White, B. F. Whiting, K. Wiesner, C. Wilkinson, P. A. Willems, L. Williams, R. D. Williams, A. R. Williamson, J. L. Willis, B. Willke, M. H. Wimmer, L. Winkelmann, W. Winkler, C. C. Wipf, A. G. Wiseman, H. Wittel, G. Woan, J. Worden, J. L. Wright, G. Wu, J. Yablon, I. Yakushin, W. Yam, H. Yamamoto, C. C. Yancey, M. J. Yap, H. Yu, M. Yvert, A. Zadrofmmode \textbackslashdotz\textbackslashelse \textbackslash.z\textbackslashfiny, L. Zangrando, M. Zanolin, J.-P. Zendri, M. Zevin, F. Zhang, L. Zhang, M. Zhang, Y. Zhang, C. Zhao, M. Zhou, Z. Zhou, X. J. Zhu, M. E. Zucker, S. E. Zuraw, and J. Zweizig. Observation of Gravitational Waves from a Binary Black Hole Merger. *Phys. Rev. Lett.*, 116(6): 061102, February 2016. doi: 10.1103/PhysRevLett.116.061102. URL `http://link.aps.org/doi/10.1103/PhysRevLett.116.061102`.

[45] The LIGO Scientific Collaboration, the Virgo Collaboration, B. P. Abbott, R. Abbott, T. D. Abbott, S. Abraham, F. Acernese, K. Ackley, C. Adams, and R. X. Adhikari. Tests of General Relativity with the Binary Black Hole Signals from the LIGO-Virgo Catalog GWTC-1. *arXiv e-prints*, page arXiv:1903.04467, March 2019.

[46] Yu. N. Pokotilovski. Constraints on new interactions from neutron scattering experiments. *Physics of Atomic Nuclei*, 69(6):924–931, 2006. ISSN 1562-692X. doi: 10.1134/S1063778806060020. URL `http://dx.doi.org/10.1134/S1063778806060020`.

[47] Y. Kamiya, K. Itagaki, M. Tani, G. N. Kim, and S. Komamiya. Constraints on New Gravitylike Forces in the Nanometer Range. *Phys. Rev. Lett.*, 114(16):161101, April 2015. doi: 10.1103/PhysRevLett.

114.161101. URL `https://link.aps.org/doi/10.1103/PhysRevLett.114.161101`.

[48] V. V. Nesvizhevsky, G. Pignol, and K. V. Protasov. Neutron scattering and extra-short-range interactions. *Phys. Rev. D*, 77(3):034020, February 2008. doi: 10.1103/PhysRevD.77.034020. URL `https://link.aps.org/doi/10.1103/PhysRevD.77.034020`.

[49] Thomas Ederth. Template-stripped gold surfaces with 0.4-nm rms roughness suitable for force measurements: Application to the Casimir force in the 20\textbackslashchar21100-nm range. *Phys. Rev. A*, 62 (6):062104, November 2000. doi: 10.1103/PhysRevA.62.062104. URL `http://link.aps.org/doi/10.1103/PhysRevA.62.062104`.

[50] Anushree Roy, Chiung-Yuan Lin, and U. Mohideen. Improved precision measurement of the Casimir force. *Phys. Rev. D*, 60(11):111101, November 1999. doi: 10.1103/PhysRevD.60.111101. URL `http://link.aps.org/doi/10.1103/PhysRevD.60.111101`.

[51] Y.-J. Chen, W. K. Tham, D. E. Krause, D. López, E. Fischbach, and R. S. Decca. Stronger Limits on Hypothetical Yukawa Interactions in the 30\textbackslashchar218000 nm Range. *Phys. Rev. Lett.*, 116(22): 221102, June 2016. doi: 10.1103/PhysRevLett.116.221102. URL `http://link.aps.org/doi/10.1103/PhysRevLett.116.221102`.

[52] J. G. Lee, E. G. Adelberger, T. S. Cook, S. M. Fleischer, and B. R. Heckel. New Test of the Gravitational $1/r^2$ Law at Separations down to $52\text \text \ensuremath\mu\mathrmm$. *Phys. Rev. Lett.*, 124 (10):101101, March 2020. doi: 10.1103/PhysRevLett.124.101101. URL `https://link.aps.org/doi/10.1103/PhysRevLett.124.101101`.

[53] Tobias Jenke, Joachim Bosina, Gunther Cronenberg, Hanno Filter, Peter Geltenbort, Andrei N. Ivanov, Jakob Micko, Mario Pitschmann, Tobias Rechberger, René I. P. Sedmik, Martin Thalhammer, and Hartmut Abele. Testing gravity at short distances: Gravity Resonance Spectroscopy with qBOUNCE. In *European Physical Journal Web of Conferences*, volume 219 of *European Physical Journal Web of Conferences*, page 05003, May 2019. doi: 10.1051/epjconf/201921905003.

[54] Jonas Schmöle, Mathias Dragosits, Hans Hepach, and Markus Aspelmeyer. A micromechanical proof-of-principle experiment for measuring the gravitational force of milligram masses. *Classical and Quantum Gravity*, 33(12):125031, May 2016. doi: 10.1088/0264-9381/33/12/125031. URL `https://doi.org/10.1088%2F0264-9381%2F33%2F12%2F125031`.

[55] Alessio Belenchia, Robert M. Wald, Flaminia Giacomini, Esteban Castro-Ruiz, fmmode \checkC\else \fiaslav Brukner, and Markus Aspelmeyer. Quantum superposition of massive objects and the quantization of gravity. *Phys. Rev. D*, 98(12):126009, December 2018. doi: 10.1103/PhysRevD.98.126009. URL `https://link.aps.org/doi/10.1103/PhysRevD.98.126009`.

[56] Tanaka, Saki, Nakaya, Yusuke, Narikawa, Reiya, Ninomiya, Kazufumi, Onishi, Junichi, Pearson, Matthew, Openshaw, Robert, Saiba, Shuntaro,

Tanuma, Ryosuke, Totsuka, Yumi, and Murata, Jiro. Search of non-standard strong gravity at nuclear scale using electron spin geodetic precession. *EPJ Web of Conferences*, 66:05021, 2014. doi: 10.1051/epjconf/20146605021. URL `http://dx.doi.org/10.1051/epjconf/20146605021`.

[57] M. Hori, A. Dax, J. Eades, K. Gomikawa, R. S. Hayano, N. Ono, W. Pirkl, E. Widmann, H. A. Torii, B. Juhász, D. Barna, and D. Horváth. Determination of the Antiproton-to-Electron Mass Ratio by Precision Laser Spectroscopy of $øverlinep\textbackslashmathrmHe+$. *Phys. Rev. Lett.*, 96(24):243401, June 2006. doi: 10.1103/PhysRevLett.96.243401. URL `https://link.aps.org/doi/10.1103/PhysRevLett.96.243401`.

[58] M. J. Sparnaay. Measurements of attractive forces between flat plates. *Physica*, 24(6):751 – 764, 1958. ISSN 0031-8914. doi: http://dx.doi.org/10.1016/S0031-8914(58)80090-7. URL `http://www.sciencedirect.com/science/article/pii/S0031891458800907`.

[59] Steve K. Lamoreaux. Demonstration of the Casimir Force in the 0.6 to 6 m Range. *Physical Review Letters*, 78(1):5–8, 1997.

[60] D. J. Kapner, T. S. Cook, E. G. Adelberger, J. H. Gundlach, B. R. Heckel, C. D. Hoyle, and H. E. Swanson. Tests of the Gravitational Inverse-Square Law below the Dark-Energy Length Scale. *Physical Review Letters*, 98(021101), 2007.

[61] John G Lee. Testing Gravity Below 50 micrometers, March 2019. URL `http://meetings.aps.org/Meeting/APR19/Session/D16.4`.

[62] Reza Matloob and Hossain Falinejad. Casimir force between two dielectric slabs. *Phys. Rev. A*, 64(4):042102, September 2001. doi: 10.1103/PhysRevA.64.042102. URL `https://link.aps.org/doi/10.1103/PhysRevA.64.042102`.

[63] Andrew A. Geraci, Sylvia J. Smullin, David M. Weld, John Chiaverini, and Aharon Kapitulink. Improved constraints on non-Newtonian forces at 10 microns. *Physical Review D*, 78(022002), 2008.

[64] Hideki Yukawa. On the Interaction of Elementary Particles. I. *Proceedings of the Physico-Mathematical Society of Japan. 3rd Series*, 17:48–57, 1935.

[65] M. Bordag, B. Geyer, G. L. Klimchitskaya, and V. M. Mostepanenko. New constraints for non-Newtonian gravity in the nanometer range from the improved precision measurement of the Casimir force. *Phys. Rev. D*, 62(1):011701, June 2000. doi: 10.1103/PhysRevD.62.011701. URL `http://link.aps.org/doi/10.1103/PhysRevD.62.011701`.

[66] Jiro Murata and Saki Tanaka. A review of short-range gravity experiments in the LHC era. *Classical and Quantum Gravity*, 32(3):033001, 2015. URL `http://stacks.iop.org/0264-9381/32/i=3/a=033001`.

[67] E. G. Adelberger, B. R. Heckel, S. Hoedl, C. D. Hoyle, D. J. Kapner, and A. Upadhye. Particle-Physics Implications of a Recent Test of the Gravitational Inverse-Square Law. *Phys. Rev. Lett.*, 98(13):

131104, March 2007. doi: 10.1103/PhysRevLett.98.131104. URL `https://link.aps.org/doi/10.1103/PhysRevLett.98.131104`.

[68] A. Conroy and J. Edholm. Newtonian Potential and Geodesic Completeness in Infinite Derivative Gravity. *ArXiv e-prints*, May 2017.

[69] Valeri P. Frolov and Andrei Zelnikov. Head-on collision of ultrarelativistic particles in ghost-free theories of gravity. *Phys. Rev. D*, 93 (6):064048, March 2016. doi: 10.1103/PhysRevD.93.064048. URL `https://link.aps.org/doi/10.1103/PhysRevD.93.064048`.

[70] Spyridon Talaganis, Tirthabir Biswas, and Anupam Mazumdar. Towards understanding the ultraviolet behavior of quantum loops in infinite-derivative theories of gravity. *Classical and Quantum Gravity*, 32(21): 215017, 2015. URL `http://stacks.iop.org/0264-9381/32/i=21/a=215017`.

[71] Yves Dirian, Stefano Foffa, Martin Kunz, Michele Maggiore, and Valeria Pettorino. Non-local gravity and comparison with observational datasets. II. Updated results and Bayesian model comparison with CDM. *Journal of Cosmology and Astroparticle Physics*, 2016(05):068, 2016. URL `http://stacks.iop.org/1475-7516/2016/i=05/a=068`.

[72] James Edholm, Alexey S. Koshelev, and Anupam Mazumdar. Behavior of the Newtonian potential for ghost-free gravity and singularity free gravity. *Phys. Rev. D*, 94(10):104033, November 2016. doi: 10.1103/PhysRevD.94.104033. URL `https://link.aps.org/doi/10.1103/PhysRevD.94.104033`.

[73] L. Perivolaropoulos. Submillimeter spatial oscillations of Newton's constant: Theoretical models and laboratory tests. *Phys. Rev. D*, 95(8): 084050, April 2017. doi: 10.1103/PhysRevD.95.084050. URL `https://link.aps.org/doi/10.1103/PhysRevD.95.084050`.

[74] H Razmi. A Simply Regularized Derivation of the Casimir Force. *Electronic Journal of Theoretical Physics*, 3(13), 2006.

[75] E. Zeidler, H. R. Schwarz, and W. Hackbusch. *Teubner Taschenbuch der Mathematik*. B. G. Teubner Verlag, Wiesbaden, 2 edition, November 2003. ISBN 3-519-20012-0.

[76] J. Bocki, J. Randrup, W. J. wiaecki, and C. F. Tsang. Proximity forces. *Annals of Physics*, 105:427–462, June 1977. doi: 10.1016/0003-4916(77) 90249-4.

[77] D. ter Haar J. B. Sykes and L. P. Pitaevskii (Auth.). *Perspectives in Theoretical Physics. The Collected Papers of E. M. Lifshitz*. Pergamon Press, 1992. ISBN 978-0-08-036364-6 0-08-036364-4. URL `http://gen.lib.rus.ec/book/index.php?md5=9581617A496DD17CEC2C7565BA81CEB5`.

[78] P. Drude. Zur Elektronentheorie der Metalle; II. Teil. Galvanomagnetische und thermomagnetische Effecte. *Annalen der Physik*, 308:369–402, 1900. doi: 10.1002/andp.19003081102.

[79] P. Drude. Zur Elektronentheorie der Metalle. *Annalen der Physik*, 306 (3):566–613, 1900. ISSN 1521-3889. doi: 10.1002/andp.19003060312. URL `http://dx.doi.org/10.1002/andp.19003060312`.

[80] J. J. Thomson M. A. XL. Cathode Rays. *The London, Edinburgh, and Dublin Philosophical Magazine and Journal of Science*, 44(269):293–316, 1897. doi: 10.1080/14786449708621070. URL `https://doi.org/10.1080/14786449708621070`.

[81] H.-J. Hagemann, W. Gudat, and C. Kunz. Optical constants from the far infrared to the x-ray region: Mg, Al, Cu, Ag, Au, Bi, C, and Al2O3. *J. Opt. Soc. Am.*, 65(6):742–744, June 1975. doi: 10.1364/JOSA.65.000742. URL `http://www.osapublishing.org/abstract.cfm?URI=josa-65-6-742`.

[82] A. O. Sushkov, W. J. Kim, D. A. R. Dalvit, and S. K. Lamoreaux. Observation of the thermal Casimir force. *Nat Phys*, 7(3):230–233, March 2011. ISSN 1745-2473. doi: 10.1038/nphys1909. URL `http://dx.doi.org/10.1038/nphys1909`.

[83] V. B. Bezerra, G. L. Klimchitskaya, V. M. Mostepanenko, and C. Romero. Violation of the Nernst heat theorem in the theory of the thermal Casimir force between Drude metals. *Phys. Rev. A*, 69 (2):022119, February 2004. doi: 10.1103/PhysRevA.69.022119. URL `https://link.aps.org/doi/10.1103/PhysRevA.69.022119`.

[84] I. Brevik, J. B. Aarseth, J. S. Høye, and K. A. Milton. Temperature dependence of the Casimir effect. *Phys. Rev. E*, 71(5):056101, May 2005. doi: 10.1103/PhysRevE.71.056101. URL `https://link.aps.org/doi/10.1103/PhysRevE.71.056101`.

[85] C.-C. Chang, A. A. Banishev, R. Castillo-Garza, G. L. Klimchitskaya, V. M. Mostepanenko, and U. Mohideen. Gradient of the Casimir force between Au surfaces of a sphere and a plate measured using an atomic force microscope in a frequency-shift technique. *Phys. Rev. B*, 85(16): 165443, April 2012. doi: 10.1103/PhysRevB.85.165443. URL `http://link.aps.org/doi/10.1103/PhysRevB.85.165443`.

[86] H. C. Hamaker. The London-van der Waals attraction between spherical particles. *Physica*, 4:1058–1072, October 1937. doi: 10.1016/S0031-8914(37)80203-7.

[87] Jan Czarnecki. Van der Waals attraction energy between sphere and half-space. *Journal of Colloid and Interface Science*, 72(2):361–362, 1979.

[88] E. J. Clayfield, E. C. Lumb, and P. H. Mackey. Retarded dispersion forces in colloidal particlesExact integration of the casimir and polder equation. *Journal of Colloid and Interface Science*, 37(2):382 – 389, 1971. ISSN 0021-9797. doi: http://dx.doi.org/10.1016/0021-9797(71)90306-7. URL `http://www.sciencedirect.com/science/article/pii/0021979771903067`.

[89] John Gregory. Approximate expressions for retarded van der waals interaction. *Journal of Colloid and Interface Science*, 83(1):138 – 145, 1981. ISSN 0021-9797. doi: http://dx.doi.org/10.1016/0021-9797(81)90018-7. URL `http://www.sciencedirect.com/science/article/pii/0021979781900187`.

[90] G. L. Klimchitskaya, U. Mohideen, and V. M. Mostepanenko. Casimir and van der Waals forces between two plates or a sphere (lens) above a plate made of real metals. *Phys. Rev. A*, 61(6):062107, May 2000. doi: 10.1103/PhysRevA.61.062107. URL `http://link.aps.org/doi/10.1103/PhysRevA.61.062107`.

[91] W. Demtröder. *Experimentalphysik 3: Atome, Moleküle und Festkörper.* Experimentalphysik / Wolfgang Demtröder. Springer, 2005. ISBN 978-3-540-21473-1. URL `https://books.google.de/books?id=UmrfixbVs_AC`.

[92] L. Boyer, F. Houze, A. Tonck, J.-L. Loubet, and J.-M. Georges. The influence of surface roughness on the capacitance between a sphere and a plane. *Journal of Physics D: Applied Physics*, 27(7):1504, 1994. URL `http://stacks.iop.org/0022-3727/27/i=7/a=024`.

[93] Alexander O. Sushkov, Woo-Jong A. Kim, Diego A.R. Dalvit, and Steve K. Lamoreaux. New Experimental Limits on Non-Newtonian Forces in the Micrometer Range. *Physical Review Letters*, 2011. doi: 10.1103/PhysRevLett.107.171101.

[94] W. J. Kim, A. O. Sushkov, D. A. R. Dalvit, and S. K. Lamoreaux. Surface contact potential patches and Casimir force measurements. *Phys. Rev. A*, 81(2):022505, February 2010. doi: 10.1103/PhysRevA.81.022505. URL `http://link.aps.org/doi/10.1103/PhysRevA.81.022505`.

[95] Martin Knudsen. Ein absolutes Manometer. *Annalen der Physik*, 337(9):809–842, 1910. ISSN 1521-3889. doi: 10.1002/andp.19103370906. URL `http://dx.doi.org/10.1002/andp.19103370906`.

[96] D. A. Grigg, P. E. Russell, and J. E. Griffith. Tipsample forces in scanning probe microscopy in air and vacuum. *Journal of Vacuum Science & Technology A: Vacuum, Surfaces, and Films*, 10(4):680–683, 1992. doi: 10.1116/1.577709. URL `https://doi.org/10.1116/1.577709`.

[97] G. Mason and W. C. Clark. Liquid bridges between spheres. *Chemical Engineering Science*, 20(10):859 – 866, 1965. ISSN 0009-2509. doi: https://doi.org/10.1016/0009-2509(65)80082-3. URL `http://www.sciencedirect.com/science/article/pii/0009250965800823`.

[98] Christopher D. Willett, Michael J. Adams, Simon A. Johnson, and Jonathan P. K. Seville. Capillary Bridges between Two Spherical Bodies. *Langmuir*, 16(24):9396–9405, 2000. doi: 10.1021/la000657y. URL `https://doi.org/10.1021/la000657y`.

[99] H. J. McSkimin. Measurement of Elastic Constants at Low Temperatures by Means of Ultrasonic WavesData for Silicon and Germanium Single Crystals, and for Fused Silica. *Journal of Applied Physics*, 24(8):988–997, 1953. doi: 10.1063/1.1721449. URL `https://doi.org/10.1063/1.1721449`.

[100] W. Demtröder. *Experimentalphysik 2: Elektrizität und Optik.* Experimentalphysik / Wolfgang Demtröder. Springer, 2006. ISBN 978-3-540-33794-6.

[101] Luis L. Sánchez-Soto, Juan J. Monzón, and Gerd Leuchs. The many facets of the FabryPerot. *European Journal of Physics*, 37(6):064001, 2016. URL `http://stacks.iop.org/0143-0807/37/i=6/a=064001`.

[102] R. Regener and W. Sohler. Loss in low-finesse Ti:LiNbO3 optical waveguide resonators. *Applied Physics B*, 36(3):143–147, March 1985. ISSN 1432-0649. doi: 10.1007/BF00691779. URL `https://doi.org/10.1007/BF00691779`.

[103] U. Dürig. Relations between interaction force and frequency shift in large-amplitude dynamic force microscopy. *Applied Physics Letters*, 75 (3):433–435, 1999. doi: 10.1063/1.124399. URL `https://doi.org/10.1063/1.124399`.

[104] Franz J. Giessibl. Forces and frequency shifts in atomic-resolution dynamic-force microscopy. *Phys. Rev. B*, 56(24):16010–16015, December 1997. doi: 10.1103/PhysRevB.56.16010. URL `http://link.aps.org/doi/10.1103/PhysRevB.56.16010`.

[105] John E. Sader and Suzanne P. Jarvis. Accurate formulas for interaction force and energy in frequency modulation force spectroscopy. *Applied Physics Letters*, 84(10):1801–1803, 2004. doi: http://dx.doi.org/10.1063/1.1667267. URL `http://scitation.aip.org/content/aip/journal/apl/84/10/10.1063/1.1667267`.

[106] W. Demtröder. *Experimentalphysik 1: Mechanik und Wärme*. Experimentalphysik / Wolfgang Demtröder. Springer, 4 edition, 2005. ISBN 978-3-540-26034-X. URL `https://books.google.de/books?id=UmrfixbVs_AC`.

[107] William McC Siebert. *Circuits, signals, and systems*, volume 2. MIT press, 1986.

[108] Stephen Kulla. Nested Intervals, October 2009. URL `https://commons.wikimedia.org/wiki/File:Illustration_nested_intervals.svg`.

[109] Robert Piessens, Elise de Doncker-Kapenga, Christoph W Überhuber, and David K Kahaner. *QUADPACK: a subroutine package for automatic integration*, volume 1. Springer Science & Business Media, 2012.

[110] Robert Piessens, David K Kahaner, Christoph W Überhuber, De Doncker-Kapenga, and others. Quadpack. 1983.

[111] Donald W. Marquardt. An Algorithm for Least-Squares Estimation of Nonlinear Parameters. *Journal of the Society for Industrial and Applied Mathematics*, 11(2):431–441, 1963. doi: 10.1137/0111030. URL `https://doi.org/10.1137/0111030`.

[112] Ananth Ranganathan. The Levenberg-Marquardt Algorithm, June 2004. URL `http://ananth.in/docs/lmtut.pdf`.

[113] Kaj Madsen, Hans Bruun Nielsen, and Ole Tingleff. Methods for nonlinear least squares problems. 1999. URL `http://www2.imm.dtu.dk/pubdb/views/edoc_download.php/3215/pdf/imm3215.pdf`.

[114] Rainer Storn and Kenneth Price. Differential evolutiona simple and efficient heuristic for global optimization over continuous spaces. *Journal of global optimization*, 11(4):341–359, 1997.

[115] David Ardia, Kris Boudt, Peter Carl, Katharine M. Mullen, and Brian G. Peterson. Differential Evolution with DEoptim. *The R Journal*, 3(1): 27–34, 2011. URL `https://journal.r-project.org/archive/2011/RJ-2011-005/index.html`.

[116] Ifan Hughes and Thomas Hase. *Measurements and their uncertainties: a practical guide to modern error analysis.* Oxford University Press, 2010.

[117] William H Press. *Numerical recipes in Fortran 77 and Fortran 90: the art of scientific and parallel computing; diskette v 2.06 h.* Cambridge University Press, 1996.

[118] Bradley Efron and Robert Tibshirani. Bootstrap methods for standard errors, confidence intervals, and other measures of statistical accuracy. *Statistical science*, pages 54–75, 1986.

[119] Andrew Yacoot and Ludger Koenders. Aspects of scanning force microscope probes and their effects on dimensional measurement. *Journal of Physics D*, 41(10):103001, 2008.

[120] Ichiro Shiraki, Yutaka Miyatake, Toshihiko Nagamura, and Kazushi Miki. Demonstration of low-temperature atomic force microscope with atomic resolution using piezoresistive cantilevers. *Review of Scientific Instruments*, 77(2):023705, 2006. doi: 10.1063/1.2169469. URL `https://doi.org/10.1063/1.2169469`.

[121] JA DeRose and J-P Revel. Examination of atomic (scanning) force microscopy probe tips with the transmission electron microscope. *Microscopy and Microanalysis*, 3(3):203–213, 1997.

[122] A. Ruf, M. Abraham, J. Diebel, W. Ehrfeld, P. Güthner, M. Lacher, K. Mayr, and J. Reinhardt. Integrated FabryPérot distance control for atomic force microscopy. *Journal of Vacuum Science & Technology B: Microelectronics and Nanometer Structures Processing, Measurement, and Phenomena*, 15(3):579–585, 1997. doi: 10.1116/1.589295. URL `https://avs.scitation.org/doi/abs/10.1116/1.589295`.

[123] Estill I Green. The story of Q. *American Scientist*, 43(4):584–594, 1955.

[124] R. Sandberg, K. Mølhave, A. Boisen, and W. Svendsen. Effect of gold coating on the Q -factor of a resonant cantilever. *Journal of Micromechanics and Microengineering*, 15(12):2249, 2005. URL `http://stacks.iop.org/0960-1317/15/i=12/a=006`.

[125] A.H. Slocum. *Precision Machine Design.* Society of Manufacturing Engineers, 1992. ISBN 978-0-87263-492-3. URL `https://books.google.de/books?id=uG7aqgal65YC`.

[126] O. Gerberding, F. Guzmán Cervantes, J. Melcher, J. R. Pratt, and J. M. Taylor. Optomechanical reference accelerometer. *Metrologia*, 52(5):654, 2015. URL `http://stacks.iop.org/0026-1394/52/i=5/a=654`.

[127] Jens Trampe Broch. *Messungen von Mechanischen Schwingungen und Stössen.* Die Anwendung der B&K Messsysteme für. Brüel & Kjaer, September 1970.

[128] H. I. Smith. OpticalContact Bonding. *The Journal of the Acoustical Society of America*, 37(5):928–929, 1965. doi: 10.1121/1.1909490. URL `http://dx.doi.org/10.1121/1.1909490`.

[129] E. J. Elliffe, J. Bogenstahl, A. Deshpande, J. Hough, C. Killow, S. Reid, D. Robertson, S. Rowan, H. Ward, and G. Cagnoli. Hydroxide-catalysis bonding for stable optical systems for space. *Classical and Quantum Gravity*, 22(10):S257, 2005. URL `http://stacks.iop.org/0264-9381/22/i=10/a=018`.

[130] Eric R. I. Abraham and Eric A. Cornell. Teflon feedthrough for coupling optical fibers into ultrahigh vacuum systems. *Appl. Opt.*, 37(10):1762–1763, April 1998. doi: 10.1364/AO.37.001762. URL `http://ao.osa.org/abstract.cfm?URI=ao-37-10-1762`.

[131] Massimo Rossella, Marco Prata, and Tommaso Cervi. STATUS ON Optical fiber: Preliminary tests on Optical Fiber and Fiber Optic Feedthrough, January 2016. URL `https://www.vacom.de/download/de/sonstige/ICARUS_Optical_fiber%20Copy.pdf#page=13`.

[132] M. Bonesini. Laboratory tests for the PMTs laser based timing calibration system, January 2017. URL `https://www.vacom.de/download/de/sonstige/WA104-PMTs-calibration%20Copy.pdf#page=34`.

[133] Vacom. Optical Fiber Feedthroughs for vacuum applications with FC/APC or FC/PC connectors. URL `https://www.vacom.de/en/downloads/category/794-optical-fiber-feedthroughs?download=2928:optical-fiber-feedthroughs-fc-pc-and-fc-apc`.

[134] J. M. Breguet and R. Clavel. Stick and slip actuators: design, control, performances and applications. In *Micromechatronics and Human Science, 1998. MHS '98. Proceedings of the 1998 International Symposium on*, pages 89–95, November 1998. doi: 10.1109/MHS.1998.745756.

[135] W. Zinth and U. Zinth. *Optik: Lichtstrahlen - Wellen - Photonen.* Oldenbourg, 2005. ISBN 978-3-486-27580-3. URL `https://books.google.de/books?id=wIzcPAAACAAJ`.

[136] J. L. Santos, A. P. Leite, and D. A. Jackson. Optical fiber sensing with a low-finesse FabryPerot cavity. *Appl. Opt.*, 31(34):7361–7366, December 1992. doi: 10.1364/AO.31.007361. URL `http://ao.osa.org/abstract.cfm?URI=ao-31-34-7361`.

[137] Oliver Gerberding. *Phase readout for satellite interferometry.* PhD thesis, Leibniz Universität Hannover, 2014. URL `http://olivergerberding.com/wp-content/uploads/2014/04/PhDThesis_20140414.pdf`.

[138] Peter C Hughes. Spacecraft Attitude Dynamics John Wiley and Sons. *New York*, 1986.

[139] Thomas Gustafsson. On the design and implementation of a rotary crane controller. *European Journal of Control*, 2(2):166–175, 1996.

[140] Katsuhiko Ogata and others. *Discrete-time control systems*, volume 2. Prentice Hall Englewood Cliffs, NJ, 1995.

[141] V. G. Rao and D. S. Bernstein. Naive control of the double integrator. *IEEE Control Systems Magazine*, 21(5):86–97, 2001.

[142] M. Karimi-Ghartemani, H. Karimi, and M. R. Iravani. A magnitude/phase-locked loop system based on estimation of frequency and in-phase/quadrature-phase amplitudes. *IEEE Transactions on Industrial Electronics*, 51(2):511–517, April 2004. ISSN 0278-0046. doi: 10.1109/TIE.2004.825282.

[143] Christopher Bishop. *Pattern Recognition and Machine Learning*. Information Science and Statistics. 1 edition, 2006. ISBN 978-0-387-31073-2.

[144] V. Lehtinen and M. Renfors. Truncation noise analysis of noise shaping DSP systems with application to CIC decimators. In *2002 11th European Signal Processing Conference*, pages 1–4, September 2002.

[145] M. S. Senousy, R. K. N. D. Rajapakse, D. Mumford, and M. S. Gadala. Self-heat generation in piezoelectric stack actuators used in fuel injectors. *Smart Materials and Structures*, 18(4):045008, 2009. URL http://stacks.iop.org/0964-1726/18/i=4/a=045008.

[146] Paul R. Wilkinson, Gordon A. Shaw, and Jon R. Pratt. Determination of a cantilever's mechanical impedance using photon momentum. *Applied Physics Letters*, 102(18):–, 2013. doi: http://dx.doi.org/10.1063/1.4803664. URL http://scitation.aip.org/content/aip/journal/apl/102/18/10.1063/1.4803664.

[147] K.V. Price, R.N. Storn, and J.A. Lampinen. *Differential Evolution: A Practical Approach to Global Optimization*. Natural Computing Series. Springer, 2005.

[148] S. Bütefisch, S. Büttgenbach, T. Kleine-Besten, and U. Brand. Micromechanical three-axial tactile force sensor for micromaterial characterisation. *Microsystem Technologies*, 7(4):171–174, November 2001. ISSN 1432-1858. doi: 10.1007/s005420000083. URL https://doi.org/10.1007/s005420000083.

[149] L Doring, U Brand, and J Fruhauf. Micro force transfer standards. *VDI BERICHTE*, 1685:83–90, 2002.

[150] Helena Schmidt. *A method to test Newton's law of gravity at micro- and submicrometre distances with parallel plates*. Berlin, March 2014. URL www.dpg-verhandlungen.de/year/2014/conference/berlin/part/gr/session/5/contribution/3.

[151] Vladimir Nesterov, Michael Mueller, L. L. Frumin, and Uwe Brand. A new facility to realize a nanonewton force standard based on electrostatic methods. *Metrologia*, 49:277–282, 2009. doi: doi:10.1088/0026-1394/46/3/016.

[152] V. B. Bezerra, G. L. Klimchitskaya, U. Mohideen, V. M. Mostepanenko, and C. Romero. Impact of surface imperfections on the Casimir force for lenses of centimeter-size curvature radii. *Phys. Rev. B*, 83(7):075417,

February 2011. doi: 10.1103/PhysRevB.83.075417. URL `http://link.aps.org/doi/10.1103/PhysRevB.83.075417`.

[153] wdwd. *Piezokeramik*. 2010. URL `https://de.wikipedia.org/wiki/Datei:Piezokeramik.svg`.

[154] Warren P. Mason. Piezoelectricity, its history and applications. *The Journal of the Acoustical Society of America*, 70(6):1561–1566, 1981. doi: 10.1121/1.387221. URL `http://dx.doi.org/10.1121/1.387221`.

[155] J. Reiser and H. Marth. PIRest Technology - How to Keep the Last Position of PZT Actuators without Electrical Power. In *ACTUATOR 2018; 16th International Conference on New Actuators*, pages 1–4, June 2018.

[156] Felipe Guzmán Cervantes, Lee Kumanchik, Jon Pratt, and Jacob M. Taylor. High sensitivity optomechanical reference accelerometer over 10 kHz. *Applied Physics Letters*, 104(22), 2014. doi: http://dx.doi.org/10.1063/1.4881936. URL `http://scitation.aip.org/content/aip/journal/apl/104/22/10.1063/1.4881936`.